

## GAMMA-RAY BURSTS AND THE FIREBALL MODEL

Tsvi Piran

Racah Institute for Physics, The Hebrew University, Jerusalem, 91904, Israel<sup>1</sup>

and

Physics Department, Columbia University, New York, NY 10027, USA

*Draft version November 26, 2024*

## ABSTRACT

Gamma-ray bursts (GRBs) have puzzled astronomers since their accidental discovery in the late sixties. The BATSE detector on the COMPTON-GRO satellite has been detecting one burst per day for the last six years. Its findings have revolutionized our ideas about the nature of these objects. They have shown that GRBs are at cosmological distances. This idea was accepted with difficulties at first. The recent discovery of an X-ray afterglow by the Italian/Dutch satellite BeppoSAX has led to a detection of high red-shift absorption lines in the optical afterglow of GRB970508 and in several other bursts and to the identification of host galaxies to others. This has confirmed the cosmological origin. Cosmological GRBs release  $\sim 10^{51} - 10^{53}$  ergs in a few seconds making them the most (electromagnetically) luminous objects in the Universe. The simplest, most conventional, and practically inevitable, interpretation of these observations is that GRBs result from the conversion of the kinetic energy of ultra-relativistic particles or possibly the electromagnetic energy of a Poynting flux to radiation in an optically thin region. This generic “fireball” model has also been confirmed by the afterglow observations. The “inner engine” that accelerates the relativistic flow is hidden from direct observations. Consequently it is difficult to infer its structure directly from current observations. Recent studies show, however, that this “inner engine” is responsible for the complicated temporal structure observed in GRBs. This temporal structure and energy considerations indicates that the “inner engine” is associated with the formation of a compact object - most likely a black hole.

## 1. INTRODUCTION

Gamma-ray bursts (GRBs), short and intense bursts of  $\sim 100$  keV-1 MeV photons, were discovered accidentally in the late sixties by the Vela satellites[1]. The mission of these satellites was to monitor the “Outer Space Treaty” that forbade nuclear explosions in space. A wonderful by-product of this effort was the discovery of GRBs.

The discovery of GRBs was announced in 1973 [1]. It was confirmed quickly by Russian observations [2] and by observations on the IMP-6 satellite [3]. Since then, several dedicated satellites have been launched to observe the bursts and numerous theories were put forward to explain their origin. Claims of observations of cyclotron spectral lines and of discovery of optical archival counterparts led in the mid eighties to a consensus that GRBs originate from Galactic neutron stars. This model was accepted quite generally and was even discussed in graduate textbooks [4, 5, 6] and encyclopedia articles [7, 8].

The BATSE detector on the COMPTON-GRO (Gamma-Ray Observatory) was launched in the spring of 1991. It has revolutionized GRB observations and consequently our basic ideas on their nature. BATSE observations of the isotropy of GRB directions, combined with the deficiency of faint GRBs, ruled out the galactic disk neutron star model<sup>2</sup> and make a convincing case for their extra-galactic origin at cosmological distances [9]. This conclusion was recently confirmed by the discovery by BeppoSAX [10] of an X-ray transient counterparts to several GRBs. This was followed by a discovery of optical

[11, 12] and radio transients [13]. Absorption line with a redshift  $z = 0.835$  were measured in the optical spectrum of the counterpart to GRB970508 [14] providing the first redshift of the optical transient and the associated GRB. Latter, redshifted emission lines from galaxies associated with GRB971214 [15] (with  $z = 3.418$ ) and GRB980703 [16] (with  $z = 0.966$ ) were discovered. Galaxies has been discovered at the positions of other bursts. There is little doubt now that some, and most likely all GRBs are cosmological.

The cosmological origin of GRBs immediately implies that GRB sources are much more luminous than previously thought. They release  $\sim 10^{51} - 10^{53}$  ergs or more in a few seconds, the most (electromagnetically) luminous objects in the Universe. This also implies that GRBs are rare events. BATSE observes on average one burst per day. This corresponds, with the simplest model (assuming that the rate of GRBs does not change with cosmological time) to one burst per million years per galaxy. The average rate changes, of course, if we allow beaming or a cosmic evolution of the rate of GRBs.

In spite of those discoveries, the origin of GRBs is still mysterious. This makes GRBs a unique phenomenon in modern astronomy. While pulsars, quasars and X-ray sources were all explained within a few years, if not months, after their discovery, the origin of GRBs remains unknown after more than thirty years. The fact that GRBs are a short transient phenomenon which until recently did not have any known counterpart, is probably the main reason for this situation. Our inability to resolve this riddle

<sup>1</sup>permanent address<sup>2</sup>A few GRBs, now called soft gamma repeaters, compose a different phenomenon, are believed to form on galactic neutron stars.

also reflects the accidental and unexpected nature of this discovery which was not done by an astronomical mission. Theoretical astrophysics was not ripe to cope with GRBs when they were discovered.

A generic scheme of a cosmological GRB model has emerged in the last few years and most of this review is devoted to an exposition of this scheme. The recently observed X-ray, optical and radio counterparts were predicted by this picture [17, 18, 19, 20, 21]. This discovery can, to some extent, be considered as a confirmation of this model [22, 23, 24, 25]. According to this scheme the observed  $\gamma$ -rays are emitted when an ultra-relativistic energy flow is converted to radiation. Possible forms of the energy flow are kinetic energy of ultra-relativistic particles or electromagnetic Poynting flux. This energy is converted to radiation in an optically thin region, as the observed bursts are not thermal. It has been suggested that the energy conversion occurs either due to the interaction with an external medium, like the ISM [27] or due to internal process, such as internal shocks and collisions within the flow [28, 29, 30]. Recent work [20, 31] shows that the external shock scenario is quite unlikely, unless the energy flow is confined to an extremely narrow beam, or else the process is highly inefficient. The only alternative is that the burst is produced by internal shocks.

The “inner engine” that produces the relativistic energy flow is hidden from direct observations. However, the observed temporal structure reflects directly this “engine’s” activity. This model requires a compact internal “engine” that produces a wind – a long energy flow (long compared to the size of the “engine” itself) – rather than an explosive “engine” that produces a fireball whose size is comparable to the size of the “engine”. Not all the energy of the relativistic shell can be converted to radiation (or even to thermal energy) by internal shocks [32, 33, 34]. The remaining kinetic energy will most likely dissipate via external shocks that will produce an “afterglow” in different wavelength [20]. This afterglow was recently discovered, confirming the fireball picture.

At present there is no agreement on the nature of the “engine” - even though binary neutron star mergers [35] are a promising candidate. All that can be said with some certainty is that whatever drives a GRB must satisfy the following general features: It produces an extremely relativistic energy flow containing  $\approx 10^{51} - 10^{52}$  ergs. The flow is highly variable as most bursts have a variable temporal structure and it should last for the duration of the burst (typically a few dozen seconds). It may continue at a lower level on a time scale of a day or so [36]. Finally, it should be a rare event occurring about once per million years in a galaxy. The rate is of course higher and the energy is lower if there is a significant beaming of the gamma-ray emission. In any case the overall GRB emission in  $\gamma$ -rays is  $\sim 10^{52}$  ergs/10<sup>6</sup> years/galaxy.

We begin (section 2) with a brief review of GRB observation (see [37, 38, 39, 40, 41] for additional reviews and [42, 43, 44, 45] for a more extensive discussion). We then turn to an analysis of the observational constraints. We analyze the peak intensity distribution and show how the distance to GRBs can be estimated from this data. We also discuss the evidence for another cosmological ef-

fect: time-dilation (section 3). We then turn (section 4) to discuss the optical depth or the compactness problem. We argue that the only way to overcome this problem is if the sources are moving at an ultra-relativistic velocity towards us. An essential ingredient of this model is the notion of a fireball - an optically thick relativistic expanding electron-positron and photon plasma (for a different model see however [46]). We discuss fireball evolution in section 6. Kinematic considerations which determine the observed time scales from emission emerging from a relativistic flow provides important clues on the location of the energy conversion process. We discuss these constraints in section 7 and the energy conversion stage in section 8. We review the recent theories of afterglow formation 9. We examine the confrontation of these models with observations and we discuss some of the quantitative problems.

We then turn to the “inner engine” and review the recent suggestions for cosmological models (section 10). As this inner engine is hidden from direct observation, it is clear that there are only a few direct constraint that can be put on it. Among GRB models, binary neutron star merger [35] is unique. It is the only model that is based on an independently observed phenomenon [48], is capable of releasing the required amounts of energy [49] within a very short time scale and takes place at approximately the same rate [50, 51, 52]<sup>3</sup>. At present it is not clear if this merger can actually channel the required energy into a relativistic flow or if it could produce the very high energy observed in GRB971214. However, in view of the special status of this model we discuss its features and the possible observational confirmation of this model in section 10.2.

GRBs might have important implications to other branches of astronomy. Relation of GRBs to other astronomical phenomena such as UCHERs, neutrinos and gravitational radiation are discussed in section 11. The universe and our Galaxy are optically thin to low energy  $\gamma$ -rays. Thus, GRBs constitute a unique cosmological population that is observed practically uniformly on the sky (there are small known biases due to CGRO’s observation schedule). Most of these objects are located at  $z \approx 1$  or greater. Thus this population is farther than any other systematic sample (QSOs are at larger distances but they suffer from numerous selection effects and there is no all sky QSOs catalog). GRBs are, therefore, an ideal tool to explore the Universe. Already in 1986 Paczyński [53] proposed that GRBs might be gravitationally lensed. This has led to the suggestion to employ the statistics of lensed bursts to probe the nature of the lensing objects and the dark matter of the Universe [54]. The fact that no lensed bursts where detected so far is sufficient to rule out a critical density of  $10^{6.5} M_{\odot}$  to  $10^{8.1} M_{\odot}$  black holes [55]. Alternatively we may use the peak-flux distribution to estimate cosmological parameters such as  $\Omega$  and  $\Lambda$  [56]. The angular distribution of GRBs can be used to determine the very large scale structure of the Universe [57, 58]. The possible direct measurements of red-shift to some bursts enhances greatly the potential of these attempts. We conclude in section 12 by summarizing these suggestions.

Over the years several thousand papers concerning GRBs have appeared in the literature. With the grow-

<sup>3</sup>this is assuming that there is no strong cosmic evolution in the rate of GRB

ing interest in GRBs the number of GRB papers has been growing at an accelerated rate recently. It is, of course, impossible to summarize or even list all this papers here. I refer the interested reader to the complete GRB bibliography that was prepared by K. Hurley [59].

## 2. OBSERVATIONS

GRBs are short, non-thermal bursts of low energy  $\gamma$ -rays. It is quite difficult to summarize their basic features. This difficulty stems from the enormous variety displayed by the bursts. I will review here some features that I believe hold the key to this enigma. I refer the reader to the proceedings of the Huntsville GRB meetings [42, 43, 44, 45] and to other recent reviews for a more detailed discussion [37, 38, 39, 40, 41].

### 2.1. Duration:

A “typical” GRB (if there is such a thing) lasts about 10sec. However, observed durations vary by six orders of magnitude, from several milliseconds [60] to several thousand seconds [61]. About 3% of the bursts are preceded by a precursor with a lower peak intensity than the main burst [62]. Other bursts were followed by low energy X-ray tails [63]. Several bursts observed by the GINGA detector showed significant apparently thermal, X-ray emission before and after the main part of the higher energy emission [64, 65]. These are probably pre-discovery detections of the X-ray afterglow observed now by BeppoSAX and other X-ray detectors.

The definition of duration is, of course, not unique. BATSE’s team characterizes it using  $T_{90}$  ( $T_{50}$ ) the time needed to accumulate from 5% to 95% (from 25% to 75%) of the counts in the 50keV - 300keV band. The shortest BATSE burst had a duration of 5ms with structure on scale of 0.2ms [66]. The longest so far, GRB940217, displayed GeV activity one and a half hours the main burst [67]. The bursts GRB961027a, GRB961027b, GRB961029a and GRB961029b occurred from the same region in the sky within two days [68] if this “gang of four” is considered as a single very long burst then the longest duration so far is two days! These observations may indicate that some sources display a continued activity (at a variable level) over a period of days [69]. It is also possible that the observed afterglow is an indication of a continued activity [36].

The distribution of burst durations is bimodal. BATSE confirmed earlier hints [70] that the burst duration distribution can be divided into two sub-groups according to  $T_{90}$ : long bursts with  $T_{90} > 2\text{sec}$  and short bursts with  $T_{90} < 2\text{sec}$  [71, 72, 73, 74, 75, 76]. The ratio of observed long bursts to observed short bursts is three to one. This does not necessarily mean that there are fewer short bursts. BATSE’s triggering mechanism makes it less sensitive to short bursts than to long ones. Consequently short bursts are detected to smaller distances [74, 77, 78, 79] and we observed a smaller number of short bursts.

### 2.2. Temporal Structure and Variability

The bursts have a complicated and irregular time profiles which vary drastically from one burst to another. Sev-

eral time profiles, selected from the second BATSE catalog, are shown in Fig. 1. In most bursts, the typical variation takes place on a time-scale  $\delta T$  significantly smaller than the total duration of the burst,  $T$ . In a minority of the bursts there is only one peak with no substructure and in this case  $\delta T \sim T$ . It turns out that the observed variability provides an interesting clue to the nature of GRBs. We discuss this in section 7. We define the ratio  $\mathcal{N} \equiv T/\delta T$  which is a measure of the variability. Fig. 2 depicts the total observed counts (at  $E > 25\text{keV}$ ) from GRB1676. The bursts lasted  $T \sim 100\text{ sec}$  and it had peaks of width  $\delta T \sim 1\text{ sec}$ , leading to  $\mathcal{N} = 100$ .

### 2.3. Spectrum:

GRBs are characterized by emission in the few hundred keV ranges with a non-thermal spectrum (see Fig. 3) X-ray emission is weaker – only a few percent of the energy is emitted below 10keV and prompt emission at lower energies has not been observed so far. The current best upper limits on such emission are given by LOTIS. For GRB970223 LOTIS finds  $m_V > 11$  and provides an upper limit on the simultaneous optical to gamma-ray fluence ratio of  $< 1.1 \times 10^{-4}$  [80]. Most bursts are accompanied, on the other hand, by a high energy tail which contains a significant amount of energy –  $E^2 N(E)$  is almost a constant. GRB940217, for example, had a high energy tail up to 18 GeV[81]. In fact EGRET and COMPTEL (which are sensitive to higher energy emission but have a higher threshold and a smaller field of view) observations are consistent with the possibility that all bursts have high energy tails [82, 83].

An excellent phenomenological fit for the spectrum was introduced by Band *et al.* [84]:

$$N(\nu) = N_0 \begin{cases} (\hbar\nu)^\alpha \exp(-\frac{\hbar\nu}{E_0}) & \text{for } \hbar\nu < H ; \\ [(\alpha - \beta)E_0]^{(\alpha - \beta)} (\hbar\nu)^\beta \\ \times \exp(\beta - \alpha), & \text{for } \hbar\nu > H, \end{cases} \quad (1)$$

where  $H \equiv (\alpha - \beta)E_0$ . There is no particular theoretical model that predicts this spectral shape. Still, this function provides an excellent fit to most of the observed spectra. It is characterized by two power laws joined smoothly at a break energy  $H$ . For most observed values of  $\alpha$  and  $\beta$ ,  $\nu F_\nu \propto \nu^2 N(\nu)$  peaks at  $E_p = (\alpha + 2)E_0 = [(\alpha + 2)/(\alpha - \beta)]H$ . The “typical” energy of the observed radiation is  $E_p$ . That is this is where the source emits the bulk of its luminosity.  $E_p$  defined in this way should not be confused with the hardness ratio which is commonly used in analyzing BATSE’s data, namely the ratio of photons observed in channel 3 (100-300keV) to those observed in channel 2 (50-100keV). Sometimes we will use a simple power law fit to the spectrum:

$$N(E)dE \propto E^{-\alpha}dE. \quad (2)$$

In these cases the power law index will be denoted by  $\alpha$ . A typical spectra index is  $\alpha \approx 1.8 - 2$  [85].

In several cases the spectrum was observed simultaneously by several instruments. Burst 9206022, for example, was observed simultaneously by BATSE, COMPTEL and Ulysses. The time integrated spectrum on those detectors, which ranges from 25keV to 10MeV agrees well with a

Band spectrum with:  $E_p = 457 \pm 30\text{keV}$ ,  $\alpha = -0.86 \pm 0.15$  and  $\beta = -2.5 \pm 0.07$  [86]. Schaefer *et al.* [87] present a complete spectrum from 2keV to 500MeV for three bright bursts.

Fig. 4 shows the distribution of observed values of  $H$  in several samples [84, 88, 89]. Most of the bursts are in the range  $100\text{keV} < H < 400\text{keV}$ , with a clear maximum in the distribution around  $H \sim 200\text{keV}$ . There are not many soft GRBs - that is, GRBs with peak energy in the tens of keV range. This low peak energy cutoff is real as soft bursts would have been easily detected by current detectors. However it is not known whether there is a real paucity in hard GRBs and there is an upper cutoff to the GRB hardness or it just happens that the detection is easiest in this (few hundred keV) band. BATSE triggers, for example, are based mostly on the count rate between 50keV and 300keV. BATSE is, therefore, less sensitive to harder bursts that emit most of their energy in the MeV range. Using BATSE's observation alone one cannot rule out the possibility that there is a population of harder GRBs that emit equal power in total energy which are not observed because of this selection effect [90, 89, 91, 92]. More generally, a harder burst with the same energy as a soft one emits fewer photons. Furthermore, the spectrum is generally flat in the high energy range and it decays quickly at low energies. Therefore it is intrinsically more difficult to detect a harder burst. A study of the SMM data [93] suggests that there is a deficiency (by at least a factor of 5) of GRBs with hardness above 3MeV, relative to GRBs peaking at  $\sim 0.5\text{MeV}$ , but this data is consistent with a population of hardness that extends up to 2MeV.

Overall the spectrum is non-thermal. This indicates that the source must be optically thin. The spectrum deviates from a black body in both the low and the high energy ends: The X-ray paucity constraint rules out optically thick models in which the  $\gamma$ -rays could be effectively degraded to X-rays [94]. The high energy tails lead to another strong constraint on physical GRB models. These high energy photons escape freely from the source without producing electron positron pairs! As we show later, this provides the first and most important clue on the nature of GRBs.

The low energy part of the spectrum behaves in many cases like a power law:  $F_\nu \propto \nu^\alpha$  with  $-\frac{1}{2} < \alpha < \frac{1}{3}$ , [19, 95]. This is consistent with the low energy tail of synchrotron emission from relativistic electrons - a distribution of electrons in which *all* the population, not just the upper tail, is relativistic. This is a direct indication for the existence of relativistic shocks in GRBs. More than 90% of the bright bursts studied by Schaefer *et al.* [87] satisfy this limit. However, there may be bursts whose low energy tail is steeper [96]. Such a spectrum cannot be produced by a simple synchrotron emission model and it is not clear how it is produced.

#### 2.4. Spectral Evolution

Observations by earlier detectors as well as by BATSE have shown that the spectrum varies during the bursts. Different trends were found. Golenetskii *et al.* [97] examined two channel data from five bursts observed by the KONUS experiment on *Venera* 13 and 14 and found a correlation between the effective temperature and the lu-

minosity, implying that the spectral hardness is related to the luminosity. Similar results were obtained Mitrofanov et. al. [98]. Norris *et al.* [99] investigated ten bursts seen by instruments on the SMM (*Solar Maximum Mission*) satellite. They found that individual intensity pulses evolve from hard-to-soft with the hardness peaking earlier than the intensity. This was supported by more recent BATSE data [100]. Ford *et al.* [101] analyzed 37 bright BATSE bursts and found that the spectral evolution is a mixture of those found by Golenetskii *et al.* [97] and by Norris *et al.* [99]: The peak energy either rises with or slightly proceeds major intensity increases and softens for the remainder of the pulse. For bursts with multiple peak emission, later spikes tend to be softer than earlier ones.

A related but not similar trend is shown by the observations that the bursts are narrower at higher energies with  $T(\nu) \propto \nu^{-0.4}$  [102]. As we show in section 8.7.3 this behavior is consistent with synchrotron emission [103].

#### 2.5. Spectral Lines

Both absorption and emission features have been reported by various experiments prior to BATSE. Absorption lines in the 20-40keV range have been observed by several experiments - but never simultaneously. GINGA has discovered several cases of lines with harmonic structure [104, 105]. These lines were interpreted as cyclotron lines (reflecting a magnetic field of  $\approx 10^{12}\text{Gauss}$ ) and providing one of the strongest arguments in favor of the galactic neutron star model. Emission features near 400keV have been claimed in other bursts [106]. These have been interpreted as red-shifted 511keV annihilation lines with a corresponding red-shift of  $\approx 20\%$  due to the gravitational field on the surface of the Neutron star. These provided additional evidence for the galactic neutron star model.

So far BATSE has not found any of the spectral features (absorption or emission lines) reported by earlier satellites [107, 108]. This can be interpreted as a problem with previous observations (or with the difficult analysis of the observed spectra) or as an unlucky coincidence. Given the rate of observed lines in previous experiments it is possible (at the  $\approx 5\%$  level) that the two sets of data are consistent [109].

Recently Mészáros & Rees [110] suggested that within the relativistic fireball model the observed spectral lines could have been blue shifted iron X-ray line.

#### 2.6. Angular Positions

BATSE is capable of estimating on its own the direction to a burst. It is composed of eight detectors that are pointed towards different directions in the sky. The relative intensity of the counts in the various detectors allows us to measure the direction to the burst. The positional error of a given burst is the square root of the sum of squares of a systematic error and a statistical error. The statistical error depends on the strength of the burst. It is as large as  $20^\circ$  for a weak burst, and it is negligible for a strong one. The estimated systematic error (using a comparison of BATSE positions with IPN (Inter Planetary Network) localization) is  $\approx 1.6^\circ$  [111]. A different analysis of this comparison [112, 113] suggests that this might be slightly higher, around  $3^\circ$ .

The location of a burst is determined much better using the difference in arrival time of the burst to several detectors on different satellites. Detection by two satellites limits the position to a circle on the sky. Detection by three determines the position and detection by four or more over-determines it. Even in this case the positional error depends on the strength of the bursts. The stronger the burst, the easier it is to identify a unique moment of time in the incoming signals. Clearly, the accuracy of the positional determination is better the longer the distance between the satellites. The best positions that have been obtained in this way are with the IPN<sup>3</sup> of detectors. For 12 events the positional error boxes are of a few arc-minutes [114].

BeppoSAX Wide Field Camera (WFC) that covers about 5% of the sky located a few bursts within 3' ( $3\sigma$ ). BeppoSAX's Narrow Field Instrument (NFI) obtained the bursts' positions to within 50''. X-ray observations by ASCA and ROSAT have yielded error boxes of 30'' and 10'' respectively. Optical identification has led, as usual, to a localization within 1''. Finally VLBI radio observation of GRB970508 has yielded a position within 200 $\mu$ arcsec. The position of at least one burst is well known.

### 2.7. Angular Distribution

One of the most remarkable findings of BATSE was the observation that the angular distribution of GRBs' positions on the sky is perfectly isotropic. Early studies had shown an isotropic GRB distribution [115] which have even led to the suggestion that GRBs are cosmological [116]. In spite of this it was generally believed, prior to the launch of BATSE, that GRBs are associated with galactic disk neutron star. It has been expected that more sensitive detectors would discover an anisotropic distribution that would reflect the planar structure of the disk of the galaxy. BATSE's distribution is, within the statistical errors, in complete agreement with perfect isotropy. For the first 1005 BATSE bursts the observed dipole and quadrupole (corrected to BATSE sky exposure) relative to the galaxy are:  $\langle \cos\theta \rangle = 0.017 \pm 0.018$  and  $\langle \sin^2 b - 1/3 \rangle = -0.003 \pm 0.009$ . These values are, respectively,  $0.9\sigma$  and  $0.3\sigma$  from complete isotropy [39].

### 2.8. Quiescent Counterparts and the historical "No Host" Problem

One of the main obstacles in resolving the GRB mystery was the lack of identified counterparts in other wavelengths. This has motivated numerous attempts to discover GRB counterparts (for a review see [117, 118]). This is a difficult task - it was not known what to expect and where and when to look for it.

The search for counterparts is traditionally divided to efforts to find a flaring (burst), a fading or a quiescent counterpart. Fading counterparts - afterglow - have been recently discovered by BeppoSAX and as expected this discovery has revolutionized GRB studies. This allowed also the discovery of host galaxies in several cases, which will be discussed in the following section 2.9. Soft X-ray flaring (simultaneous with the GRB) was discovered in several bursts but it is an ambiguous question whether this should be considered as a part of the GRB itself or is it

a separate component. Flaring has not been discovered in other wavelengths yet. Quiescent counter parts were not discovered either.

Most cosmological models suggest that GRBs are in a host galaxy. If so then deep searches within the small error boxes of some GRBs localized by the IPN system should reveal the host galaxy. until the discovery of GRB afterglow these searches have yielded only upper limits on the magnitudes of possible hosts. This has lead to what is called the "No Host" Problem. Schaefer *et al.* conducted searches in the near and far infrared [119] using IRAS, in radio using the VLA [120] and in archival optical photographs [121] and have found only upper limits and no clear counterpart candidates. Similar results from multiple wavelength observations have been obtained by Hurley *et al.* [67]. Vrba, Hartmann & Jennings [122] have monitored the error boxes of seven bursts for five year. They did not find any unusual objects. As for the "no host" problem this authors, as well as Luginbuhl *et al.* [123] and Larson, McLean & Becklin [124] concluded, using the standard galaxy luminosity function, that there are enough dim galaxies in the corresponding GRB error boxes which could be the hosts of cosmological burst and therefore, there is no "no host" problem.

More recently Larson & McLean [125] monitored in the infrared nine of the smallest error boxes of burst localized by the IPN with a typical error boxes of eight arc-min<sup>2</sup>. They found in all error boxes at least one bright galaxy with  $K \leq 15.5$ . However, the error boxes are too large to discern between the host galaxy and unrelated background galaxies. Schaefer *et al.* [126], searched the error boxes of five GRBs using the HST. Four of these are smaller boxes with a size of  $\sim 1$  arc-min<sup>2</sup>. They searched but did not find any unusual objects with UV excess, variability, parallax or proper motion. They have found only faint galaxies. For the four small error boxes the luminosity upper limits of the host galaxy are 10-100 times smaller than the luminosity of an  $L_*$  galaxy. Band & Hartmann [127] concluded that the error boxes of Larsen & McLean [125] are too large to discriminate between the presence or the absence of host galaxies. However, they find that the absence of host galaxies in the Schaefer *et al.* [126] data is significant, at the  $2 \cdot 10^{-6}$  level. Suggesting that there are no bright hosts.

This situation has drastically changed and the "no host" problem has disappeared with afterglow observations. These observations have allowed for an accurate position determination and to identification of host galaxies for several GRBs. Most of these host galaxies are dim with magnitude  $24.4 < R < 25.8$ . This support the conclusions of the earlier studies that GRBs are not associated with bright galaxies and definitely not with cores of such galaxies (ruling out for example AGN type models). These observations are consistent with GRBs rate being either a constant or being proportional to the star formation rate [128]. According to this analysis it is not surprising that most hosts are detected at  $R \sim 25$ . However, though these two models are consistent with the current data both predict the existence of host galaxies brighter than 24 mag, which were not observed so far. One could say now that the "no host" problem has been replaced by the "no bright host" problem. But this may not be a problem but rather

an indication on the nature of the sources.

The three GRBs with measured cosmological redshifts lie in host galaxies with a strong evidence for star formation. These galaxies display prominent emission lines from line associated with star-formation. In all three cases the strength of those lines is high for galaxies of comparable magnitude and redshift [16, 129, 130, 131, 128]. The host of GRB980703, for example, show a star forming rate of  $\sim 10M_{\odot}\text{yr}^{-1}$  or higher with a lower limit of  $7M_{\odot}\text{yr}^{-1}$  [129]. For most GRBs with afterglow the host galaxy was detected but no emission or absorption lines were found and no redshift was measured. This result is consistent with the hypothesis that all GRBs are associated with star-forming galaxies. For those hosts that are at redshift  $1.3 < z < 2.5$  the corresponding emission lines are not observed as for this redshift range no strong lines are found in the optical spectroscopic window [131].

The simplest conclusion of the above observations is that all GRBs are associated with star forming regions. Still one has to keep in mind that those GRBs on which this conclusion was based had a strong optical afterglow, which not all GRBs show. It is possible that the conditions associated with star forming regions (such as high interstellar matter density - or the existance of molecular clouds) are essential for the appearance of strong optical afterglow and not for the appearance of the GRB itself.

### 2.9. Afterglow

GRB observations were revolutionized on February 28, 1997 by the Italian-Dutch satellite BeppoSAX [132] that discovered an X-ray counterpart to GRB970228 [10]. GRB970228 was a double peaked GRB. The first peak which lasted  $\sim 15\text{sec}$  was hard. It was followed, 40 seconds later, by a much softer second peak, which lasted some  $\sim 40\text{sec}$ . The burst was detected by the GRBM (Gamma-Ray Burst Monitor) as well as by the WFC (Wide Field Camera). The WFC, which has a  $40^{\circ} \times 40^{\circ}$  field of view detected soft X-rays simultaneously with both peaks. Eight hours latter the NFI (Narow Field Instrument) was pointed towards the burst's directions and detected a continuous X-ray emission. The accurate position determined by BeppoSAX enabled the identification of an optical afterglow [11] - a 20 magnitude point source adjacent to a red nebulae. HST observations [133] revealed that the nebula adjacent to the source is roughly circular with a diameter of  $0''.8$ . The diameter of the nebula is comparable to the one of galaxies of similar magnitude found in the Hubble Deep Field, especially if one takes into account a possible visual extinction in the direction of GRB970228 of at least one magnitude [134].

Following X-ray detections by BeppoSAX [10, 135], ROSAT [136] and ASCA [137] revealed a decaying X-ray flux  $\propto t^{-1.33 \pm 0.11}$  (see Fig. 5). The decaying flux can be extrapolated as a power law directly to the X-ray flux of the second peak (even though this extrapolation requires some care in determining when is  $t = 0$ ).

The optical emission also depicts a decaying flux [138] (see fig. 6. The source could not be observed from late March 97 until early September 1997. When it was observed again, on Sept. 4th by HST [139, 131] it was found that the optical nebulosity does not decay and the point source shows no proper motion, refuting earlier sugges-

tions. The visual magnitude of the nebula on Sept. 4th was  $25.7 \pm 0.25$  compared with  $V = 25.6 \pm 0.25$  on March 26th and April 7th. The visual magnitude of the point source on Sept. 4th was ( $V = 28.0 \pm 0.25$ ), which is consistent with a decay of the flux as  $t^{-1.14 \pm 0.05}$  [131]. In spite of extensive efforts no radio emission was detected and one can set an upper limit of  $\sim 10\mu\text{Jy}$  to the radio emission at 8.6 Ghz [140].

GRB970508 was detected by both BATSE in  $\gamma$ -rays [141] and BeppoSAX in X-rays [142] on 8 May 1997. The  $\gamma$ -ray burst lasted for  $\sim 15\text{sec}$ , with a  $\gamma$ -ray fluence of  $\sim 3 \times 10^{-6}\text{ergs/cm}^{-2}$ . Variable emission in X-rays, optical [12, 143, 144, 145, 146, 147] and radio [13, 148] followed the  $\gamma$ -rays. The spectrum of the optical transient taken by Keck revealed a set of absorption lines associated with Fe II and Mg II and O II emission line with a redshift  $z = 0.835$  [14]. A second absorption line system with  $z = 0.767$  is also seen. These lines reveal the existence of an underlying, dim galaxy host. HST images [149, 150] and Keck observations [130] show that this host is very faint ( $R = 25.72 \pm 0.2$  mag), compact ( $\leq 1$  arcsec) dwarf galaxy at  $z = 0.835$  and nearly coincident on the sky with the transient.

The optical light curve peaks at around 2 days after the burst. Assuming isotropic emission (and using  $z = 0.835$  and  $H=100\text{km/sec/Mpc}$ ) this peak flux corresponds to a luminosity of  $a \text{ few} \times 10^{45}\text{ergs/sec}$ . The flux decline shows a continuous power law decay  $\propto t^{-1.27 \pm 0.02}$  [151, 152, 153, 154, 130]. After about 100 days the light curve begun to flatten as the transient faded and become weaker than the host [153, 155, 156, 157]. Integration of this light curve results in an overall emission of  $a \text{ few} \times 10^{50}$  ergs in the optical band. Radio emission was observed, first, one week after the burst [13] (see Fig. 8). This emission showed intensive oscillations which were interpreted as scintillation [158]. The subsequent disappearance of these oscillations after about three weeks enabled Frail *et al.* [13] to estimate the size of the fireball at this stage to be  $\sim 10^{17}\text{cm}$ . This was supported by the indication that the radio emission was initially optically thick [13], which yields a similar estimate to the size [25].

GRB970828 was a strong GRB that was detected by BATSE on August 28, 1997. Shortly afterwards RXTE [159, 160] focused on the approximate BATSE position and discovered X-ray emission. This X-ray emission determined the position of the burst to within an elliptical error box with  $5' \times 2'$ . However, in spite of enormous effort no variable optical counterpart brighter than  $R=23.8$  that has changed by more than 0.2 magnitude was detected [161]. There was also no indication of any radio emission. Similarly X-ray afterglow was detected from several other GRBs (GRB970615, GRB970402, GRB970815, GRB980519) with no optical or radio emission.

Seventeen GRBs have been detected with arcminute positions by July 22, 1998: fourteen by the WFC of BeppoSAX and three by the All-Sky Monitor (ASM) on board the Rossi X-ray Timing Explorer (RXTE). Of these seventeen burst, thirteen were followed up within a day in X-rays and all those resulted in good candidates for X-ray afterglows. We will not discuss all those here (see table 4 for a short summary of some of the properties). Worth mentioning are however, GRB971214, GRB980425

and GRB980703.

GRB971214 was a rather strong burst. It was detected on December 14.9 UT 1997 [162]. Its optical counterpart was observed with a magnitude  $21.2 \pm 0.3$  on the I band by Halpern *et al.*, [163] on Dec. 15.47 UT twelve hours after the burst. It was observed one day later on Dec. 16.47 with I magnitude 22.6. Kulkarni *et al.* [15] obtained a spectrum of the host galaxy for GRB971214 and found a redshift of  $z=3.418!$  With a total fluence of  $1.09 \times 10^{-5}$  ergs  $\text{cm}^{-2}$  [164] this large redshift implies, for isotropic emission,  $\Omega = 1$  and  $H_0 = 65 \text{ km/sec/Mpc}$ , an energy release of  $\sim 10^{53}$  ergs in  $\gamma$ -rays alone<sup>4</sup>. The familiar value of  $3 \times 10^{53}$  [15] is obtained for  $\Omega = 0.3$  and  $H_0 = 0.55 \text{ km/sec/Mpc}$ .

GRB980425 was a moderately weak burst with a peak flux of  $3 \pm 0.3 \times 10^{-7}$  ergs  $\text{cm}^{-2} \text{ sec}^{-1}$ . It was a single peak burst with a rise time of 5 seconds and a decay time of about 25 seconds. The burst was detected by BeppoSAX (as well as by BATSE) whose WFC obtained a position with an error box of  $8'$ . Inspection of an image of this error box taken by the New Technology Telescope (NTT) revealed a type Ic supernova SN1998bw that took place more or less at the same time as the GRB [151]. Since the probability for a chance association of the SN and the GRB is only  $1.1 \times 10^{-4}$  it is likely that this association is real. The host galaxy of this supernova (ESO 184-G82) has a redshift of  $z = 0.0085 \pm 0.0002$  putting it at a distance of  $38 \pm 1 \text{ Mpc}$  for  $H=67 \text{ km/sec Mpc}$ . The corresponding  $\gamma$ -ray energy is  $5 \times 10^{47}$  ergs. With such a low luminosity it is inevitable that if the association of this burst with the supernova is real it must correspond to a new and rare subgroup of GRBs.

GRB980703 was a very strong burst with an observed gamma-ray fluence of  $(4.59 \pm 0.42) \times 10^{-5}$  ergs  $\text{cm}^{-2}$  [166]. Keck observations revealed that the host galaxy has a redshift of  $z = 0.966$ . The corresponding energy release (for isotropic emission,  $\Omega = 0.2$  and  $H_0 = 65 \text{ km sec}^{-1}/\text{Mpc}$ ) is  $\sim 10^{53}$  ergs [129].

## 2.10. Repetition?

Quashnock and Lamb [167] suggested that there is evidence from the data in the BATSE 1B catalog for repetition of bursts from the same source. If true, this would severely constrain most GRB models. In particular, it would rule out any other model based on a 'once in lifetime' catastrophic event. This claim has been refuted by several authors [168, 169] and most notably by the analysis of the 2B data [170] and 3B data [171].

A unique group of four bursts - "the gang of four" - emerged from the same position on the sky within two days [68]. One of those bursts (the third burst GRB961029a) was extremely strong, one of the strongest observed by BATSE so far. Consequently it was observed by the IPN network as well, and its position is known accurately. The other three (GRB961027a, GRB961027b and GRB961029d) were detected only by BATSE. The precise position of one burst is within the  $1\sigma$  circles of the three other bursts. However, two of the bursts are almost  $3\sigma$  away from each other. Is this a clear cut case of repetition? It is difficult to assign a unique statistical significance to this question as the significance depends critically on the *a priori* hypothesis that one tests. Furthermore, the time

difference between the first and the last bursts is less than two days. This is only one order of magnitude longer than the longest burst observed beforehand. It might still be possible that all those bursts came from the same source and that they should be considered as one long burst.

## 2.11. Correlations with Abell Clusters, Quasars and Supernovae

Various attempts to search for a correlation between GRBs and other astronomical objects led to null result. For example, Blumenthal & Hartmann [172] found no angular correlation between GRBs and nearby galaxies. They concluded that if GRBs are cosmological then they must be located at distances larger than 100Mpc. Otherwise, they would have shown a positive correlation with the galaxy distribution.

The only exception is the correlation (at 95% confidence level) between GRBs at the 3B catalog and Abell clusters [77, 173]. This correlation has been recently confirmed by Kompaneetz & Stern [174]. The correlation is strongest for a subgroup of strong GRBs whose position is accurately known. Comparison of the rich clusters auto-correlation with the cross-correlation found suggests that  $\sim 26 \pm 15\%$  of the accurate position GRBs sub-sample members are located within  $600 \text{ h}^{-1}\text{Mpc}$ . Recently Schartel *et al.* [176] found that a group of 134 GRBs with position error radius smaller than  $1.8^\circ$  are correlated with radio quiet quasars. The probability of such correlation by chance coincidence is less than 0.3%.

It should be stressed that this correlation does not imply that there is a direct association between GRBs and Abell clusters, such as would have been if GRBs would have emerged from Abell clusters. All that it means is that GRBs are distributed in space like the large scale structure of the universe. Since Abell clusters are the best tracers of this structure they are correlated with GRBs. Therefore the lack of excess Abell Clusters in IPN error boxes (which are much smaller than BATSE's error boxes) [175] does not rule out this correlation.

## 2.12. $V/V_{max}$ , Count and Peak Flux Distributions

The limiting fluence observed by BATSE is  $\approx 10^{-7}$  ergs/ $\text{cm}^2$ . The actual fluence of the strongest bursts is larger by two or three orders of magnitude. A plot of the number of bursts vs. the peak flux depicts clearly a paucity of weak bursts. This is manifested by the low value of  $\langle V/V_{max} \rangle$ , a statistic designed to measure the distribution of sources in space [177]. A sample of the first 601 bursts has  $\langle V/V_{max} \rangle = .328 \pm 0.012$ , which is  $14\sigma$  away from the homogeneous flat space value of 0.5 [178]. Correspondingly, the peak count distribution is incompatible with a homogeneous population of sources in Euclidean space. It is compatible, however, with a cosmological distribution (see Fig. 10). The distribution of short bursts has a larger  $\langle V/V_{max} \rangle$  and it is compatible with a homogeneous Euclidean distribution [77, 78, 79].

## 3. THE DISTANCE SCALE

<sup>4</sup>This value depends also on the spectral shape of the burst.

burst	X-ray detection	O	R	$\gamma$ -ray fluence in [ergs/cm <sup>2</sup> ]	redshift	total energy in [ergs]
GRB970228	BeppoSAX	+	-	$1 \times 10^{-5}$	-	-
GRB970508	BeppoSAX	+	+	$2 \times 10^{-6}$	0.835	$2 \times 10^{51}$
GRB970616	BeppoSAX	-	-	$4 \times 10^{-5}$	-	-
GRB970815	RXTE	-	-	$1 \times 10^{-5}$	-	-
GRB970828	RXTE	-	-	$7 \times 10^{-5}$	-	-
GRB971214	RXTE	+	+	$1 \times 10^{-5}$	3.418	$1 \times 10^{53}$
GRB971227	BeppoSAX	-	-	$9 \times 10^{-7}$	-	-
GRB980326	BeppoSAX	-	-	$1 \times 10^{-6}$	-	-
GRB980329	BeppoSAX	+	+	$5 \times 10^{-5}$	-	-
GRB980425	BeppoSAX	+	+	$4 \times 10^{-6}$	0.0085	$7 \times 10^{47}$
GRB980515	BeppoSAX	-	-	$1 \times 10^{-6}$	-	-
GRB980519	BeppoSAX	+	+	$3 \times 10^{-5}$	-	-
GRB980703	RXTE	+	+	$5 \times 10^{-5}$	0.966	$1 \times 10^{53}$

Table 1: Observational data of several GRBs for which afterglow was detected. The two columns O and R indicate whether emission was detected in the optical and radio, respectively. The total energy of the burst is estimated through the observed fluence and redshift, assuming spherical emission and a flat  $\Omega = 1$ ,  $\Lambda = 0$  universe with  $H_0 = 65$ Km/sec/Mpc.

### 3.1. Redshift Measurements.

The measurements of redshifts of several GRB optical counterparts provide the best and the only direct distance estimates for GRBs. Unfortunately these measurements are available only for a few bursts.

### 3.2. The Angular Distribution

Even before these redshift measurements there was a strong evidence that GRBs originate from cosmological distances. The observed angular distribution is incompatible with a galactic disk distribution unless the sources are at distances less than 100pc. However, in this case we would expect that  $\langle V/V_{max} \rangle = 0.5$  corresponding to a homogeneous distribution [177] while the observations yield  $\langle V/V_{max} \rangle = 0.33$ .

A homogeneous angular distribution could be produced if the GRB originate from the distant parts of the galactic halo. Since the solar system is located at  $d = 8.5$ kpc from the galactic center such a population will necessarily have a galactic dipole of order  $d/R$ , where  $R$  is a typical distance to a GRB [179]. The lack of an observed dipole strongly constrain this model. Such a distribution of sources is incompatible with the distribution of dark matter in the halo. The typical distance to the GRBs must of the order of 100kpc to comply with this constraint. For example, if one considers an effective distribution that is confined to a shell of a fixed radius then such a shell would have to be at a distance of 100kpc in order to be compatible with current limits on the dipole [180].

### 3.3. Interpretation of the Peak Flux Distribution

The counts distribution or the Peak flux distribution of the bursts observed by BATSE show a paucity of weak burst. A homogeneous count distribution, in an Euclidean space should behave like:  $N(C) \propto C^{-3/2}$ , where  $N(C)$  is the number of bursts with more than  $C$  counts (or counts per second). The observed distribution is much flatter (see Fig. 10). This fact is reflected by the low  $\langle V/V_{max} \rangle$  value of the BATSE data: there are fewer distant sources than expected.

The observed distribution is compatible with a cosmological distribution of sources. A homogeneous cosmological distribution displays the observed trend - a paucity of weak bursts relative to the number expected in a Euclidean distribution. In a cosmological population four factors combine to make distant bursts weaker and by this to reduce the rate of weak bursts: (i) K correction - the observed photons are red-shifted. As the photon number decreases with energy this reduces the count rate of distant bursts for a detector at a fixed energy range. (ii) The cosmological time dilation causes a decrease (by a factor  $1+z$ ) in the rate of arrival of photons. For a detector, like BATSE, that measures the count rate within a given time window this reduces the detectability of distant bursts. (iii) The rate of distant bursts also decreases by a factor  $1+z$  and there are fewer distant bursts per unit of time (even if the rate at the comoving frames does not change). (iv) Finally, the distant volume element in a cosmological model is different than the corresponding volume element in a Euclidean space. As could be expected, all these effects are significant only if the typical red-shift to the sources is of order unity or larger.

The statistics  $\langle V/V_{max} \rangle$  is a weighted average of the distribution  $N(> f)$ . Already in 1992 Piran [56] compared the theoretical estimate of this statistics to the observed one and concluded that the typical redshift of the bursts observed by BATSE is  $z_{max} \sim 1$ . Later Fenimore *et al.* [200] compared the sensitivity of PVO (that observes  $N(> f) \propto f^{-3/2}$ ) with the sensitivity of BATSE and concluded that  $z_{max}(\text{BATSE}) \sim 1$  (the maximal  $z$  from which bursts are detected by BATSE). This corresponds to a peak luminosity of  $\sim 10^{50}$  ergs/sec. Other calculations based on different statistical methods were performed by Horack & Emslie [186], Loredo & Wasserman [181, 182], Rutledge *et al.* [185] Cohen & Piran [183] and Mészáros and collaborators [187, 188, 189, 190] and others. In particular Loredo & Wassermann [181, 182] give an extensive discussion of the statistical methodology involved.

Consider a homogeneous cosmological distribution of sources with a peak luminosity  $L$ , that may vary from

one source to another. It should be noted that only the luminosity per unit solid angle is accessible by these arguments. If there is significant beaming, as inferred [25], the distribution of total luminosity may be quite different. The sources are emitting bursts with a count spectrum:  $N(\nu)d\nu = (L/h\bar{\nu})\tilde{N}(\nu)d\nu$ , where  $h\bar{\nu}$ , is the average energy. The observed peak (energy) flux in a fixed energy range,  $[E_{min}, E_{max}]$  from a source at a red-shift  $z$  is:

$$f(L, z) = \frac{(1+z)}{4\pi d_l^2(z)} \frac{L}{h\bar{\nu}} \int_{E_{min}}^{E_{max}} \tilde{N}[\nu(1+z)]h\nu(1+z)h\nu d\nu \quad (3)$$

where  $d_l(z)$  is the luminosity distance [184].

To estimate the number of bursts with a peak flux larger than  $f$ ,  $N(> f)$ , we need the luminosity function,  $\psi(L, z)$ : the number of bursts per unit proper (comoving) volume per unit proper time with a given luminosity at a given red-shift. Using this function we can write:

$$N(> f) = 4\pi \int_0^\infty \int_0^{z(f, L)} \psi(L, z) \frac{d_l^2}{(1+z)^3} \frac{dr_p(z)}{dz} dz dL \quad (4)$$

where the red-shift,  $z(f, L)$ , is obtained by inverting Eq. 3 and  $r_p(z)$  is the proper distance to a red-shift  $z$ . For a given theoretical model and a given luminosity function we can calculate the theoretical distribution  $N(f)$  and compare it with the observed one.

A common simple model assumes that  $\psi(L, z) = \phi(L)\rho(z)$  - the luminosity does not change with time, but the rate of events per unit volume per unit proper time may change. In this case we have:

$$N(> f) = 4\pi \int_0^\infty \phi(L) \int_0^{z(f, L)} \rho(z) \frac{d_l^2}{(1+z)^3} \frac{dr_p(z)}{dz} dz dL \quad (5)$$

The emitted spectrum,  $N(\nu)$ , can be estimated from the observed data. The simplest shape is a single power law (Eq. 2), with  $\alpha = 1.5$  or  $\alpha = 1.8$  [85]. More elaborate studies have used the Band *et al.* [84] spectrum or even a distribution of such spectra [185].

The cosmic evolution function  $\rho(z)$  and the luminosity function  $\phi(L)$  are unknown. To proceed one has to choose a functional shape for these functions and characterize it by a few parameters. Then using maximum likelihood, or some other technique, estimate these parameters from the data.

A simple characterization of  $\rho(z)$  is:

$$\rho(z) = \rho_0(1+z)^{-\beta}. \quad (6)$$

Similarly the simplest characterization of the luminosity is as standard candles:

$$\phi(L) = \delta(L - L_0), \quad (7)$$

with a single parameter,  $L_0$ , or equivalently  $z_{max}$ , the maximal  $z$  from which the source is detected (obtained by inverting Eq. 3 for  $f = f_{min}$  and  $L = L_0$ ).

There are two unknown cosmological parameters: the closure parameter,  $\Omega$ , and the cosmological constant  $\Lambda$ . With the luminosity function given by Eqs. (5) and (6) we have three unknown parameters that determine the bursts'

distribution:  $L_0$ ,  $\rho_0$ ,  $\beta$ . We calculate the likelihood function over this five dimensional parameter space and find the range of acceptable models (those whose likelihood function is not less than 1% of the maximal likelihood). We then proceed to perform a KS (Kolmogorov-Smirnov) test to check whether the model with the maximal likelihood is an acceptable fit to the data.

The likelihood function is practically independent of  $\Omega$  in the range:  $0.1 < \Omega < 1$ . It is also insensitive to the cosmological constant  $\Lambda$  (in the range  $0 < \Lambda < 0.9$ , in units of the critical density). This simplifies the analysis as we are left only with the intrinsic parameters of the bursts' luminosity function.

There is an interplay between evolution (change in the bursts' rate) and luminosity. Fig. 9 depicts the likelihood function in the  $(z_{max}, \beta)$  plane for sources with a varying intrinsic rate. The banana shaped contour lines show that a population whose rate is independent of  $z$  ( $\beta = 0$ ) is equivalent to a population with an increasing number of bursts with cosmological time ( $\beta > 0$ ) with a lower  $L_0$  (lower  $z_{max}$ ). This tendency saturates at high intrinsic evolution (large  $\beta$ ), for which the limiting  $z_{max}$  does not go below  $\approx .5$  and at very high  $L_0$ , for which the limiting  $\beta$  does not decrease below -1.5. This interplay makes it difficult to constraint the red shift distribution of GRB using the peak flux distribution alone. For completeness we quote here "typical" results based on standard candles, no evolution and an Einstein-DeSitter cosmology [183].

Recall that  $\langle V/V_{max} \rangle$  of the short bursts distribution is rather close to the homogeneous Euclidean value of 0.5. This means that when analyzing the peak flux distribution one should analyze separately the long and the short bursts [183]. For long bursts (bursts with  $t_{90} > 2$  sec) the likelihood function peaks at  $z_{max} = 2.1$  (see Fig. 10) [183]. The allowed range at a 1% confidence level is:  $1.4 < z_{max} < 3.1$  ( $z_{max}^{(\alpha=2)} = 1.5^{(+.7)}_{(-.4)}$  for  $\alpha = 2$ ). The maximal red-shift,  $z_{max} = 2.1^{(+1.1)}_{(-0.7)}$ , corresponds, with an estimated BATSE detection efficiency of  $\approx 0.3$ , to  $2.3^{(+1.1)}_{(-0.7)} \cdot 10^{-6}$  events per galaxy per year (for a galaxy density of  $10^{-2}h^3$  Mpc $^{-3}$ ; [192]). The rate per galaxy is independent of  $H_0$  and is only weakly dependent on  $\Omega$ . For  $\Omega = 1$  and  $\Lambda = 0$  the typical energy of a burst with an observed fluence,  $F$ , is  $7^{(+11)}_{(-4)} \cdot 10^{50} (F/10^{-7} \text{ergs/cm}^2)$  ergs. The distance to the sources decreases and correspondingly the rate increases and the energy decreases if the spectral index is 2 and not 1.5. These numbers vary slightly if the bursts have a wide luminosity function.

Short bursts are detected only up to a much nearer distances:  $z_{max}(\text{short}) = 0.4^{+1.1}$ , again assuming standard candles and no source evolution. There is no significant lower limit on  $z_{max}$  for short bursts and their distribution is compatible with a homogeneous non-cosmological one. The estimate of  $z_{max}(\text{short})$  corresponds to a comparable rate of  $6.3^{(+39)}_{(-5.6)} \cdot 10^{-6}$  events per year per galaxy and a typical energy of  $3^{(+39)} \cdot 10^{49} F_{-7}$  ergs (there are no lower limits on the energy or and no upper limit on the rate since there is no lower limit on  $z_{max}(\text{short})$ ). The fact that short bursts are detected only at nearer distances is also reflected by the higher  $\langle V/V_{max} \rangle$  of the population of these bursts [79].

Relatively wide luminosity distributions are allowed by the data [183]. For example, the KS test gives a probability of 80% for a double peaked luminosity distribution with luminosity ratio of 14. These results demonstrate that the BATSE data alone allow a variability of one order of magnitude in the luminosity.

The above considerations should be modified if the rate of GRBs trace the SFR - the star formation rate [193, 194, 195]. The SFR has been determined recently by two independent studies [196, 197, 198]. The SFR peaks at  $z \sim 1.25$ . This is a strongly evolving non monotonic distribution, which is drastically different from the power laws considered so far. Sahu *et al.* [194] find that  $\rho(z) \propto SFR(z)$  yields  $N(> f)$  distribution that is compatible with the observed one (for  $q_0 = 0.2$ ,  $H_0 = 50 \text{ km/sec}^{-1} \text{Mpc}^{-1}$ ) for a narrow luminosity distribution with  $L_\gamma = 10^{51} \text{ ergs/sec}$ . Wijers *et al.* [195] find that the implied peak luminosity is higher  $L_\gamma = 8.3 \cdot 10^{51} \text{ ergs/sec}$  and it corresponds to a situation in which the dimmest bursts observed by BATSE originate from  $z \approx 6$ !

The direct red-shift measure of GRB970508 [14] agrees well with estimates made previously using peak-flux count statistics ([200, 182, 183]). The red-shift of GRB971214,  $z = 3.418$ , and of GRB980703,  $z = 0.966$ , and the implied luminosities disagree with these estimates. A future detection of additional red-shifts for other bursts will enable us to estimate directly the luminosity function of GRBs. It will also enable us to determine the evolution of GRBs. Krumholz *et al.* [199] and Hogg & Fruchter [128] find that with a wide luminosity function both models of a constant GRB rate and a GRB rate following the star formation rate are consistent with the peak flux distribution and with the observed redshift of the three GRBs.

### 3.4. Time Dilation

Norris *et al.* [202, 203] examined 131 long bursts (with a duration longer than 1.5s) and found that the dimmest bursts are longer by a factor of  $\approx 2.3$  compared to the bright ones. With our canonical value of  $z_{max} = 2.1$  the bright bursts originate at  $z_{bright} \approx 0.2$ . The corresponding expected ratio due to cosmological time dilation, 2.6, is in agreement with this measurement. Fenimore and Bloom [204] find, on the other hand, that when the fact that the burst's duration decreases as a function of energy as  $\Delta t \approx E^{-0.5}$  is included in the analysis, this time dilation corresponds to  $z_{max} > 6$ . This would require a strong negative intrinsic evolution:  $\beta \approx -1.5 \pm 0.3$ . Alternatively, this might agree with the model in which the GRB rate follows the SFR [193, 195] which gives  $z_{max} \approx 6$ . Cohen & Piran [191] suggested a way to perform the time dilation, spectral and red shift analysis simultaneously. Unfortunately current data are insufficient for this purpose.

## 4. THE COMPACTNESS PROBLEM AND RELATIVISTIC MOTION.

The key to understanding GRBs lies, I believe, in understanding how GRBs bypass the compactness problem. This problem was realized very early on in one form by Ruderman [205] and in another way by Schmidt [206]. Both used it to argue that GRBs cannot originate from cosmological distances. Now, we understand that GRBs

are cosmological and special relativistic effects enable us to overcome this constraint.

The simplest way to see the compactness problem is to estimate the average opacity of the high energy gamma-ray to pair production. Consider a typical burst with an observed fluence,  $F$ . For a source emitting isotropically at a distance  $D$  this fluence corresponds to a total energy release of:

$$E = 4\pi D^2 F = 10^{50} \text{ ergs} \left( \frac{D}{3000 \text{ Mpc}} \right)^2 \left( \frac{F}{10^{-7} \text{ ergs/cm}^2} \right). \quad (8)$$

Cosmological effects change this equality by numerical factors of order unity that are not important for our discussion. The rapid temporal variability on a time scale  $\delta T \approx 10 \text{ msec}$  implies that the sources are compact with a size,  $R_i < c\delta T \approx 3000 \text{ km}$ . The observed spectrum (see section 2.3) contains a large fraction of high energy  $\gamma$ -ray photons. These photons (with energy  $E_1$ ) could interact with lower energy photons (with energy  $E_2$ ) and produce electron-positron pairs via  $\gamma\gamma \rightarrow e^+e^-$  if  $\sqrt{E_1 E_2} > m_e c^2$  (up to an angular factor). Denote by  $f_p$  the fraction of photon pairs that satisfy this condition. The average optical depth for this process is [207, 208, 209]:

$$\tau_{\gamma\gamma} = \frac{f_p \sigma_T F D^2}{R_i^2 m_e c^2},$$

or

$$\tau_{\gamma\gamma} = 10^{13} f_p \left( \frac{F}{10^{-7} \text{ ergs/cm}^2} \right) \left( \frac{D}{3000 \text{ Mpc}} \right)^2 \left( \frac{\delta T}{10 \text{ msec}} \right)^{-2}, \quad (9)$$

where  $\sigma_T$  is the Thompson cross-section. This optical depth is very large. Even if there are no pairs to begin with they will form rapidly and then these pairs will Compton scatter lower energy photons, resulting in a huge optical depth for all photons. However, the observed non-thermal spectrum indicates with certainty that the sources must be optically thin!

An alternative calculation is to consider the optical depth of the highest energy photons (say a GeV photon) to pair production with the lower energy photons. The observation of GeV photons shows that they are able to escape freely. In other words it means that this optical depth must be much smaller than unity [210, 211]. This consideration leads to a slightly stronger but comparable limit on the opacity.

The compactness problem stems from the assumption that the size of the sources emitting the observed radiation is determined by the observed variability time scale. There won't be a problem if the source emitted the energy in another form and it was converted to the observed gamma-rays at a large distance,  $R_X$ , where the system is optically thin and  $\tau_{\gamma\gamma}(R_X) < 1$ . A trivial solution of this kind is based on a weakly interacting particle, which is converted in flight to electromagnetic radiation. The only problem with this solution is that there is no known particle that can play this role (see, however [213]).

### 4.1. Relativistic Motion

Relativistic effects can fool us and, when ignored, lead to wrong conclusions. This happened thirty years ago

when rapid variability implied “impossible” temperatures in extra-galactic radio sources. This puzzle was resolved when it was suggested [214, 215] that these objects reveal ultra-relativistic expansion. This was confirmed later by VLBA measurements of superluminal jets with Lorentz factors of order two to ten. This also happened in the present case. Consider a source of radiation that is moving towards an observer at rest with a relativistic velocity characterized by a Lorentz factor,  $\gamma = 1/\sqrt{1-v^2/c^2} \gg 1$ . Photons with an observed energy  $h\nu_{obs}$  have been blue shifted and their energy at the source was  $\approx h\nu_{obs}/\gamma$ . Since the energy at the source is lower fewer photons have sufficient energy to produce pairs. Now the observed fraction  $f_p$ , of photons that could produce pairs is not equal to the fraction of photons that could produce pairs at the source. The latter is smaller by a factor  $\gamma^{-2\alpha}$  (where  $\alpha$  is the high energy spectral index) than the observed fraction. At the same time, relativistic effects allow the radius from which the radiation is emitted,  $R_e < \gamma^2 c \delta T$  to be larger than the original estimate,  $R_e < c \delta T$ , by a factor of  $\gamma^2$ . We have

$$\tau_{\gamma\gamma} = \frac{f_p}{\gamma^{2\alpha}} \frac{\sigma_T F D^2}{R_e^2 m_e c^2},$$

or

$$\tau_{\gamma\gamma} \approx \frac{10^{13}}{\gamma^{(4+2\alpha)}} f_p \left( \frac{F}{10^{-7} \text{ergs/cm}^2} \right) \left( \frac{D}{3000 \text{Mpc}} \right)^2 \left( \frac{\delta T}{10 \text{msec}} \right)^{-2} \quad (10)$$

where the relativistic limit on  $R_e$  was included in the second line. The compactness problem can be resolved if the source is moving relativistically towards us with a Lorentz factor  $\gamma > 10^{13/(4+2\alpha)} \approx 10^2$ . A more detailed discussion [210, 211] gives comparable limits on  $\gamma$ . Such extreme-relativistic motion is larger than the relativistic motion observed in any other celestial source. Extragalactic super-luminal jets, for example, have Lorentz factors of  $\sim 10$ , while the known galactic relativistic jets [216] have Lorentz factors of  $\sim 2$  or less.

The potential of relativistic motion to resolve the compactness problem was realized in the eighties by Goodman [217], Paczyński [53] and Krolik and Pier [218]. There was, however, a difference between the first two approaches and the last one. Goodman [217] and Paczyński [53] considered relativistic motion in the dynamical context of fireballs, in which the relativistic motion is an integral part of the dynamics of the system. Krolik and Pier [218] considered, on the other hand, a kinematical solution, in which the source moves relativistically and this motion is not necessarily related to the mechanism that produces the burst.

Is a purely kinematic scenario feasible? In this scenario the source moves relativistically as a whole. The radiation is beamed with an opening angle of  $\gamma^{-1}$ . The total energy emitted in the source frame is smaller by a factor  $\gamma^{-3}$  than the isotropic estimate given in Eq. (8). The total energy required, however, is at least  $(Mc^2 + 4\pi F D^2/\gamma^3)\gamma$ , where  $M$  is the rest mass of the source (the energy would be larger by an additional amount  $E_{th}\gamma$  if an internal energy,  $E_{th}$ , remains in the source after the burst has been emitted). For most scenarios that one can imagine  $Mc^2\gamma \gg (4\pi/\gamma^2)FD^2$ . The kinetic energy is much larger than the observed energy of the burst and the process is extremely (energetically) wasteful. Generally, the

total energy required is so large that the model becomes infeasible.

The kinetic energy could be comparable to the observed energy if it also powers the observed burst. This is the most energetically-economical situation. It is also the most conceptually-economical situation, since in this case the  $\gamma$ -ray emission and the relativistic motion of the source are related and are not two independent phenomena. This will be the case if GRBs result from the slowing down of ultra-relativistic matter. This idea was suggested by Mészáros, and Rees [27, 219] in the context of the slowing down of fireball accelerated material [220] by the ISM and by Narayan, et al. [28] and independently by Rees and Mészáros [29] and Paczyński and Xu [30] in the context of self interaction and internal shocks within the fireball. It is remarkable that in both cases the introduction of energy conversion was motivated by the need to resolve the “Baryonic Contamination” problem (which we discuss in the next section). If the fireball contains even a small amount of baryons all its energy will eventually be converted to kinetic energy of those baryons. A mechanism was needed to recover this energy back to radiation. However, it is clear now that the idea is much more general and it is an essential part of any GRB model regardless of the nature of the relativistic energy flow and of the specific way it slows down.

Assuming that GRBs result from the slowing down of a relativistic bulk motion of massive particles, the rest mass of the ultra-relativistic particles is:

$$M = \frac{\theta^2 F D^2}{\gamma \epsilon_c c^2} \approx 10^{-6} M_{\odot} \epsilon_c^{-1} \left( \frac{\theta^2}{4\pi} \right) \times \left( \frac{F}{10^{-7} \text{ergs/cm}^2} \right) \left( \frac{D}{3000 \text{Mpc}} \right)^2 \left( \frac{\gamma}{100} \right)^{-1} \quad (11)$$

where  $\epsilon_c$  is the conversion efficiency and  $\theta$  is the opening angle of the emitted radiation. We see that the allowed mass is very small. Even though a way was found to convert back the kinetic energy of the baryons to radiation (via relativistic shocks) there is still a “baryonic contamination” problem. Too much baryonic mass will slow down the flow and it won’t be relativistic.

#### 4.2. Relativistic Beaming?

Radiation from relativistically moving matter is beamed in the direction of the motion to within an angle  $\gamma^{-1}$ . In spite of this the radiation produced by relativistically moving matter can spread over a much wider angle. This depends on the geometry of the emitting region. Let  $\theta_M$  be the angular size of the relativistically moving matter that emits the burst. The beaming angle  $\theta$  will be  $\theta_M$  if  $\theta_M > \gamma^{-1}$  and  $\gamma^{-1}$  otherwise. Thus if  $\theta_M = 4\pi$  - that is if the emitting matter has been accelerated spherically outwards from a central source (as will be the case if the source is a spherical fireball) - the burst will be isotropic even though each observer will observe radiation coming only from a very small region (see Fig. 11). The radiation will be beamed into  $\gamma^{-1}$  only if the matter has been accelerated along a very narrow beam. The opening angle can also have any intermediate value if it emerges from a beam with an opening angle  $\theta > \gamma^{-1}$ , as will be the

case if the source is an anisotropic fireball [222, 223] or an electromagnetic accelerator with a modest beam width.

Beaming requires, of course, an event rate larger by a ratio  $4\pi/\theta^2$  compared to the observed rate. Observations of about one burst per  $10^{-6}$  year per galaxy implies one event per hundred years per galaxy if  $\theta \approx \gamma^{-1}$  with  $\gamma$  given by the compactness limit of  $\sim 100$ .

## 5. AN OVERVIEW OF THE GENERIC MODEL

It is worthwhile to summarize now the essential features of the generic GRB model that arose from the previous discussion. Compactness has led us to the requirement of relativistic motion, with a Lorentz factor  $\gamma \geq 100$ . Ockham's razor and the desire to limit the total energy have lead us to the idea that the observed gamma-rays arise in the process of slowing down of a relativistic energy flow, at a stage that the motion of the emitting particles is still highly relativistic.

This leads us to the generic picture mentioned earlier and to the suggestion that GRBs are composed of a three stage phenomenon: (i) a compact inner hidden "engine" that produces a relativistic energy flow, (ii) the energy transport stage and (iii) the conversion of this energy to the observed prompt radiation. One may add a forth stage (iv) conversion of the remaining energy to radiation in other wavelengths and on a longer time scale - the "afterglow".

### 5.1. Models for The Energy Flow

The simplest mode of relativistic energy flow is in the form of kinetic energy of relativistic particles. A variant that have been suggested is based on the possibility that a fraction of the energy is carried by Poynting flux [224, 225, 226, 69, 227] although in all models the power must be converted to kinetic energy somewhere. The energy flow of  $\sim 10^{50}$  ergs/sec from a compact object whose size is  $\lesssim 10^7$  cm requires a magnetic field of  $10^{15}$  Gauss or higher at the source. This large value might be reached in stellar collapses of highly magnetized stars or amplified from smaller fields magnetohydrodynamically [69]. Overall the different models can be characterized by two parameters: the ratio of the kinetic energy flux to the Poynting flux and the location of the energy conversion stage ( $\approx 10^{12}$  cm for internal conversion or  $\approx 10^{16}$  cm for external conversion). This is summarized in Table 5.1. In the following section we will focus on the simplest possibility, that is of a kinetic energy flux.

### 5.2. Models for The Energy Conversion

Within the baryonic model the energy transport is in the form of the kinetic energy of a shell of relativistic particles with a width  $\Delta$ . The kinetic energy is converted to "thermal" energy of relativistic particles via shocks. These particles then release this energy and produce the observed radiation. There are two modes of energy conversion (i) External shocks, which are due to interaction with an external medium like the ISM. (ii) Internal shocks that arise due to shocks within the flow when fast moving particles catch up with slower ones. Similar division to external and internal energy conversion occurs within other models for the energy flow.

External shocks arise from the interaction of the shell with external matter. The typical length scale is the Sedov length,  $l \equiv (E/n_{ism}m_p c^2)^{1/3}$ . The rest mass energy within a sphere of radius  $l$ , equals the energy of the shell. Typically  $l \sim 10^{18}$  cm. As we see later (see section 8.7.1) relativistic external shocks (with a Newtonian reverse shock) convert a significant fraction of their kinetic energy at  $R_\gamma = l/\gamma^{2/3} \approx 10^{15} - 10^{16}$  cm, where the external mass encountered equals  $\gamma^{-1}$  of the shell's mass. Relativistic shocks (with a relativistic reverse shock) convert their energy at  $R_\Delta = l^{3/4} \Delta^{1/4} \approx 10^{16}$  cm, where the shock crosses the shell.

Internal shocks occur when one shell overtakes another. If the initial separation between the shells is  $\delta$  and both move with a Lorentz factor  $\gamma$  with a difference of order  $\gamma$  these shocks take place at:  $\delta\gamma^2$ . A typical value is  $10^{12} - 10^{14}$  cm.

### 5.3. Typical Radii

In table 5.3 we list the different radii that arise in the fireball evolution.

Figs. 12 and 13 (from [228]) depict a numerical solution of a fireball from its initial configuration at rest to its final Sedov phase.

## 6. FIREBALLS

Before turning to the question of how is the kinetic energy of the relativistic flow converted to radiation we ask is it possible to produce the needed flows? More specifically, is it possible to accelerate particles to relativistic velocities? It is remarkable that a relativistic particle flow is almost the unavoidable outcome of a "fireball" - a large concentration of energy (radiation) in a small region of space in which there are relatively few baryons. The relativistic fireball model was proposed by Goodman [217] and by Paczyński [53]. They have shown that the sudden release of a large quantity of gamma ray photons into a compact region can lead to an opaque photon-lepton "fireball" through the production of electron-positron pairs. The term "fireball" refers here to an opaque radiation-plasma whose initial energy is significantly greater than its rest mass. Goodman [217] considered the sudden release of a large amount of energy,  $E$ , in a small volume, characterized by a radius,  $R_i$ . Such a situation could occur in an explosion. Paczyński [53] considered a steady radiation and electron-positron plasma wind that emerges from a compact region of size  $R_i$  with an energy,  $E$ , released on a time scale significantly larger than  $R_i/c$ . Such a situation could occur if there is a continuous source that operates for a while. As it will become clear later both configurations display, in spite of the seemingly large difference between them, the same qualitative behavior. Both Goodman [217] and Paczyński [53] considered a pure radiation fireballs in which there are no baryons. Later Shemi & Piran [220] and Paczyński [221] considered the effect of a baryonic load. They showed that under most circumstances the ultimate outcome of a fireball with a baryonic load will be the transfer of all the energy of the fireball to the kinetic energy of the baryons. If the baryonic load is sufficiently small the baryons will be accelerated to a

	Kinetic Energy Dominated	Kinetic Energy and Poynting Flux	Poynting Flux Dominated
Internal conversion	[28, 29, 18]	[224]	[225, 69, 227]
External conversion	[27, 219]	-	[226, 69]

Table 2: General Scheme for Energy Transport

$R_i$	Initial Radius	$c\delta t$	$\approx 10^7 - 10^8 \text{ cm}$
$R_\eta$	Matter dominates	$R_i\eta$	$\approx 10^9 \text{ cm}$
$R_{pair}$	Optically thin to pairs	$[(3E/4\pi R_i^3 a)^{1/4}/T_p]R_i$	$\approx 10^{10} \text{ cm}$
$R_e$	Optically thin	$(\sigma_T E/4\pi m_p c^2 \eta)^{1/2}$	$\approx 10^{13} \text{ cm}$
$R_\delta$	Internal collisions	$\delta\gamma^2$	$\approx 10^{12} - 10^{14} \text{ cm}$
$R_\gamma$	External Newtonian Shocks	$l\gamma^{-2/3}$	$\approx 10^{16} \text{ cm}$
$R_\Delta$	External Relativistic shocks	$l^{3/4}\Delta^{1/4}$	$\approx 10^{16} \text{ cm}$
$l$ or $L$	Non relativistic external shock	$l^{(a)} \text{ or } l\gamma^{-1/3} (b)$	$\approx 10^{17} - 10^{18} \text{ cm}$
1	Sedov Length	$l = (3E/4\pi n_{ism} m_p c^2)^{1/3}$	$\approx 10^{18} \text{ cm}$

Table 3: Critical Radii (a) - adiabatic fireball; (b) - radiative fireball

relativistic velocity with  $\gamma \approx E/M$ . If it is large the net result will be a Newtonian flow with  $v \simeq \sqrt{2E/M}$ .

### 6.1. A simple model

The evolution of a homogeneous fireball can be understood by a simple analogy to the Early Universe [220]. Consider, first, a pure radiation fireball. If the initial temperature is high enough pairs will form. Because of the opacity due to pairs, the radiation cannot escape. The pairs-radiation plasma behaves like a perfect fluid with an equation of state  $p = \rho/3$ . The fluid expands under of its own pressure. As it expands it cools with  $T \propto R^{-1}$  ( $T$  being the local temperature and  $R$  the radius). The system resembles quite well a part of a Milne Universe in which gravity is ignored. As the temperature drops below the pair-production threshold the pairs annihilate. When the local temperature is around 20keV the number of pairs becomes sufficiently small, the plasma becomes transparent and the photons escape freely to infinity. In the meantime the fireball was accelerated and it is expanding relativistically outwards. Energy conservation (as viewed from the observer frame) requires that the Lorentz factor that corresponds to this outward motion satisfies  $\gamma \propto R$ . The escaping photons, whose local energy (relative to the fireball's rest frame) is  $\approx 20\text{keV}$  are blue shifted. An observer at rest detects them with a temperature of  $T_{obs} \propto \gamma T$ . Since  $T \propto R^{-1}$  and  $\gamma \propto R$  we find that the observed temperature,  $T_{obs}$ , approximately equals  $T_0$ , the initial temperature. The observed spectrum, is however, almost thermal [217] and it is still far from the one observed in GRBs.

In addition to radiation and  $e^+e^-$  pairs, astrophysical fireballs may also include some baryonic matter which may be injected with the original radiation or may be present in an atmosphere surrounding the initial explosion. These baryons can influence the fireball evolution in two ways. The electrons associated with this matter increase the opacity, delaying the escape of radiation. Initially, when the local temperature  $T$  is large, the opacity is dominated by  $e^+e^-$  pairs [217]. This opacity,  $\tau_p$ , decreases exponentially with decreasing temperature, and falls to unity

when  $T = T_p \approx 20\text{keV}$ . The matter opacity,  $\tau_b$ , on the other hand decreases only as  $R^{-2}$ , where  $R$  is the radius of the fireball. If at the point where  $\tau_p = 1$ ,  $\tau_b$  is still  $> 1$ , then the final transition to  $\tau = 1$  is delayed and occurs at a cooler temperature.

More importantly, the baryons are accelerated with the rest of the fireball and convert part of the radiation energy into bulk kinetic energy. The expanding fireball has two basic phases: a radiation dominated phase and a matter dominated phase. Initially, during the radiation dominated phase the fluid accelerates with  $\gamma \propto R$ . The fireball is roughly homogeneous in its local rest frame but due to the Lorentz contraction its width in the observer frame is  $\Delta \approx R_i$ , the initial size of the fireball. A transition to the matter dominated phase takes place when the fireball has a size

$$R_\eta = \frac{R_i E}{M c^2} \approx 10^9 \text{ cm} R_{i7} E_{52} (M/5 \cdot 10^{-6} M_\odot)^{-1} \quad (12)$$

and the mean Lorentz factor of the fireball is  $\gamma \approx E/Mc^2$ . We have defined here  $E_{52} \equiv E/10^{52} \text{ ergs}$  and  $R_{i7} \equiv R_i/10^7 \text{ cm}$ . After that, all the energy is in the kinetic energy of the matter, and the matter coasts asymptotically with a constant Lorentz factor.

The matter dominated phase is itself further divided into two sub-phases. At first, there is a frozen-coasting phase in which the fireball expands as a shell of fixed radial width in its own local frame, with a width  $\sim \bar{\gamma} R_i \sim (E/Mc^2) R_i$ . Because of Lorentz contraction the shell appears to an observer with a width  $\Delta \approx R_i$ . Eventually, when the size of the fireball reaches  $R_s = \Delta \gamma^2 \approx 10^{11} \text{ cm} (\Delta/10^7 \text{ cm}) (\gamma/100)^2$  variability in  $\gamma$  within the fireball results in a spreading of the fireball which enters the coasting-expanding phase. In this final phase, the width of the shell grows linearly with the size of the shell,  $R$ :

$$\Delta(R) \approx R/\gamma^2 \approx 10^7 \text{ cm} \left( \frac{R}{10^{11} \text{ cm}} \right) \left( \frac{\gamma}{100} \right)^{-2} \quad (13)$$

$$\text{for } R > R_s = 10^{11} \text{ cm} \left( \frac{R_i}{10^7 \text{ cm}} \right) \left( \frac{\gamma}{100} \right)^2.$$

The initial energy to mass ratio,  $\eta = (E/Mc^2)$ , determines the order of these transitions. There are two critical values for  $\eta$  [220]:

$$\eta_{pair} = \left( \frac{3\sigma_T^2 E \sigma T_p^4}{4\pi m_p^2 c^4 R_i} \right)^{1/2} \approx 3 \cdot 10^{10} E_{52}^{1/2} R_{i7}^{-1/2} \quad (14)$$

and

$$\eta_b = \left( \frac{3\sigma_T E}{8\pi m_p c^2 R_i^2} \right)^{1/3} \approx 10^5 E_{52}^{1/3} R_{i7}^{-2/3} \quad (15)$$

These correspond to four different types of fireballs:

- (i) **A Pure Radiation Fireball** ( $\eta_{pair} < \eta$ ): The effect of the baryons is negligible and the evolution is of a pure photon-lepton fireball. When the temperature reaches  $T_p$ , the pair opacity  $\tau_p$  drops to 1 and  $\tau_b \ll 1$ . At this point the fireball is radiation dominated ( $E > Mc^2$ ) and most of the energy escapes as radiation.
- (ii) **Electron Dominated Opacity** ( $\eta_b < \eta < \eta_{pair}$ ): In the late stages, the opacity is dominated by free electrons associated with the baryons. The comoving temperature decreases far below  $T_p$  before  $\tau$  reaches unity. However, the fireball continues to be radiation dominated and most of the energy still escapes as radiation.
- (iii) **Relativistic Baryonic Fireball** ( $1 < \eta < \eta_b$ ): The fireball becomes matter dominated before it becomes optically thin. Most of the initial energy is converted into bulk kinetic energy of the baryons, with a final Lorentz factor  $\gamma_f \approx (E/Mc^2)$ . This is the most interesting situation for GRBs.
- (iv) **Newtonian Fireball** ( $\eta < 1$ ): This is the Newtonian regime. The rest energy exceeds the radiation energy and the expansion never becomes relativistic. This is the situation, for example in supernova explosions in which the energy is deposited into a massive envelope.

## 6.2. Extreme-Relativistic Scaling Laws.

The above summary describes the qualitative features of a roughly homogeneous expanding fireball. Surprisingly similar scaling laws exists also for inhomogeneous fireballs [229] as well as for relativistic winds [53]. Consider a spherical fireball with an arbitrary radial distribution of radiation and matter. Under optically thick conditions the radiation and the relativistic leptons (with energy density  $e$ ) and the matter (with baryon mass density  $\rho$ ) at each radius behave like a single fluid, moving with the same velocity. The pressure,  $p$ , and the energy density,  $e$ , are related by  $p = e/3$ . We can express the relativistic conservation equations of baryon number, energy and momentum using characteristic coordinates:  $r$  and  $s \equiv t - r$  as [229]:

$$\frac{1}{r^2} \frac{\partial}{\partial r} (r^2 \rho u) = - \frac{\partial}{\partial s} \left( \frac{\rho}{\gamma + u} \right), \quad (16)$$

$$\frac{1}{r^2} \frac{\partial}{\partial r} (r^2 e^{3/4} u) = - \frac{\partial}{\partial s} \left( \frac{e^{3/4}}{\gamma + u} \right), \quad (17)$$

$$\frac{1}{r^2} \frac{\partial}{\partial r} \left[ r^2 \left( \rho + \frac{4}{3} e \right) u^2 \right] = - \frac{\partial}{\partial s} \left[ \left( \rho + \frac{4}{3} e \right) \frac{u}{\gamma + u} \right] + \frac{1}{3} \left[ \frac{\partial e}{\partial s} - \frac{\partial \rho}{\partial r} \right], \quad (18)$$

where  $u = u^r = \sqrt{\gamma^2 - 1}$ , and we use units in which  $c = 1$  and the mass of the particles  $m = 1$ . The derivative  $\partial/\partial r$  now refers to constant  $s$ , i.e. is calculated along a characteristic moving outward at the speed of light. After a short acceleration phase we expect that the motion of a fluid shell will become highly relativistic ( $\gamma \gg 1$ ). If we restrict our attention to the evolution of the fireball from this point on, we may treat  $\gamma^{-1}$  as a small parameter and set  $\gamma \approx u$ , which is accurate to order  $O(\gamma^{-2})$ . Then, under a wide range of conditions the quantities on the right-hand sides of Eqs. 16-18 are significantly smaller than those on the left. When we neglect the right hand sides of Eqs. 16-18 the problem becomes effectively only  $r$  dependent. We obtain the following conservation laws for each fluid shell:

$$r^2 \rho \gamma = \text{const.}, \quad r^2 e^{3/4} \gamma = \text{const.}, \quad r^2 \left( \rho + \frac{4}{3} e \right) \gamma^2 = \text{const.} \quad (19)$$

A scaling solution that is valid in both the radiation-dominated and matter-dominated regimes, as well as in the transition zone in between, can be obtained by combining the conserved quantities in Eq. 19 appropriately. Let  $t_0$  be the time and  $r_0$  be the radius at which a fluid shell in the fireball first becomes ultra-relativistic, with  $\gamma \gtrsim \text{few}$ . We label various properties of the shell at this time by a subscript 0, e.g.  $\gamma_0$ ,  $\rho_0$ , and  $e_0$ . Defining the auxiliary quantity  $D$ , where

$$\frac{1}{D} \equiv \frac{\gamma_0}{\gamma} + \frac{3\gamma_0 \rho_0}{4e_0 \gamma} - \frac{3\rho_0}{4e_0}, \quad (20)$$

we find that

$$r = r_0 \frac{\gamma_0^{1/2} D^{3/2}}{\gamma^{1/2}}, \quad \rho = \frac{\rho_0}{D^3}, \quad e = \frac{e_0}{D^4}. \quad (21)$$

These are parametric relations which give  $r$ ,  $\rho$ , and  $e$  of each fluid shell at any time in terms of the  $\gamma$  of the shell at that time. The parametric solution 21 describes both the radiation-dominated and matter-dominated phases of the fireball within the frozen pulse approximation. That is as long as the fireball does not spread due to variation in the velocity.

## 6.3. The Radiation-Dominated Phase

Initially the fireball is radiation dominated. For  $\gamma \ll (e_0/\rho_0)\gamma_0$ , the first term in Eq 20 dominates and we find  $D \propto r$ ,  $\gamma \propto r$ , recovering the radiation-dominated scaling:

$$\gamma \propto r, \quad \rho \propto r^{-3}, \quad e \propto r^{-4}. \quad (22)$$

The scalings of  $\rho$  and  $e$  given in Eq. 22 correspond to those of a fluid expanding uniformly in the comoving frame. Indeed, all three scalings in Eq. 22 can be derived for a homogeneous radiation dominated fireball by noting the analogy with an expanding universe.

Type	$\eta = E/Mc^2$	$M$
Pure Radiation	$\eta_{pair} < \eta$	$M < M_{pair} = 10^{-12} M_\odot E_{52}^{1/2} R_{i7}^{1/2}$
Electrons Opacity	$\eta_b < \eta < \eta_{pair}$	$M_{pair} < M < M_b = 2 \cdot 10^{-7} M_\odot E_{52}^{2/3} R_{i7}^{2/3}$
Relativistic Baryons	$1 < \eta < \eta_b$	$M_b < M < 5 \cdot 10^{-3} M_\odot E_{52}$
Newtonian	$\eta < 1$	$5 \cdot 10^{-4} M_\odot E_{52} < M$

Table 4: *Different Fireballs*

Although the fluid is approximately homogeneous in its own frame, because of Lorentz contraction it appears as a narrow shell in the observer frame, with a radial width given by  $\Delta r \sim r/\gamma \sim \text{constant} \sim R_i$ , the initial radius of the fireball, or the initial width of the specific shell under discussion when we consider a continuous wind. We can now go back to Eqs. 16-18 and set  $\partial/\partial s \sim \gamma/r$ . We then find that the terms we neglected on the right hand sides of these equations are smaller than the terms on the left by a factor  $\sim 1/\gamma$ . Therefore, the conservation laws 19 and the scalings 22 are valid so long as the radiation-dominated fireball expands ultra-relativistically with large  $\gamma$ . The only possible exception is in the very outermost layers of the fireball where the pressure gradient may be extremely steep and  $\partial/\partial s$  may be  $\gg \gamma/r$ . Ignoring this minor deviation, we interpret Eq. 19 and the constancy of the radial width  $\Delta r$  in the observer frame to mean that the fireball behaves like a pulse of energy with a frozen radial profile, accelerating outward at almost the speed of light.

#### 6.4. The Matter-Dominated Phase

The radiation dominated regime extends out to a radius  $r \sim (e_0/\rho_0)r_0$ . At larger radii, the first and last terms in Eq. 20 become comparable and  $\gamma$  tends to its asymptotic value of  $\gamma_f = (4e_0/3\rho_0 + 1)\gamma_0$ . This is the matter dominated regime. (The transition occurs when  $4e/3 = \rho$ , which happens when  $\gamma = \gamma_f/2$ .) In this regime,  $D \propto r^{2/3}$ , leading to the scalings:

$$\gamma \rightarrow \text{constant}, \quad \rho \propto r^{-2}, \quad e \propto r^{-8/3}. \quad (23)$$

The modified scalings of  $\rho$  and  $e$  arise because the fireball now moves with a constant radial width in the comoving frame. (The steeper fall-off of  $e$  with  $r$  is because of the work done by the radiation through tangential expansion.) Moreover, since  $e \ll \rho$ , the radiation has no important dynamical effect on the motion and produces no significant radial acceleration. Therefore,  $\gamma$  remains constant on streamlines and the fluid coasts with a constant asymptotic radial velocity. Of course, since each shell moves with a velocity that is slightly less than  $c$  and that is different from one shell to the next, the frozen pulse approximation on which Eq. 19 is based must ultimately break down at some large radius.

#### 6.5. Spreading

At very late times in the matter-dominated phase the frozen pulse approximation begins to break down. In this stage the radiation density  $e$  is much smaller than the matter density  $\rho$ , and the Lorentz factor,  $\gamma$ , tends to a constant value  $\gamma_f$  for each shell. We may therefore neglect the term

$-(1/3)(\partial e/\partial r)$  in Eq. 18 and treat  $\gamma$  and  $u$  in Eqs. 16-18 as constants. We then find that the flow moves strictly along the characteristic,  $\beta_f t - r = \text{constant}$ , so that each fluid shell coasts at a constant radial speed,  $\beta_f = u_f/\gamma_f$ . We label the baryonic shells in the fireball by a Lagrangian coordinate  $\tilde{R}$ , moving with a fixed Lorentz factor  $\gamma_f(\tilde{R})$ , and let  $t_c$  and  $r_c$  represent the time and radius at which the coasting phase begins, which corresponds essentially to the point at which the fluid makes the transition from being radiation dominated to matter dominated. We then find

$$r(t, \tilde{R}) - r_c(\tilde{R}) = \frac{\sqrt{\gamma_f^2(\tilde{R}) - 1}}{\gamma_f(\tilde{R})} (t - t_c(\tilde{R})) \approx \left[ 1 - \frac{1}{2\gamma_f^2(\tilde{R})} \right] [t - t_c(r)]. \quad (24)$$

The separation between two neighboring shells separated by a Lagrangian distance  $\Delta\tilde{R}$  varies during the coasting phase as

$$\left[ \frac{d(\partial r/\partial \tilde{R})}{dt} \right] \Delta\tilde{R} = \left[ \frac{1}{\gamma_f(\tilde{R})^3} \frac{\partial \gamma_f}{\partial \tilde{R}} \right] \Delta\tilde{R}. \quad (25)$$

Thus the width of the pulse at time  $t$  is  $\Delta r(t) \approx \Delta r_c + \Delta\gamma_f(t - t_c)/\bar{\gamma}_f^3 \approx R_i + (t - t_c)/\gamma_f^2$ , where  $\Delta r_c \sim R_i$  is the width of the fireball when it begins coasting,  $\bar{\gamma}_f$  is the mean  $\gamma_f$  in the pulse, and  $\Delta\gamma_f \sim \bar{\gamma}_f$  is the spread of  $\gamma_f$  across the pulse. From this result we see that within the matter dominated coasting phase there are two separate regimes. So long as  $t - t_c < \bar{\gamma}_f^2 R_i$ , we have a frozen-coasting phase in which  $\Delta r$  is approximately constant and the frozen pulse approximation is valid. In this regime the scalings in Eq. 23 are satisfied. However, when  $t - t_c > \bar{\gamma}_f^2 R_i$ , the fireball switches to an expanding-coasting phase where  $\Delta r \propto t - t_c$  and the pulse width grows linearly with time. In this regime the scaling of  $\rho$  reverts to  $\rho \propto r^{-3}$ , and, if the radiation is still coupled to the matter,  $e \propto r^{-4}$ .

#### 6.6. Optical Depth

Independently of the above considerations, at some point during the expansion, the fireball will become optically thin. For a pure fireball this happens when the local temperature drops to about 20keV at:

$$R_{pair} \approx 10^{10} \text{ cm } E_{52}^{1/4} R_{i7}^{-3/4} \quad (26)$$

In a matter dominated fireball the optical depth is usually determined by the ambient electrons. In this case the

fireball becomes optically thin at:

$$R_e = \left( \frac{\sigma_T E}{4\pi m_p c^2 \eta} \right)^{1/2} \approx 6 \cdot 10^{13} \text{ cm} \sqrt{E_{52}} (\eta/100)^{-1}. \quad (27)$$

From this stage on the radiation and the baryons no longer move with the same velocity and the radiation pressure vanishes, leading to a breakdown of Eqs. 16-18. Any remaining radiation will escape freely now. The baryon shells will coast with their own individual velocities. If the fireball is already in the matter dominated coasting phase there will be no change in the propagation of the baryons. However, if the fireball is in the radiation dominated phase when it becomes optically thin, then the baryons will switch immediately to a coasting phase. This transition radius,  $R_e$  has another crucial role in the fireball evolution. It is the minimal radius in which energy conversion and generation of the observed GRB can begin. Photons produced at  $R < R_e$  cannot escape.

### 6.7. Anisotropic Fireballs

It is unlikely that a realistic fireball will be spherically symmetric. In fact strong deviation from spherical symmetry are expected in the most promising neutron star merger model, in which the radiation is expected to emerge through funnels along the rotation axis. The initial motion of the fireball might be fairly complex but once  $\gamma \gg 1$  the motion of each fluid element decouples from the motion of its neighbors with angular distance larger than  $\gamma^{-1}$ . This motion can be described by the same asymptotic solution, as if it is a part of a spherical shell. We define the angular range over which different quantities vary as  $\theta$ . Additionally now the motion is not radially outwards and  $u^r \neq u$ . We define the spread angle  $\phi$  as  $u^r \equiv u \cos \phi$ . The spherical fireball equations hold locally if:

$$\gamma^{-1} < \theta \quad \text{and} \quad \phi \ll \sqrt{2}/\gamma. \quad (28)$$

## 7. TEMPORAL STRUCTURE AND KINEMATIC CONSIDERATIONS

General kinematic considerations impose constraints on the temporal structure produced when the energy of a relativistic shell is converted to radiation. The enormous variability of the temporal profiles of GRBs from one burst to another in contrast to the relatively regular spectral characteristics, was probably the reason that until recently this aspect of GRBs was largely ignored. However, it turns out that the observed temporal structure sets a strong constraint on the energy conversion models [20, 230]. GRBs are highly variable (see section 2.2) and some configurations cannot produce such temporal profiles.

### 7.1. Time-scales

Special relativistic effects determine the observed duration of the burst from a relativistic shell (see Fig. 14).

- **The Radial Time Scale:**  $T_{radial}$ : Consider an infinitely thin relativistic shell with a Lorentz factor  $\gamma_E$  (the subscript E is for the emitting region). Let  $R_E$  be a typical radius characterizing the emitting region (in the observer frame) such that most of the

emission takes place between  $R_E$  and  $2R_E$ . The observed duration between the first photon (emitted at  $R_E$ ) and last one (emitted at  $2R_E$ ) is [205, 18]:

$$T_{radial} \cong R_E/2\gamma_E^2 c. \quad (29)$$

- **The Angular Time Scale:**  $T_{ang}$ : Because of relativistic beaming an observer sees up to solid angle of  $\gamma_E^{-1}$  from the line of sight. Two photons emitted at the same time and radius  $R_E$ , one on the line of sight and the other at an angle of  $\gamma_E^{-1}$  away travel different distances to the observer. The difference lead to a delay in the arrival time by [205, 18, 230] :

$$T_{ang} = R_E/2\gamma_E^2 c. \quad (30)$$

Clearly this delay is relevant only if the angular width of the emitting region,  $\theta$  is larger than  $\gamma_E^{-1}$ .

In addition there are two other time scales that are determined by the flow of the relativistic particles. These are:

- **Intrinsic Duration:**  $\Delta T$ : The duration of the flow. This is simply the time in which the source that produces the relativistic flow is active.  $\Delta T = \Delta/c$ , where  $\Delta$  is the width of the relativistic wind (measured in the observer's rest frame). For an explosive source  $\Delta \approx R_i$ . However,  $\Delta$  could be much larger for a wind. The observed duration of the burst must be longer or equal to  $\Delta/c$
- **Intrinsic Variability**  $\delta T$ : The time scale on which the inner source varies and produces a subsequent variability with a length scale  $\delta = c\delta T$  in the flow. Naturally,  $\delta T$  sets a lower limit to the variability time scale observed in any burst.

Clearly  $\Delta$  and  $\delta$  must satisfy:

$$R_{source} \leq \delta \leq \Delta \quad (31)$$

Finally we have to consider the cooling time scale.

- **The Cooling Time Scale:**  $T_{cool}$  This is the difference in arrival time of photons while the shocked material cools measured in the rest frame of an observer at rest at infinity. It is related to the local cooling time,  $e/P$  (where  $e$  is the internal energy density and  $P$  is the power radiated per unit volume) in the fluid's rest frame by:

$$T_{cool} = e/P\gamma_E \quad (32)$$

Note that this differs from the usual time dilation which gives  $\gamma_E e/P$ .

For synchrotron cooling there is a unique energy dependence of the cooling time scale on frequency:  $T_{cool}(\nu) \propto \nu^{-1/2}$  [103] (see Eq. 59). If  $T_{cool}$  determines the variability we will have  $\delta T(\nu) \propto \nu^{-1/2}$ . This is remarkably close to the observed relation:  $\delta T \propto \nu^{-0.4}$  [102]. Quite generally  $T_{cool}$  is shorter than the hydrodynamics time scales [103, 232, 69]. However, during the late stages of an afterglow,  $T_{cool}$  becomes the longest time scale in the system.

## 7.2. Angular Spreading and External shocks

Comparison of Eqs. 29 and 30 (using  $\Delta R_E \lesssim R_E$ ) reveals that  $T_{ang} \approx T_{radial}$ . As long as the shell's angular width is larger than  $\gamma^{-1}$ , any temporal structure that could have arisen due to irregularities in the properties of the shell or in the material that it encounters will be spread on a time given by  $T_{ang}$ . This means that  $T_{ang}$  is the minimal time scale for the observed temporal variability:  $\delta T \geq T_{ang}$ .

Comparison with the intrinsic time scales yields two cases:

$$T = \begin{cases} T_{ang} = R_E/c\gamma_E^2 & \text{if } \Delta < R_E/\gamma_E^2 \quad (\text{Type-I}); \\ \Delta/c & \text{otherwise} \quad (\text{Type-II}). \end{cases} \quad (33)$$

In Type-I models, the duration of the burst is determined by the emission radius and the Lorentz factor. It is independent of  $\Delta$ . This type of models include the standard “external shock model” [27, 18, 233] in which the relativistic shell is decelerated by the ISM, the relativistic magnetic wind model [226] in which a magnetic Poynting flux runs into the ISM, or the scattering of star light by a relativistic shell [234, 235].

In Type-II models, the duration of the burst is determined by the thickness of the relativistic shell,  $\Delta$  (that is by the duration that the source is active and produces the relativistic wind). The angular spreading time (which depends on the the radius of emission) is shorter and therefore irrelevant. These models include the “internal shock model” [28, 29, 30], in which different parts of the shell are moving with different Lorentz factor and therefore collide with one another. A magnetic dominated version is given by Thompson [224].

The majority of GRBs have a complex temporal structure (e.g. section 2.2) with  $\mathcal{N} \equiv T/\delta T$  of order 100. Consider a Type-I model. Angular spreading means that at any given moment the observer sees a whole region of angular width  $\gamma_E^{-1}$ . Any variability in the emission due to different conditions in different radii on a time scale smaller than  $T_{ang}$  is erased unless the angular size of the emitting region is smaller than  $\gamma_E^{-1}$ . Thus, such a source can produce only a smooth single humped burst with  $\mathcal{N} = 1$  and no temporal structure on a time-scale  $\delta T < T$ . Put in other words a shell, of a Type-I model, and with an angular width larger than  $\gamma_E^{-1}$  cannot produce a variable burst with  $\mathcal{N} \gg 1$ . This is the angular spreading problem.

On the other hand a Type-II model contains a thick shell  $\Delta > R_E/\gamma_E^2$  and it can produce a variable burst. The variability time scale, is again limited  $\delta T > T_{ang}$  but now it can be shorter than the total duration  $T$ . The duration of the burst reflects the time that the “inner engine” operates. The variability reflects the radial inhomogeneity of the shell which was produced by the source (or the cooling time if it is longer than  $\delta/c$ ). The observed temporal variability provides an upper limit to the scale of the radial inhomogeneities in the shell and to the scale in which the “inner engine” varies. This is a remarkable conclusion in view of the fact that the fireball hides the “inner engine”.

Can an external shock give rise to a Type-II behavior? This would have been possible if we could set the parameters of the external shock model to satisfy  $R_E \leq 2\gamma_E c\delta T$ . As discussed in 8.7.1 the deceleration radius for a thin shell

with an initial Lorentz factor  $\gamma$  is given by

$$R_E = l\gamma^{-2/3}, \quad (34)$$

and the observed duration is  $l\gamma^{-8/3}/c$ . The deceleration is gradual and the Lorentz factor of the emitting region  $\gamma_E$  is similar to the original Lorentz factor of the shell  $\gamma$ . It seems that with an arbitrary large Lorentz factor  $\gamma$  we can get a small enough deceleration radius  $R_E$ . However, Eq. 34 is valid only for thin shells satisfying  $\Delta > l\gamma^{-8/3}$  [233]. As  $\gamma$  increases above a critical value  $\gamma \geq \gamma_c = (l/\Delta)^{3/8}$  the shell can no longer be considered thin. In this situation the reverse shock penetrating the shell becomes ultra-relativistic and the shocked matter moves with Lorentz factor  $\gamma_E = \gamma_c < \gamma$  which is independent of the initial Lorentz factor of the shell  $\gamma$ . The deceleration radius is now given by  $R_E = \Delta^{1/4}l^{3/4}$ , and it is independent of the initial Lorentz factor of the shell. The behavior of the deceleration radius  $R_E$  and observed duration as function of the shell Lorentz factor  $\gamma$  is given in Fig. 15 for a shell of thickness  $\Delta = 3 \times 10^{12}$  cm. This emission radius  $R_E$  is always larger than  $\Delta/\gamma_E^2$  - thus an external shock cannot be of type II.

## 7.3. Angular Variability and Other Caveats

In a Type-I model, that is a for a shell satisfying  $\Delta < R_E/\gamma_E^2$ , variability is possible only if the emitting regions are significantly narrower than  $\gamma_E^{-1}$ . The source would emit for a total duration  $T_{radial}$ . To estimate the allowed opening angle of the emitting region imagine two points that emit radiation at the same (observer) time  $t$ . The difference in the arrival time between two photons emitted at  $(R_E, \theta_1)$  and  $(R_E, \theta_2)$  at the same (observer) time  $t$  is:

$$\delta T \approx \frac{R_E|\theta_2^2 - \theta_1^2|}{2c} = \frac{R_E\bar{\theta}|\theta_2 - \theta_1|}{c} = \frac{R_E\bar{\theta}\delta\theta}{c}, \quad (35)$$

where  $\theta$  is the angle from the line of sight and we have used  $\theta_1, \theta_2 \ll 1$ ,  $\bar{\theta} \equiv (\theta_1 + \theta_2)/2$  and  $\delta\theta \equiv |\theta_2 - \theta_1|$ . Since an observer sees emitting regions up to an angle  $\gamma_E^{-1}$  away from the line of sight  $\bar{\theta} \sim \gamma_E^{-1}$ . The size of the emitting region  $r_s = R_E\delta\theta$  is limited by:

$$r_s \leq \gamma_E c \delta T. \quad (36)$$

The corresponding angular size is:

$$\delta\theta \leq \frac{\gamma_E c \delta T}{R_E} = \frac{1}{\mathcal{N}\gamma_E}. \quad (37)$$

Note that Fenimore, Madras and Nayakshin [230] who examined this issue, considered only emitting regions that are directly on the line of sight with  $\bar{\theta} \sim |\theta_2 - \theta_1|$  and obtained a larger  $r_s$  which was proportional to  $R_E^{1/2}$ . However only a small fraction of the emitting regions will be exactly on the line of sight. Most of the emitting regions will have  $\bar{\theta} \sim \gamma_E^{-1}$ , and thus Eq. 36 yields the relevant estimate.

The above discussion suggests that one can produce GRBs with  $T \approx T_{radial} \approx R_E/c\gamma_E^2$  and  $\delta T = T/\mathcal{N}$  if the emitting regions have angular size smaller than  $1/\mathcal{N}\gamma_E \approx 10^{-4}$ . That is, one needs an extremely narrow jet. Relativistic jets are observed in AGNs and even

in some galactic objects, however, their opening angles are of order of a few degrees almost two orders of magnitude larger. A narrow jet with such a small opening angle would be able to produce the observed variability. Such a jet must be extremely cold (in its local rest frame); otherwise its internal pressure will cause it to spread. It is not clear what could produce such a jet. Additionally, for the temporal variability to be produced, either a rapid modulation of the jet or inhomogeneities in the ISM are needed. These two options are presented in Fig. 16.

A second possibility is that the shell is relatively “wide” (wider than  $\gamma_E^{-1}$ ) but the emitting regions are small. An example of this situation is schematically described in Fig. 17. This may occur if either the ISM or the shell itself are very irregular. This situation is, however, extremely inefficient. The area of the observed part of the shell is  $\pi R_E^2/\gamma_E^2$ . The emitting regions are much smaller and to comply with the temporal constraint their area is  $\pi r_s^2$ . For high efficiency all the area of the shell must eventually radiate. The number of emitting regions needed to cover the shell is at least  $(R_E/\gamma_E r_s)^2$ . In Type-I models, the relation  $R_E = 2c\gamma_E^2 T$  holds, and the number of emitting region required is  $4\mathcal{N}^2$ . But a sum of  $4\mathcal{N}^2$  peaks each of width  $1/\mathcal{N}$  of the total duration does not produce a complex time structure. Instead it produces a smooth time profile with small variations, of order  $1/\sqrt{2\mathcal{N}} \ll 1$ , in the amplitude.

In a highly variable burst there cannot be more than  $\mathcal{N}$  sub-bursts of duration  $\delta T = T/\mathcal{N}$ . The corresponding area covering factor (the fraction of radiating area of the shell) and the corresponding efficiency is less than  $1/4\mathcal{N}$ . This result is independent of the nature of the emitting regions: ISM clouds, star light or fragments of the shell. This is the case, for example, in the Shaviv & Dar model [235] where a relativistic iron shell interacts with the starlight of a stellar cluster (a spherical shell interacting with an external fragmented medium). This low efficiency poses a series energy crisis for most (if not all) cosmological models of this kind. In a recent paper Fenimore *et al.* [231] consider other ways, which are based on low surface covering factor, to resolve the angular spreading problems. None seems very promising.

#### 7.4. Temporal Structure in Internal shocks.

Type-II behavior arises naturally in the internal shock model. In this model different shells have different Lorentz factors. These shells collide with each other and convert some of their kinetic energy into internal energy and radiate (Fig. 18). If the emission radius is sufficiently small angular spreading will not erase the temporal variability. This requires  $R_E \leq 2\gamma_E^2 c \delta T$ . This condition is always satisfied as internal shocks take place at  $R_E = R_s \approx \delta \gamma^2$  with  $\gamma_E \simeq \gamma$ . Since  $\delta < \Delta$  we have  $T = \Delta/c > T_{ang} = R_E/2\gamma_E^2 c = \delta/c = \delta T$ . Clearly multiple shells are needed to account for the observed temporal structure. Each shell produces an observed peak of duration  $\delta T$  and the whole complex of shells (whose width is  $\Delta$ ) produces a burst that lasts  $T = \Delta/c$ . The angular spreading time is comparable to the temporal variability produced by the “inner engine”. They determine the observed temporal structure provided that they are longer than the cooling time.

Before concluding that internal shocks can actually produce GRBs we must address two issues. First, can internal shocks produce the observed variable structure? Second, can it be done efficiently? We will address the first question here and the second one in section 8.6 where we discuss energy conversion in internal shocks.

Mochkovitch, Maitia and Marques [32] and Kobayashi, Piran & Sari [33] used a simple model to calculate the temporal profiles produced by an internal shock. According to this model the relativistic flow that produces the shocks is characterized by multiple shells, each of width  $l$  and with a separation  $L$ . The shells are assigned random Lorentz factors (varying in the range  $[\gamma_{min}, \gamma_{max}]$ ) and random density or energy. One can follow the motion of the shell and calculate the time of the binary (two-shell) collisions that take place, until all the shells that could collide have collided and the remaining flow has a monotonically decreasing velocity. The energy generated and the emitted radiation in each binary encounter are then combined to a synthetic sample of a temporal profile.

The emitted radiation from each binary collision will be observed as a single pulse characterized by an amplitude and a width. The amplitude depends on the amount of energy converted to radiation in a given collision (see 8.6). The time scale depends on the cooling time, the hydrodynamic time, and the angular spreading time. The internal energy is radiated via synchrotron emission and inverse Compton scattering. In most of cases, the electrons’ cooling time is much shorter than the hydrodynamic time scale [103, 232, 18] so we consider only the latter two.

The hydrodynamic time scale is determined by the time that the shock crosses the shell, whose width is  $d$ . In fact there are two shocks: a forward shock and a reverse shock. Detailed calculations [33] reveals that this time scale (in the observer’s rest frame) is of order of the light crossing time of the shell, that is:  $d/c$ .

Let the distance between the shells be  $\delta$ . A collision takes place at  $\delta/\gamma^2$  and the angular spreading yields an observed pulse whose width is  $\sim \delta/c$ . If  $\delta > d$  the overall pulse width  $\delta T$  is determined by angular spreading. The shape of the pulse become asymmetric with a fast rise and a slower decline (Fig. 19) which GRBs typically show (see section 2.2). The amplitude of an individual pulse depends on the energy produced in the collision, which we calculate latter in section 8.6.

Typical synthetic temporal profile are shown in Fig. 20. Clearly, internal shocks can produce the observed highly variable temporal profiles, provided that the source of the relativistic particles, the “inner engine”, produces a sufficiently variable wind. Somewhat surprisingly the resulting temporal profile follows, to a large extent, the shape of the pulse emitted by the source. Long bursts require long relativistic winds that last hundred seconds, with a rapid variability on a time scale of a fraction of a second. Thus, unlike previous worries [78, 236] we find that there is some direct information on the “inner engine” of GRBs: It produces the observed complicated temporal structure. This severely constrains numerous models.

## 8. ENERGY CONVERSION

### 8.1. Slowing Down of Relativistic Particles

The cross section for a direct electromagnetic or nuclear interaction between the relativistic particles and the ISM particles is too small to convert efficiently the kinetic energy to radiation. The fireball particles can be slowed down only via some collective interaction such as a collisionless shock. Supernova remnants (SNRs) in which the supernova ejecta is slowed down by the ISM show that collisionless shocks form in somewhat similar circumstances. One can expect that collisionless shocks will form here as well [27, 18].

GRBs are the relativistic analogues of SNRs. In both cases the phenomenon results from the conversion of the kinetic energy of the ejected matter to radiation. Even the total energy involved is comparable. One crucial difference is the amount of ejected mass. SNRs involve a solar mass or more. The corresponding velocity is several thousands kilometers per second, much less than the speed of light. In GRBs, the masses are smaller by several orders of magnitude and with the same energy the matter attains ultra-relativistic velocities. A second crucial difference is that while SNRs result from the interaction of the ejecta with the ISM, GRBs result from internal collisions. The interaction of the ejecta in GRBs with the ISM produces the “afterglow” that follows some GRBs.

The interaction between the SNR ejecta and the ISM takes place on scales of several pc and it is observed for thousands of years. The internal interaction of the relativistic matter in GRBs takes place on a scale of several hundred astronomical units and special relativistic effects reduce the observed time scale to a fraction of a second. The interaction with the ISM that leads to the “afterglow” takes place on a scale of a tenth of a pc. Once more special relativistic effects reduce the observed time scale to several days.

In the following sections I discuss the slowing down of matter due to relativistic shocks. The discussion begins with a general review of relativistic inelastic collisions and continues with the relativistic shock conditions. Then I turn to the radiation processes: synchrotron emission and Inverse Compton. After the general discussion I apply the general results to internal shocks, to external shocks and to the afterglow.

### 8.1.1. Relativistic Inelastic Collisions

Consider a mass (denoted by the subscript  $r$ ) that catches up a slower one (denoted  $s$ ). The two masses collide and merge to form a single mass (denoted  $m$ ). Energy and momentum conservation yield:

$$\begin{aligned} m_r \gamma_r + m_s \gamma_s &= (m_r + m_s + \mathcal{E}/c^2) \gamma_m \\ m_r \sqrt{\gamma_r^2 - 1} + m_s \sqrt{\gamma_s^2 - 1} &= (m_r + m_s + \mathcal{E}/c^2) \sqrt{\gamma_m^2 - 1}, \end{aligned} \quad (38)$$

where  $\mathcal{E}$  is the internal energy generated in the collision (in the rest frame of the merged mass).

There are two interesting limits. First let  $m_s$  be at rest:  $\gamma_s = 1$ . This is the case in external shocks, or in a shock between relativistic ejecta and a non-relativistic material that was ejected from the source before it exploded. Eqs. 39 reveal that a mass:

$$m_s \approx m_r / \gamma_r \ll m_r \quad (39)$$

is needed to yield  $\gamma_m \approx \gamma_r/2$  and  $\mathcal{E} \approx m_r/2$ . The external mass needed to convert half of the kinetic energy is smaller than the original mass by a factor of  $\gamma_r$  [27, 18].

The second case corresponds to an internal collision between shells that are moving at different relativistic velocities:  $\gamma_r \gtrsim \gamma_s \gg 1$ . Eqs. 39 yield:

$$\gamma_m \simeq \sqrt{\frac{m_r \gamma_r + m_s \gamma_s}{m_r / \gamma_r + m_s / \gamma_s}}, \quad (40)$$

The internal energy (in the frame of an external observer) of the merged shell,  $E_{int} = \gamma_m \mathcal{E}$ , is the difference of the kinetic energies before and after the collision:

$$E_{int} = m_r c^2 (\gamma_r - \gamma_m) + m_s c^2 (\gamma_s - \gamma_m). \quad (41)$$

The conversion efficiency of kinetic energy into internal energy is [33, 69]:

$$\epsilon = 1 - \frac{(m_r + m_s) \gamma_m}{(m_r \gamma_r + m_s \gamma_s)}. \quad (42)$$

As can be expected a conversion of a significant fraction of the initial kinetic energy to internal energy requires that the difference in velocities between the shells will be significant:  $\gamma_r \gg \gamma_s$  and that the two masses will be comparable  $m_r \approx m_s$ .

### 8.1.2. Shock Conditions

Quite often the previous estimates based on the approximation that the whole shell behaves as a single object are good enough. However, the time scale between the interaction of different parts of the shell with the ISM may be relatively long (compared to the time scale to collect an external mass  $M/\gamma$ ) and in this case one has to turn to the hydrodynamics of the interaction. This calculation takes into account the shocks that form during the collision.

Consider the situation a cold shell (whose internal energy is negligible compared to the rest mass) that overtakes another cold shell or moves into the cold ISM. Generally, Two shocks form: an outgoing shock that propagates into the ISM or into the external shell, and a reverse shock that propagates into the inner shell, with a contact discontinuity between the shocked material (see Fig. 21). Two quantities determine the shocks’ structure:  $\gamma$ , the Lorentz factor of the motion of the inner shell (denoted 4) relative to the outer one - or the ISM (denoted 1) and the ratio between the particle number densities in these regions,  $f \equiv n_4/n_1$ .

There are three interesting cases: **(i)** Ultra-relativistic shock ( $\gamma \gg 1$ ) with  $f > \gamma^2$ . This happens during the early phase of an external shock or during the very late external shock evolution when there is only a single shock. We call this configuration “Newtonian” because the reverse shock is non-relativistic (or mildly relativistic). In this case the energy conversion takes place in the forward shock: Let  $\gamma_2$  be the Lorentz factor of the motion of the shocked fluid relative to the rest frame of the fluid at 1 (an external observer for interaction with the ISM and the outer shell in case of internal collision) and let  $\bar{\gamma}_3$  be the Lorentz factor of the motion of this fluid relative to the rest frame of the relativistic shell (4).

$$\gamma_2 \approx \gamma \quad ; \quad \bar{\gamma}_3 \approx 1, \quad (43)$$

The particle and energy densities ( $n, e$ ) in the shocked regions satisfy:

$$n_2 \approx 4\gamma n_1, ; e \equiv e_2 = 4\gamma^2 n_1 m_p c^2 ; n_3 = 7n_4, ; e_3 = e. \quad (44)$$

(ii) Later during the propagation of the shell the density ratio decreases and  $f < \gamma^2$ . Both the forward and the reverse shocks are relativistic. The shock equations between regions 1 and 2 yield: [238, 239, 222]:

$$\gamma_2 = f^{1/4} \gamma^{1/2} / \sqrt{2} ; n_2 = 4\gamma_2 n_1 ; e \equiv e_2 = 4\gamma_2^2 n_1 m_p c^2, \quad (45)$$

Similar relations hold for the reverse shock:

$$\bar{\gamma}_3 = f^{-1/4} \gamma^{1/2} / \sqrt{2} ; n_3 = 4\bar{\gamma}_3 n_4. \quad (46)$$

In addition we have  $e_3 = e$  and  $\bar{\gamma}_3 \cong (\gamma/\gamma_2 + \gamma_2/\gamma)/2$  which follow from the equality of pressures and velocity on the contact discontinuity. Comparable amounts of energy are converted to thermal energy in both shocks when both shocks are relativistic. But only a negligible amount of energy is converted to thermal energy in the reverse shock if it is Newtonian [233].

(iii) Internal shocks are characterized by  $f \approx 1$  - both shells have similar densities, and by a Lorentz factor of order of a few ( $2 < \gamma < 10$ ) describing the relative motion of the shells. In this case, for an adiabatic index (4/3) we have:

$$\gamma_2 = \sqrt{(\gamma^2 + 1)/2} \approx \max[1, \sqrt{\gamma/2}] ; \quad (47)$$

$$n_2 = (4\gamma_2 + 3)n_1 \approx 4\gamma_2 n_1 ; e_2 = \gamma_2 n_2 m_p c^2$$

Both shocks are mildly relativistic and their strength depends on the relative Lorentz factors of the two shells.

### 8.1.3. Lorentz Factors in Different Emitting Regions

Before concluding this section and turning to the radiation mechanisms we summarize briefly the different relativistic motions encountered when considering different emitting regions. The relativistic shocks are characterized by  $\gamma_{sh}$  that describes the shock's velocity as well as the "thermal" motion of the shocked particles. It is measured relative to a rest frame in which the unshocked material is at rest. The Lorentz factor of the forward shock is usually different from the Lorentz factor of the reverse shock. The emitting region - the shocked material - moves relativistically relative to an observer at rest at infinity. This is characterized by a Lorentz factor,  $\gamma_E$ . Table 8.1.3 summarizes the different values of  $\gamma_{sh}$  and  $\gamma_E$  for external and internal shocks and for the afterglow.

## 8.2. Synchrotron Emission from Relativistic Shocks

### 8.2.1. General Considerations

The most likely radiation process in GRBs is synchrotron emission [240, 18, 222, 103]. The observed low energy spectra provide an indication that this is indeed the case [95, 241].

The parameters that determine synchrotron emission are the magnetic field strength,  $B$ , and the electrons' energy distribution (characterized by the minimal Lorentz

factor  $\gamma_{e,min}$  and the index of the expected power-law electron energy distribution  $p$ ). These parameters should be determined from the microscopic physical processes that take place in the shocks. However, it is difficult to estimate them from first principles. Instead we define two dimensionless parameters,  $\epsilon_B$  and  $\epsilon_e$ , that incorporate our ignorance and uncertainties [222, 103].

The dimensionless parameter  $\epsilon_B$  measures the ratio of the magnetic field energy density to the total thermal energy  $e$ :

$$\epsilon_B \equiv \frac{U_B}{e} = \frac{B^2}{8\pi e}, \quad (48)$$

so that, after substituting the shock conditions we have:

$$B = \sqrt{32\pi c \epsilon_B^{1/2} \gamma_{sh} m_p^{1/2} n_1^{1/2}}. \quad (49)$$

There have been different attempts to estimate  $\epsilon_B$  [224, 240, 226]. We keep it as a free parameter. Additionally we assume that the magnetic field is randomly oriented in space.

The second parameter,  $\epsilon_e$ , measures the fraction of the total thermal energy  $e$  which goes into random motions of the electrons:

$$\epsilon_e \equiv \frac{U_e}{e}. \quad (50)$$

### 8.2.2. The Electron Distribution

We call consider a "typical" electron as one that has the average  $\gamma_e$  of the electrons distribution:

$$\langle \gamma_e \rangle = \frac{m_p}{m_e} \epsilon_e \gamma_{sh}. \quad (51)$$

Collisionless acceleration of electrons can be efficient if they are tightly coupled to the protons and the magnetic field by mean of plasma waves [243]. Since the electrons receive their random motions through shock-heating, we assume (following the treatment of non-relativistic shocks) that they develop a power law distribution of Lorentz factors:

$$N(\gamma_e) \sim \gamma_e^{-p} \quad \text{for } \gamma_e > \gamma_{e,min}. \quad (52)$$

We require  $p > 2$  so that the energy does not diverge at large  $\gamma_e$ . Since the shocks are relativistic we assume that all the electrons participate in the power-law, not just a small fraction in the tail of the distribution as in the Newtonian case. An indication that this assumption is correct is given by the lower energy spectrum observed in some GRBs [95, 241]. The minimum Lorentz factor,  $\gamma_{e,min}$ , of the distribution is related to  $\epsilon_e$  and to the total energy  $e \sim \gamma_{sh} n m_p c^2$ :

$$\gamma_{e,min} = \frac{m_p}{m_e} \frac{p-2}{p-1} \epsilon_e \gamma_{sh} = \frac{p-2}{p-1} \langle \gamma_e \rangle. \quad (53)$$

where  $\gamma_{sh}$  is the relative Lorentz factor across the corresponding shock.

The energy index  $p$  can be fixed by requiring that the model should be able to explain the high energy spectra of GRBs. If we assume that most of the radiation observed in the soft gamma-rays is due to synchrotron cooling, then it is straightforward to relate  $p$  to the power-law index of the observed spectra of GRBs,  $\beta$ . The mean spectral index of GRBs at high photon energies  $\beta \approx -2.25$ , [84] corresponds

Shock type			$\gamma_E$	$\gamma_{sh}$	
External	Newtonian	Forward	$\gamma$	$\gamma$	
		Reverse	$\gamma$	1	
	Relativistic	Forward	$\gamma\xi^{3/4}$	$\gamma\xi^{3/4}$	
		Reverse	$\gamma\xi^{3/4}$	$\xi^{-3/4}$	
Internal			$\gamma$	$\sqrt{\gamma_{int}/2} \sim \text{a few}$	
Afterglow			$\gamma(t)$	$\gamma(t)$	

Table 5: *Lorentz Factors*

to  $p \approx 2.5$ . This agrees, as we see later (9.3.2) with the value inferred from afterglow observations ( $p \sim 2.25$ ). We assume this value of  $p$  in what follows. The corresponding ratio that appears in Eq. 53  $(p-2)/(p-1)$  equals  $1/3$  and we have  $\gamma_{e,min} = 610\gamma_{sh}$ .

The shock acceleration mechanisms cannot accelerate the electrons to arbitrary high energy. For the maximal electron's energy, with a corresponding  $\gamma_{e,max}$ , the acceleration time equals to the cooling time. The acceleration time is determined by the Larmor radius  $R_L$  and the Alfvén velocity  $v_A$  [244]:

$$t_{acc} = \frac{cR_L}{v_A^2}. \quad (54)$$

This time scale should be compared with the synchrotron cooling time  $\gamma_e m_e c^2 / P_{syn}$  (in the local frame). Using  $v_A^2 \approx \epsilon_B^2$ , Eq. 49 to estimate  $B$  and Eq. 57 below to estimate  $P_{syn}$  one finds:

$$\gamma_{e,max} = \sqrt{\frac{24\pi\epsilon_B^2 e}{B\sigma_T\gamma_{sh}}} = 3.7 \times 10^8 \frac{\epsilon_B^{3/2}}{\gamma_{sh} n_1^{1/2}}. \quad (55)$$

cooling This value is quite large and generally it does not effect the observed spectrum in the soft gamma ray range.

### 8.2.3. Synchrotron Frequency and Synchrotron Power

The typical energy of synchrotron photons as well as the synchrotron cooling time depend on the Lorentz factor  $\gamma_e$  of the relativistic electron under consideration and on the strength of the magnetic field (see e.g. [245]). Since the emitting material moves with a Lorentz factor  $\gamma_E$  the photons are blue shifted. The characteristic photon energy in the observer frame is given by:

$$(h\nu_{syn})_{obs} = \frac{\hbar q_e B}{m_e c} \gamma_e^2 \gamma_E. \quad (56)$$

The power emitted by a single electron due to synchrotron radiation in the local frame is:

$$P_{syn} = \frac{4}{3} \sigma_T c U_B \gamma_e^2, \quad (57)$$

where  $\sigma_T$  is the Thomson cross section. The cooling time of the electron in the fluid frame is then  $\gamma_e m_e c^2 / P$ . The observed cooling time  $t_{syn}$  is shorter by a factor of  $\gamma_E$ :

$$t_{syn}(\gamma_e) = \frac{3m_e c}{4\sigma_T U_B \gamma_e \gamma_E}. \quad (58)$$

Substituting the value of  $\gamma_e$  from equation 56 into the cooling rate Eq. 58 we obtain the cooling time scale as a function of the observed photon energy:

$$t_{syn}(\nu) = \frac{3}{\sigma_T} \sqrt{\frac{2\pi\hbar m_e q_e}{B^3 \gamma_E \nu}} \quad (59)$$

Since  $\gamma_e$  does not appear explicitly in this equation  $t_{syn}$  at a given observed frequency is independent of the electrons' energy distribution within the shock. This is provided, of course, that there are electrons with the required  $\gamma_e$  so that there will be emission in the frequency considered. As long as there is such an electron the cooling time is "universal". This equation shows a characteristic scaling of  $t_{syn}(\nu) \propto \nu^{-1/2}$ . This is not very different from the observed relation  $\delta T \propto \nu^{-0.4}$  [102]. However, it is not clear if the cooling time and not another time scale determined the temporal profile.

The cooling time calculated above sets a lower limit to the variability time scale of a GRB since the burst cannot possibly contain spikes that are shorter than its cooling time. Observations of GRBs typically show asymmetric spikes in the intensity variation, where a peak generally has a fast rise and a slower exponential decline (FRED). A plausible explanation of this observation is that the shock heating of the electrons happens rapidly (though episodically), and that the rise time of a spike is related to the heating time. The decay time is then set by the cooling, so that the widths of spikes directly measure the cooling time.

### 8.2.4. The Integrated Synchrotron Spectrum

The instantaneous synchrotron spectrum of a single electron with an initial energy  $\gamma_e m_e c^2$  is a power law with  $F_\nu \propto \nu^{1/3}$  up to  $\nu_{syn}(\gamma_e)$  and an exponential decay above it. If the electron is energetic it will cool rapidly until it will reach  $\gamma_{e,c}$ . This is the Lorentz factor of an electron that cools on a hydrodynamic time scale. For a rapidly cooling electron we have to consider the time integrated spectrum above  $\hbar_{syn}(\gamma_{e,c})$ :  $F_\nu \propto \nu^{-1/2}$  from  $\nu_{syn}(\gamma_{e,c})$  up to  $\nu_{syn}(\gamma_e)$ .

To calculate the overall spectrum due to all the electrons we need to integrate over  $\gamma_e$ . Our discussion here follows [246]. We consider a power-law electron distribution with a power index  $p$  and a minimal Lorentz factor  $\gamma_{e,min}$  (see Eq. 52). Overall we expect a broken power law spectrum with a break frequency around the synchrotron frequency of the lowest energy electrons  $\nu_{syn}(\gamma_{e,min})$ . These power law indices depend on the cooling rate. The most energetic

electrons will always be cooling rapidly (independently of the behavior of the “typical electron”). Thus the highest spectrum is always satisfy:

$$F_\nu = N[(\gamma(\nu)]m_e c^2(\gamma(\nu)d\gamma/d\nu \propto \nu^{-p/2}. \quad (60)$$

similarly the low energy electrons will always be slow cooling and thus the lowest part of the spectrum will behave like  $F_\nu \propto \nu^{1/3}$ .

For slow cooling we have the instantaneous spectrum:  $F_\nu \propto \nu^{1/3}$  for the lower part of the spectrum. For the upper part we have

$$F_\nu = N[(\gamma(\nu)]P[(\gamma(\nu)]d\gamma/d\nu \propto \nu^{-(p-1)/2}, \quad (61)$$

where  $\gamma(\nu)$  is the Lorentz factor for which the synchrotron frequency equals  $\nu$ . The most energetic electrons will cool rapidly even when the overall system is in slow cooling. These electrons emit practically all their energy  $m_e c^2 \gamma$ , at their synchrotron frequency. Thus the uppermost part of the spectrum will satisfy:

For fast cooling we have  $F_\nu \propto \nu^{-1/2}$  for the lower part and  $F_\nu \propto \nu^{-p/2}$  for the upper part. Here at the lower end the least energetic electrons will be cooling slowly even when the typical electron is cooling rapidly. Thus we will have  $f_\nu \propto \nu^{1/3}$  in the lowest part of the spectrum.

The critical parameter that determines if the electrons are cooling fast or slow is  $\gamma_{e,c}$ , the Lorentz factor of an electron that cools on a hydrodynamic time scale. To estimate  $\gamma_{e,c}$  we compare  $t_{syn}$  (Eq. 58) with  $t_{hyd}$ , the hydrodynamic time scale (in the observer’s rest frame):

$$\gamma_{e,c} = \frac{3m_e c}{4\sigma_T U_B \gamma_E t_{hyd}} \quad (62)$$

*Fast cooling* occurs if  $\gamma_{e,c} < \gamma_{e,min}$ . All the electrons cool rapidly and the electrons’ distribution effectively extends down to  $\gamma_{e,c}$ . If  $\gamma_{e,c} > \gamma_{e,min}$  only the high energy tail of the distribution (those electrons above  $\gamma_{e,c}$ ) cool and the system is in the *slow cooling* regime.

For the GRB itself we must impose the condition of fast cooling: the relativistic shocks must emit their energy effectively - otherwise there will be a serious inefficiency problem. Additionally we won’t be able to explain the variability if the cooling time is too long. The electrons must cool rapidly and release all their energy. In this case  $\gamma_{e,min} > \gamma_{e,c}$  [103] and all the electrons cool down roughly to  $\gamma_{e,c}$ . The observed flux,  $F_\nu$ , is given by:

$$F_\nu \propto \begin{cases} (\nu/\nu_c)^{1/3} F_{\nu,max}, & \nu_c > \nu, \\ (\nu/\nu_c)^{-1/2} F_{\nu,max}, & \nu_m > \nu > \nu_c, \\ (\nu_m/\nu_c)^{-1/2} (\nu/\nu_m)^{-p/2} F_{\nu,max}, & \nu > \nu_m, \end{cases} \quad (63)$$

where  $\nu_m \equiv \nu_{syn}(\gamma_{e,min})$ ,  $\nu_c \equiv \nu_{syn}(\gamma_{e,c})$  and  $F_{\nu,max}$  is the observed peak flux.

It is most likely that during the latter stages of an external shock (that is within the afterglow phase - provided that it arises due to external shocks) there will be a transition from fast to slow cooling [21, 23, 47, 247, 25]. When  $\gamma_c > \gamma_{e,min}$ , only those electrons with  $\gamma_e > \gamma_c$  can cool. We call this slow cooling, because the electrons with  $\gamma_e \sim \gamma_{e,min}$ , which form the bulk of the population, do

not cool. Integration over the electron distribution gives in this case:

$$F_\nu \propto \begin{cases} (\nu/\nu_m)^{1/3} F_{\nu,max}, & \nu_m > \nu, \\ (\nu/\nu_m)^{-(p-1)/2} F_{\nu,max}, & \nu_c > \nu > \nu_m, \\ (\nu_c/\nu_m)^{-(p-1)/2} (\nu/\nu_c)^{-p/2} F_{\nu,max}, & \nu > \nu_c. \end{cases} \quad (64)$$

For fast cooling  $\nu_c < \nu_m$ . We find that the peak flux is at  $\nu_c$  while the peak energy emitted (which corresponds to the peak of  $\nu F_\nu$ ) is at  $\nu_m$ . For slow cooling the situation reverses  $\nu_m < \nu_c$ . The peak flux is at  $\nu_m$  while the peak energy emitted is at  $\nu_c$ .

Typical spectra corresponding to fast and slow cooling are shown in Fig. 22. The light curve depends on the hydrodynamic evolution, which in turn determines the time dependence of  $\nu_m$ ,  $\nu_c$  and  $F_{\nu,max}$ .

For fast cooling the power emitted is simply the power given to the electrons, that is  $\epsilon_e$  times the power generated by the shock:

$$P_{fast} = \epsilon_e \frac{dE}{dt}. \quad (65)$$

For slow cooling the emitted power is determined by the ability of the electrons to radiate their energy:

$$P_{slow} = N_e P_{syn}(\gamma_{e,min}) \quad (66)$$

where,  $N_e$  is the number of electrons in the emitting region and  $P_{syn}(\gamma_{e,min})$ , the synchrotron power of an electron with  $\gamma_{e,min}$ , is given by Eq. 57.

### 8.3. Synchrotron Self Absorption

An important effect that we have ignored so far is the possibility of self absorption. This is irrelevant during the GRB itself. One of the essential features of the GRB spectrum is that it is produced in an optically thin region. However, self absorption may appear at late time and typically in radio emission [18, 247, 25, 248, 249]. When it appears it will cause a steep cutoff of the low energy spectrum, either as the commonly known  $\nu^{5/2}$  or as  $\nu^2$ .

To estimate the self absorption frequency we need the optical depth along the line of sight. A simple approximation is:  $\alpha'_{\nu'} R_l / \gamma_l$  where  $\alpha'_{\nu'}$  is the absorption coefficient [245]:

$$\alpha'_{\nu'} = \frac{(p+2)}{8\pi m_e \nu'^2} \int_{\gamma_{min}}^{\infty} d\gamma_e P'_{\nu',e}(\gamma_e) \frac{N(\gamma_e)}{\gamma_e} . \quad (67)$$

The self absorption frequency  $\nu_a$  satisfies:  $\alpha'_{\nu'_0} R / \gamma = 1$ . It can be estimated only once we have a model for the hydrodynamics and how do  $R$  and  $\gamma$  change with time [248, 249].

The spectrum below the the self-absorption frequency depends on the electron distribution. One obtains the well known [245],  $\nu^{5/2}$  slope when the synchrotron frequency of the electron emitting the self absorbed radiation is inside the self absorption range. One obtains a slope of  $\nu^2/2$  if there is self absorption, but the radiation in that range is due to the low energy tail of electrons radiating effectively at higher energies. For this latter case, which is more appropriate for GRB afterglow we find that [18, 25]:

$$F_\nu \propto \nu^2 [k_B T_e / (\gamma m_p c^2)] R^2, \quad (68)$$

where  $R$  is the radius of the radiating shell and the factor  $k_B T_e / (\gamma m_p c^2)$  describes the degree of electron equipartition in the plasma shock-heated to an internal energy per particle  $\gamma m_p c^2$  and moving with Lorentz factor  $\gamma$ .

#### 8.4. Inverse Compton Emission

Inverse Compton (IC) scattering may modify our analysis in several ways. IC can influence the spectrum even if the system is optically thin (as it must be) to Compton scattering (see e.g. [245]). In view of the high energies involved we assume that only one IC scattering takes place. After this scattering the photon's energy is so high that in the electron's rest frame it is above the Klein-Nishina energy and in this case the decrease in the Compton cross section makes this scattering unlikely. The effect of IC depends on the Comptonization parameter  $Y = \gamma^2 \tau_e$ . For fast cooling one can show [103] that  $Y$  satisfies:

$$\begin{aligned} Y = \epsilon_e / \epsilon_B &\quad \text{if} \quad \epsilon_e \ll \epsilon_B \\ Y = \sqrt{\epsilon_e / \epsilon_B} &\quad \text{if} \quad \epsilon_e \gg \epsilon_B. \end{aligned} \quad (69)$$

IC is unimportant if  $Y < 1$  and in this case it can be ignored.

If  $Y > 1$ , which corresponds to  $\epsilon_e > \epsilon_B$  and to  $Y = \sqrt{\epsilon_e / \epsilon_B}$  then a large fraction of the low energy synchrotron radiation will be up scattered by IC and a large fraction of the energy will be emitted via the IC processes. If those IC up scattered photons will be in the observed energy band then the observed radiation will be IC and not synchrotron photons. Those IC photons might be too energetic, that is their energy may be beyond the observed energy range. In this case IC will not influence the observed spectra directly. However, as IC will take a significant fraction of the energy of the cooling electrons it will influence the observations in two ways: it will shorten the cooling time (the emitting electrons will be cooled by both synchrotron and IC process). Second, assuming that the observed  $\gamma$ -ray photons results from synchrotron emission, IC will influence the overall energy budget and reduce the efficiency of the production of the observed radiation. We turn now to each of this cases.

Consider, first, the situation in which  $Y > 1$  and the IC photons are in the observed range so that some of the observed radiation may be due to IC rather than synchrotron emission. This is an interesting possibility since one might expect that the IC process will ease the requirement of rather large magnetic fields that is imposed by the synchrotron process. We show here that, somewhat surprisingly, this cannot be the case.

An IC scattering boosts the energy of the photon by a factor  $\gamma_e^2$ . Typical IC photons will be observed at the energy:

$$(h\nu_{IC})_{obs} = \frac{\hbar q_e B}{m_e c} \gamma_e^4 \gamma_E = 12 \text{Mev} B_{1G} (\gamma_{E100}) \left[ \frac{\gamma_e}{(m_p/m_e)} \right]^4. \quad (70)$$

where  $B_{1G} = B/1\text{Gauss}$  and  $\gamma_{E100} \equiv \gamma_{E/100}$ . The Lorentz factor of electrons radiating synchrotron photons which are IC scattered on electrons with the same Lorentz factor and have energy  $h\nu$  in the observed range is the square root of the  $\gamma_e$  required to produce synchrotron radiation in the same frequency. The required value for  $\gamma_e$  is rather

low relative to what one may expect in an external shock (in which  $\gamma_{e,ext} \sim \epsilon_e (m_p/m_e) \gamma_{sh}$ ). In internal shocks we expect lower values ( $\gamma_{e,int} \sim \epsilon_e (m_p/m_e)$ ) but in this case the equipartition magnetic field is much stronger (of the order of few thousand Gauss, or higher). Thus IC might produce the observed photons in internal shocks if  $\epsilon_B$  is rather small (of order  $10^{-5}$ ).

These electrons are cooled both by synchrotron and by IC. The latter is more efficient and the cooling is enhanced by the Compton parameter  $Y$ . The cooling time scale is:

$$\begin{aligned} t_{IC} &= \frac{6\pi c^{3/4} \sqrt{\epsilon_B} \hbar^{1/4} m_e^{3/4} q_e^{1/4}}{B^{7/4} \sqrt{\epsilon_e} (h\nu)^{1/4} \gamma_E^{3/4} \sigma_T} = \\ &8 \cdot 10^4 \text{sec} \sqrt{\frac{\epsilon_B}{\epsilon_e}} B_{1G}^{-7/4} (\gamma_{E100})^{-3/4} (h\nu/100\text{keV})^{-1/4} \end{aligned} \quad (71)$$

As we see in the following discussion for external shocks,  $t_{IC}(100\text{keV})$ , the IC cooling time if the IC radiation is in the observed range (soft gamma-rays) is too long, while for internal shocks  $t_{IC}(100\text{keV})$  is marginal. However, even if IC does not produce the observed  $\gamma$ -ray photons it still influences the process if  $Y > 1$ . It will speed up the cooling of the emitting regions and shorten the cooling time,  $t_{syn}$  estimated earlier (Eq. 59) by a factor of  $Y$ . Additionally IC also reduces the efficiency by the same factor, and the efficiency becomes extremely low as described below.

#### 8.5. Radiative Efficiency

The efficiency of a burst depends on three factors: First only the electrons' energy is available. This yields a factor  $\epsilon_e$ . Second, if  $\epsilon_B < \epsilon_e$  there is an additional factor of  $\min[1, \sqrt{\epsilon_B/\epsilon_e}]$  if the IC radiation is not observed. Third, there is a specific Lorentz factor,  $\hat{\gamma}_e$ , of an electron which emits synchrotron (or IC) radiation in the 100keV energy band. Therefore, only the energy radiated by electrons with  $\gamma_e \geq \hat{\gamma}_e$  is observed as soft  $\gamma$ -rays. Assuming a power law electron distribution with an index  $p = 2.5$  (see [103]) this gives a factor of  $(\gamma_{e,min}/\hat{\gamma}_e)^{1/2}$  (which is valid of course provided that  $\gamma_{e,min} < \hat{\gamma}_e$ ). The total efficiency is the multiplication of those three factors and it is given by:

$$\epsilon = \epsilon_e \min[1, \sqrt{\epsilon_B/\epsilon_e}] (\gamma_{e,min}/\hat{\gamma}_e)^{1/2} \quad (72)$$

The efficiency depends first of all on the electrons' energy density and to a lesser extend on the magnetic energy density. Both should be close to equipartition in order that the efficiency will be large. Additionally, in order that there will be photons in the 100keV range  $\gamma_{e,min}$  should be smaller than  $\hat{\gamma}$ . However efficient production of soft  $\gamma$ -rays requires that  $\gamma_{e,min}$  will not be too small compared with  $\hat{\gamma}$ . This estimate is, of course, different if the observed  $\gamma$ -rays are produced by inverse Compton scattering.

#### 8.6. Internal Shocks

Internal shocks are the leading mechanism for energy conversion and production of the observed gamma-ray radiation. We discuss, in this section, the energy conversion process, the typical radiation frequency and its efficiency.

### 8.6.1. Parameters for Internal Shocks

Internal shocks take place when an inner shell overtakes a slower outer shell. Consider a fast inner shell with a Lorentz factor  $\gamma_r$  that collides with a slower shell whose Lorentz factor is  $\gamma_s$ . If  $\gamma_r \gtrsim \gamma_s \sim \gamma$  then the inner shell will overtake the outer one at:

$$R_\delta \approx \gamma^2 \delta \approx 10^{14} \text{ cm } \delta_{10} \gamma_{100}^2 \quad (73)$$

where  $\delta$  is the initial separation between the shells in the observer's rest frame and  $\delta_{10} = \delta/10^{10} \text{ cm}$  and  $\gamma_{100} = \gamma/100$ . Clearly internal shocks are relevant only if they appear before the external shock that is produced as the shell sweeps up the ISM. We show in section 8.7.1 that the necessary condition for internal shocks to occur before the external shock is:

$$\xi^{3/2} > \zeta. \quad (74)$$

where  $\xi$  and  $\zeta$  are two dimensionless parameters. The parameter,  $\xi$ , characterizes the interaction of the flow with the external medium and it is defined in Eq. 92 (see section 8.7.1). The second parameter,  $\zeta$ , characterizes the variability of the flow:

$$\zeta \equiv \frac{\delta}{\Delta} \leq 1. \quad (75)$$

We have seen in section 7.4 that for internal shocks the duration of the burst  $T \approx \Delta/c$  and the duration of individual spikes  $\delta T \approx \delta/c$ . The observed ratio  $\mathcal{N}$  defined in section 2.2 must equal  $1/\zeta$  and this sets  $\zeta \approx 0.01$ .

The overall duration of a burst produced by internal shocks equals  $\Delta/c$ . Thus, whereas external shocks require an extremely large value of  $\gamma$  to produce a very short burst, internal shocks can produce a short burst with a modest value of the Lorentz factor  $\gamma$ . This eases somewhat the baryon purity constraints on source models. The condition 74 can be turned into a condition that  $\gamma$  is sufficiently small:

$$\gamma \leq 2800 \zeta_{0.01}^{-1/2} T_{10}^{-3/8} l_{18}^{3/8}, \quad (76)$$

where we have used  $T = \Delta/c$  and we have defined  $T_{10} = T/10\text{s}$  and  $\zeta_{0.01} = \zeta/0.01$ . It follows that internal shocks take place in relatively "low"  $\gamma$  regime. Fig. 23 depicts the regimes in the physical parameter space  $(\Delta, \gamma)$  in which various shocks are possible. It also depicts an example of a  $T = \Delta/c = 1\text{s}$  line.

Too low a value of the Lorentz factor leads to a large optical depth in the internal shocks region. Using Eq. 27 for  $R_e$ , at which the optical depth for Compton scattering of the photons on the shell's electrons equals one, Eq. 73 for  $R_\delta$  and the condition  $R_e \leq R_\delta$  we find:

$$\gamma \geq \left( \frac{E \sigma_T}{4c^2 \delta^2 m_p \pi} \right)^{1/5} = 130 T_{10}^{-2/5} \zeta_{0.01}^{-2/5} E_{52}^{1/5}. \quad (77)$$

In addition, the radius of emission should be large enough so that the optical depth for  $\gamma\gamma \rightarrow e^+e^-$  will be less than unity ( $\tau_{\gamma\gamma} < 1$ ). There are several ways to consider this constraint. The strongest constraint is obtained if one demands that the optical depth of an observed high energy, e.g. 100MeV photon will be less than unity [210, 211]. Following these calculations and using Eq. 73 to express  $R_\delta$  we find:

$$\gamma > 570 (\zeta_{0.01} T_{10})^{-1/4}. \quad (78)$$

This constraint, which is due to the  $\gamma\gamma$  interaction, is generally more important than the constraint due to Compton scattering: that is  $\tau_{\gamma\gamma} > \tau_e$ .

Eq. 76, and the more restrictive Eq. 78 constrains  $\gamma$  to a relatively narrow range:

$$570 \zeta_{0.01}^{-1/4} T_{10}^{-1/4} \leq \gamma_E \leq 2800 \zeta_{0.01}^{-1/2} T_{10}^{-3/8} l_{18}^{3/8}. \quad (79)$$

This can be translated to a rather narrow range of emission radii:

$$10^{15} \text{ cm } \zeta_{0.01}^{1/2} T_{10}^{1/2} \leq R_\delta \leq 2.5 \cdot 10^{16} \text{ cm } T_{10}^{1/4} l_{18}^{3/4}. \quad (80)$$

In Fig. 24, we plot the allowed regions in the  $\gamma$  and  $\delta$  parameter space. Using the less restrictive  $\tau_e$  limit 77 we find:

$$5 \times 10^{13} \text{ cm } \zeta_{0.01}^{1/5} T_{10}^{1/5} E_{52}^{2/5} \leq R_\delta \leq 2.5 \cdot 10^{16} \text{ cm } T_{10}^{1/4} l_{18}^{3/4}$$

$$130 \zeta_{0.01}^{-2/5} T_{10}^{-2/5} E_{52}^{1/5} \leq \gamma_E \leq 2800 \zeta_{0.01}^{-1/2} T_{10}^{3/8}.$$

Three main conclusions emerge from the discussion so far. First, if the spectrum of the observed photons extends beyond 100MeV (as was the case in the bursts detected by EGRET [83]) and if those high energy photons are emitted in the same region as the low energy ones then the condition on the pair production,  $\tau_{\gamma\gamma}$ , Eq. 78 is stronger than the condition on Compton scattering Eq. 81. This increases the required Lorentz factors. Second, the Compton scattering limit (which is independent of the observed high energy tail of the spectrum) poses also a lower limit on  $\gamma$ . However, this is usually less restrictive than the  $\tau_{\gamma\gamma}$  limit. Finally, one sees in Fig. 24 that optically thin internal shocks are produced only in a narrow region in the  $(\delta, \gamma)$  plane. The region is quite small if the stronger pair production limit holds. In this case there is no single value of  $\gamma$  that can produce peaks over the whole range of observed durations. The allowed region is larger if we use the weaker limits on the opacity. But even with this limit there is no single value of  $\gamma$  that produces peaks with all durations. The IS scenario suggests that bursts with very narrow peaks should not have very high energy tails and that very short bursts may have a softer spectrum.

### 8.6.2. Physical Conditions and Emission from Internal Shocks

Provided that the different parts of the shell have comparable Lorentz factors differing by factor of  $\sim 2$ , the internal shocks are mildly relativistic. The protons' thermal Lorentz factor will be of order of unity, and the shocked regions will still move highly relativistically towards the observer with approximately the initial Lorentz factor  $\gamma$ . In front of the shocks the particle density of the shell is given by the total number of baryons  $E/\gamma m_p c^2$  divided by the co-moving volume of the shell at the radius  $R_\delta$  which is  $4\pi R_\delta^2 \Delta \gamma$ . The particle density behind the shock is higher by a factor of 7 which is the limiting compression possible by Newtonian shocks (assuming an adiabatic index of relativistic gas, i.e., 4/3). We estimate the pre-shock density of the particles in the shells as:  $[E/(\gamma m_p c^2)]/(4\pi(\delta\gamma)^2 \gamma \Delta)$ . We introduce  $\gamma_{int}$  as the Lorentz factor of the internal

shock. As this shock is relativistic (but not extremely relativistic)  $\gamma_{int}$  is of order of a few. Using Eq. 48 for the particle density  $n$  and the thermal energy density  $e$  behind the shocks we find:

$$n_{int} \approx \frac{4E(\gamma_{int}/2)^{1/2}}{4\pi\gamma^6 c^2 m_p \delta^2 \Delta} = \quad (81)$$

$$2 \times 10^{10} \text{ cm}^{-3} E_{52}(\gamma_{int}/2)^{1/2} \gamma_{100}^{-6} \Delta_{12}^{-1} \delta_{10}^{-2},$$

$$e_{int} = (\gamma_{int}/2)^{1/2} n_{int} m_p c^2. \quad (82)$$

We have defined here  $\Delta_{12} = \Delta/10^{12} \text{ cm}$ . Using Eq. 49 we find:

$$B_{int} = 6 \cdot 10^5 \text{ Gauss } \epsilon_B^{1/2} E_{52}^{1/2} \gamma_{100}^{-3} \Delta_{12}^{-1/2} \delta_{10}^{-1} (\gamma_{int}/2)^{1/2}. \quad (83)$$

Using Eqs. 49, 51, 56 and 81 we can estimate the typical synchrotron frequency from an internal shock. This is the synchrotron frequency of an electron with a “typical” Lorentz factor:

$$(h\nu_{syn})_{obs}|_{\langle\gamma_e\rangle} = \frac{\hbar q_e B}{m_e c} \gamma_e^2 \gamma = 220 \text{ keV } E_{52}^{1/2} \epsilon_B^{1/2} \times \zeta_{0.01} (\gamma_{int}/2)^{1/2} \gamma_{100}^{-2} \Delta_{12}^{-3/2} [\gamma_e/(m_p/m_e)]^2. \quad (84)$$

The corresponding observed synchrotron cooling time is:

$$t_{syn}|_{\langle\gamma_e\rangle} = 1.3 \cdot 10^{-6} \text{ sec } \epsilon_B^{-1} \delta_{10}^2 \Delta_{12} \gamma_{100}^5 E_{52}^{-1} (\gamma_{int}/2)^{-1}. \quad (85)$$

Using Eq. 53 we can express  $\gamma_{e,min}$  in terms of  $\gamma_{int}$  to estimate the minimal synchrotron frequency:

$$(h\nu_{syn})_{obs}|_{\gamma_{e,min}} = 24 \text{ keV } E_{52}^{1/2} \epsilon_B^{1/2} \epsilon_e \times \zeta_{0.01}^{-1} (\gamma_{int}/2)^{5/2} \gamma_{100}^{-2} \Delta_{12}^{-3/2}. \quad (86)$$

The energy emitted by a “typical electron” is around 220keV. The energy emitted by a “minimal energy” electron is about one order of magnitude lower than the typical observed energy of  $\sim 100$ keV. This should correspond to the break energy of the spectrum. This result seems in a good agreement with the observations. But this estimate might be misleading as both  $\epsilon_B$  and  $\epsilon_e$  might be significantly lower than unity. Still these values of  $(h\nu_{syn})_{obs}$  are remarkably close to the observations. One might hope that this might explain the observed lower cutoff of the GRB spectrum. Note that a lower value of  $\epsilon_B$  or  $\epsilon_e$  might be compensated by a higher value of  $\gamma_{int}$ . This is advantageous as shocks with higher  $\gamma_{int}$  are more efficient (see section 8.6.4).

The synchrotron cooling time at a given frequency (in the observer’s frame) is given by:

$$t_{syn}(h\nu) = 2 \times 10^{-6} \text{ sec } \epsilon_B^{-3/4} \left( \frac{h\nu_{obs}}{100 \text{ keV}} \right)^{-1/2} \times \delta_{10}^{3/2} \Delta_{12}^{3/4} \gamma_{100}^4 E_{52}^{3/4} (\gamma_{int}/2)^{-3/4}. \quad (87)$$

We recover the general trend  $t_{syn} \propto (h\nu)^{-1/2}$  of synchrotron emission. However if (as we expect quite generally) this cooling time is much shorter than  $T_{ang}$  it does not determine the width of the observed peaks. It will correspond to the observed time scales if, for example,  $\epsilon_B$  is small. But then the “typical” photon energy will be far below the observed range. Therefore, it is not clear this relation can explain the observed dependence of the width of the bursts on the observed energy.

### 8.6.3. Inverse Compton in Internal Shocks

The calculations of section 8.4 suggest that the typical Inverse Compton (IC) (actually synchrotron - self Compton) radiation from internal shocks will be at energy higher by a factor  $\gamma_e^2$  than the typical synchrotron frequency. Since synchrotron emission is in the keV range and  $\gamma_{e,min} \approx m_p/m_e$ , the expected IC emission should be in the GeV or even TeV range. This radiation might contribute to the prompt very high energy emission that accompanies some of the GRBs [83].

However, if the magnetic field is extremely low:  $\epsilon_B \sim 10^{-12}$  then we would expect the IC photons to be in the observed  $\sim 100$ keV region:

$$h\nu_{IC-int} = 800 \text{ keV } (\epsilon_B/10^{-12})^{1/2} \times \delta_{10}^{-1} \Delta_{12}^{-1/2} \gamma_{100}^{-2} [\gamma_e/(mp/me)]^4 E_{52}^{1/2} [\gamma_{int}/2]^{1/2}. \quad (88)$$

Using Eqs. 71 and 83 we find that the cooling time for synchrotron-self Compton in this case is:

$$\tau_{IC-int} = 1 \text{ sec } \epsilon_e^{-1/2} (\epsilon_B/10^{-12})^{-1/2} \times \delta_{10}^{-2} \Delta_{12} \gamma_{100}^5 [\gamma_e/(mp/me)]^{-1} E_{52}^{-1} (\gamma_{int}/2)^{-1}. \quad (89)$$

This is marginal. It is too large for some bursts and possibly adequate for others. It could possibly be adjusted by a proper choice of the parameters. It is more likely that if Inverse Compton is important then it contributes to the very high (GeV or even TeV) signal that accompanies the lower energy GRB (see also [250]).

### 8.6.4. Efficiency in Internal Shocks

The elementary unit in the internal shock model (see section 7.4) is a a binary (two shells) encounter between a rapid shell (denoted by the subscript  $r$ ) that catches up a slower one (denoted  $s$ ). The two shells merge to form a single shell (denoted  $m$ ). The system behaves like an inelastic collision between two masses  $m_r$  and  $m_s$ .

The efficiency of a single collision between two shells was calculated earlier in section 8.1.1. For multiple collisions the efficiency depends on the nature of the random distribution. It is highest if the energy is distributed equally among the different shells. This can be explained analytically. Consider a situation in which the mass of the shell,  $m_i$  is correlated with the (random) Lorentz factor,  $\gamma_i$  as  $m_i \propto \gamma_i^\eta$ . Let all the shells collide and merge and only then emit the thermal energy as radiation. Using conservation of energy and momentum we can calculate the overall efficiency:

$$\epsilon = 1 - \Sigma \gamma_i^\eta / \sqrt{\Sigma \gamma_i^{\eta-1} \Sigma \gamma_i^{\eta+1}}. \quad (90)$$

Averaging over the random variables  $\gamma_i$ , and assuming a large number of shells  $N \rightarrow \infty$  we obtain:

$$\langle \epsilon \rangle \sim 1 - \frac{(\gamma_{max}/\gamma_{min})^{\eta+1} - 1}{\eta + 1} \times \sqrt{\frac{\eta(\eta+2)}{[(\gamma_{max}/\gamma_{min})^\eta - 1][(\gamma_{max}/\gamma_{min})^{\eta+2} - 1]}}. \quad (91)$$

This formula explains qualitatively the numerical results: the efficiency is maximal when the energy is distributed equally among the different shells (which corresponds to  $\eta = -1$ ).

In a realistic situation we expect that the internal energy will be emitted after each collision, and not after all the shells have merged. In this case there is no simple analytical formula. However, numerical calculations show that the efficiency of this process is low (less than 2%) if the initial spread in  $\gamma$  is only a factor of two [32]. However the efficiency could be much higher [33]. The most efficient case is when the shells have a comparable energy but very different Lorentz factors. In this case ( $\eta = -1$ , and spread of Lorentz factor  $\gamma_{max}/\gamma_{min} > 10^3$ ) the efficiency is as high as 40%. For a moderate spread of Lorentz factor  $\gamma_{max}/\gamma_{min} = 10$ , with  $\eta = -1$ , the efficiency is 20%.

The efficiency discussed so far is the efficiency of conversion of kinetic energy to internal energy. One should multiply this by the radiative efficiency, discussed in 8.5 (Eq. 72) to obtain the overall efficiency of the process. The resulting values may be rather small and this indicates that some sort of beaming may be required in most GRB models in order not to come up with an unreasonable energy requirement.

#### 8.6.5. Summary - Internal Shocks

Internal shocks provide the best way to explain the observed temporal structure in GRBs. These shocks, that take place at distances of  $\sim 10^{15}$  cm from the center, convert two to twenty percent of the kinetic energy of the flow to thermal energy. Under reasonable conditions the typical synchrotron frequency of the relativistic electrons in the internal shocks is around 100 keV, more or less in the observed region.

Internal shocks require a variable flow. The situation in which an inner shell is faster than an outer shell is unstable [251]. The instability develops before the shocks form and it may affect the energy conversion process. The full implications of this instability are not understood yet.

Internal shocks can extract at most half of the shell's energy [32, 33, 69]. Highly relativistic flow with a kinetic energy and a Lorentz factor comparable to the original one remains after the internal shocks. Sari & Piran [20] pointed out that if the shell is surrounded by ISM and collisionless shock occurs the relativistic shell will dissipate by "external shocks" as well. This predicts an additional smooth burst, with a comparable or possibly greater energy. This is most probably the source of the observed "afterglow" seen in some counterparts to GRBs which we discuss later. This leads to the Internal-External scenario [252, 20, 26] in which the GRB itself is produced by an Internal shock, while the "afterglow" that was observed to follows some GRBs is produced by an external shock.

The main concern with the internal shock model is its low efficiency of conversion of kinetic energy to  $\gamma$ -rays. This could be of order twenty percent under favorable conditions and significantly lower otherwise. If we assume that the "inner engine" is powered by a gravitational binding energy of a compact object (see section 10.1) a low efficiency may require beaming to overcome an overall energy crisis.

#### 8.7. Shocks with the ISM - External shocks

We turn now to the interaction of a relativistic shell with the ISM. We have seen in section 7.4 that external shocks cannot produce bursts with a complicated temporal structure. Still it is worthwhile to explore this situation. First, there are some smooth bursts that might be produced in this way. Second, one needs to understand the evolution of external shocks in order to see why they cannot satisfy the condition  $R_E/\gamma^2 \leq \Delta$ . Third, it is possible that in some bursts emission is observed from both internal and external shocks [253]. Finally, as we see in the following section 9 the observed afterglow is most likely produced by external shocks.

##### 8.7.1. Newtonian vs. Relativistic Reverse Shocks

The interaction between a relativistic flow and an external medium depends, like in SNRs, on the Sedov length,  $l \equiv (E/n_{ism}m_p c^2)^{1/3}$ . The ISM rest mass energy within a volume  $l^3$  equals the energy of the GRB:  $E$ . For a canonical cosmological burst with  $E \approx 10^{52}$  ergs and a typical ISM density  $n_{ism} = 1$  particle/cm<sup>3</sup> we have  $l \approx 10^{18}$  cm. A second length scale that appears in the problem is  $\Delta$ , the width of the relativistic shell in the observer's rest frame.

There are two possible types of external shocks [233]. They are characterized according to the nature of the reverse shock: Newtonian Reverse Shock (NRS) vs. Relativistic Reverse Shock (RRS). If the reverse shock is relativistic (RRS) then it reduces significantly the kinetic energy of each layer that it crosses. Each layer within the shell loses its energy independently from the rest of the shock. The energy conversion process is over once the reverse shock crosses the shell (see Fig. 13). A Newtonian or even mildly relativistic reverse shock (NRS) is comparatively weak. Such a shock reduces the energy of the layer that it crosses by a relatively small amount. Significant energy conversion takes place only after the shock has crossed the shell several time after it has been reflected as a rarefaction wave from the inner edge (see Fig. 12). The shell behaves practically like a single object and it loses its energy only by the time that it accumulates an external mass equal to  $M/\gamma$ .

The question which scenario is taking place depends on the parameters of the shell relative to the parameters of the ISM. As we see shortly it depends on a single dimensionless parameter  $\xi$  constructed from  $l$ ,  $\Delta$  and  $\gamma$ : [233]:

$$\xi \equiv (l/\Delta)^{1/2} \gamma^{-4/3}. \quad (92)$$

As the shell propagates outwards it is initially very dense and the density ratio between the shell and the ISM,  $f \equiv n_4/n_1$ , is extremely large (more specifically  $f > \gamma^2$ ). The reverse shock is initially Newtonian (see Eq. 43). Such a shock converts only a small fraction of the kinetic energy to thermal energy. As the shell propagates the density ratio,  $f$ , decreases (like  $R^{-2}$  if the width of the shell is constant and like  $R^{-3}$  if the shell is spreading). Eventually the reverse shock becomes relativistic at  $R_N$  where  $f = \gamma^2$ . The question where is the kinetic energy converted depends on whether the reverse shock reaches the inner edge of the shell before or after it becomes relativistic.

There are four different radii that should be considered. The following estimates assume a spherically symmetric shell, or that  $E$  and  $M$  are energy and rest mass divided by the fraction of a sphere into which they are launched. The reverse shock becomes relativistic at  $R_N$ , where  $f = n_4/n_1 = 1$ :

$$R_N = l^{3/2}/\Delta^{1/2}\gamma^2 \quad (93)$$

Using the expression for the velocity of the reverse shock into the shell (Eq. 46) we find that the reverse shock reaches the inner edge of the shell at  $R_\Delta$  [233]:

$$R_\Delta = l^{3/4}\Delta^{1/4}. \quad (94)$$

A third radius is  $R_\gamma$ , where the shell collects an ISM mass of  $M/\gamma$  [27, 18]. For NRS this is where an effective energy release occurs:

$$R_\gamma = \frac{l}{\gamma^{2/3}} = \left( \frac{E}{n_{ism}m_p c^2 \gamma^2} \right)^{1/3} = 5.4 \times 10^{16} \text{ cm } E_{52}^{1/3} n_1^{-1/3} \gamma_{100}^{-2/3}, \quad (95)$$

where we defined  $n_1 = n_{ism}/1$  particle/cm<sup>3</sup>. Finally we have  $R_\delta = \delta\gamma^2$ , (see Eq. 73). The different radii are related by the dimensionless parameter  $\xi$ , and this determines the character of the shock:

$$R_\delta/\xi = R_\Delta/\xi^{3/2} = R_\gamma\xi^2 = R_N/\xi^3 \quad (96)$$

If  $\xi > 1$  then:

$$R_\delta < R_\Delta < R_\gamma < R_N. \quad (97)$$

The reverse shock remains Newtonian or at best mildly relativistic during the whole energy extraction process. The reverse shock reaches the inner edge of the shock at  $R_\Delta$  while it is still Newtonian. At this stage a reflected rarefaction wave begins to move forwards. This wave is, in turn, reflected from the contact discontinuity, between the shell's material and the ISM material, and another reverse shock begins. The overall outcome of these waves is that in this case the shell acts as a single fluid element of mass  $M \approx E/\gamma c^2$  that is interacting collectively with the ISM. It follows from Eq. 39 that an external mass  $m = M/\gamma$  is required to reduce  $\gamma$  to  $\gamma/2$  and to convert half of the kinetic energy to thermal energy. Energy conversion takes place at  $R_\gamma$ . Comparison of  $R_\gamma$  with  $R_e$  (equation 27) shows that the optical depth is much smaller than unity.

If the shell propagates with a constant width then  $R_N/\xi = R_\gamma = \sqrt{\xi}R_\Delta$  (see Fig. 25) and for  $\xi > 1$  the reverse shock remains Newtonian during the energy extraction period. If there are significant variations in the particles velocity within the shell it will spread during the expansion. If the typical variation in  $\gamma$  is of the same order as  $\gamma$  then the shell width increases like  $R/\gamma^2$ . Thus  $\Delta$  changes with time in such a manner that at each moment the current width,  $\Delta(t)$ , satisfies  $\Delta(t) \sim \max[\Delta(0), R/\gamma^2]$ . This delays the time that the reverse shock reaches the inner edge of the shell and increases  $R_\Delta$ . It also reduces the shell's density which, in turn, reduces  $f$  and leads to a decrease in  $R_N$ . The overall result is a triple coincidence  $R_N \approx R_\gamma \approx R_\Delta$  with a mildly relativistic reverse shock

and a significant energy conversion in the reverse shock as well. This means that due to spreading a shell which begins with a value of  $\xi > 1$  adjusts itself so as to satisfy  $\xi = 1$ .

For  $\xi \geq 1$  we find that  $T_{radial} \sim T_{ang} \sim R_\gamma/\gamma^2 > \Delta$ . Therefore, NRS can produce only smooth bursts. The bursts' duration is determined by the slowing down time of the shell. In section 7 we have shown that only one time scale is possible in this case. Given the typical radius of energy conversion,  $R_\gamma$  this time scale is:

$$\delta T \approx T_{obs} \approx R_\gamma/(\gamma_E^2 c) \approx R_\gamma/(\gamma^2 c) \approx 170 \text{ sec } E_{52}^{1/3} n_1^{-1/3} \gamma_{100}^{-8/3}, \quad (98)$$

If  $\gamma$  or  $\Delta$  are larger than  $\xi < 1$ . In this case the order is reversed:

$$R_N < R_\gamma < R_\Delta. \quad (99)$$

The reverse shock becomes relativistic very early (see Fig. 25). Since  $\gamma_{sh} = \gamma_2 \ll \gamma$  the relativistic reverse shock converts very efficiently the kinetic energy of the shell to thermal energy. Each layer of the shell that is shocked loses effectively all its kinetic energy at once and the time scale of converting the shell's kinetic energy to thermal energy is the shell crossing time. The kinetic energy is consumed at  $R_\Delta$ , where the reverse shock reaches the inner edge of the shell. Using Eq. 94 for  $R_\Delta$  and Eq. 45 we find that at  $R_\Delta$

$$\gamma_E = \gamma_2 = (l/\Delta)^{3/8}. \quad (100)$$

Note that  $\gamma_E$  is independent of  $\gamma$ . The observed radial or angular time scales are:

$$T_{radial} \approx T_{ang} \approx R_\Delta/\gamma_E^2 \approx \Delta/c = 30 \text{ sec } \Delta_{12}. \quad (101)$$

Thus even for RRS we find that  $\delta T \sim T$  and there is only one time scale. This time scale depends only on  $\Delta$  and it is independent of  $\gamma$ ! Spreading does not affect this estimate since for  $\xi < 1$  spreading does not occur before the energy extraction.

In the following discussions we focus on the RRS case and we express all results in terms of the parameter  $\xi$ . By setting  $\xi < 1$  in the expressions we obtain results corresponding to RRS, and by choosing  $\xi = 1$  in the same expressions we obtain the spreading NRS limit. We shall not discuss the case of non-spreading NRS ( $\xi \gg 1$ ), since spreading will always bring these shells to the mildly relativistic limit ( $\xi \sim 1$ ). Therefore, in this way, the same formulae are valid for both the RRS and NRS limits.

If  $\xi > 1$  it follows from Eq. 97 that internal shocks will take place before external shocks. If  $\xi < 1$  then the condition for internal shocks  $R_\delta < R_\Delta$  becomes Eq. 74:  $\xi^{3/2} > \zeta$ . As we have seen earlier (see section 8.6.1) this sets an upper limit on  $\gamma$  for internal shocks.

### 8.7.2. Physical Conditions in External Shocks

The interaction between the outward moving shell and the ISM takes place in the form of two shocks: a forward shock that propagates into the ISM and a reverse shock that propagates into the relativistic shell. This results in four distinct regions: the ISM at rest (denoted by the subscript 1 when we consider properties in this region), the

shocked ISM material which has passed through the forward shock (subscript 2 or f), the shocked shell material which has passed through the reverse shock (3 or r), and the unshocked material in the shell (4). See Fig. 21. The nature of the emitted radiation and the efficiency of the cooling processes depend on the conditions in the shocked regions 2 and 3. Both regions have the same energy density  $e$ . The particle densities  $n_2$  and  $n_3$  are, however, different and hence the effective “temperatures,” i.e. the mean Lorentz factors of the random motions of the shocked protons and electrons, are different.

The bulk of the kinetic energy of the shell is converted to thermal energy via the two shocks at around the time the shell has expanded to the radius  $R_\Delta$ . At this radius, the conditions at the forward shock are as follows,

$$\gamma_2 = \gamma \xi^{3/4}, \quad n_2 = 4\gamma_2 n_1, \quad e_2 = 4\gamma_2^2 n_1 m_p c^2, \quad (102)$$

while at the reverse shock we have

$$\bar{\gamma}_3 = \xi^{-3/4}, \quad \gamma_3 = \gamma \xi^{3/4}, \quad n_3 = 4\xi^{9/4} \gamma^2 n_1, \quad e_3 = e_2. \quad (103)$$

Substitution of  $\gamma_{sh} = \gamma_2 = \gamma \xi^{3/4}$  in Eq. 49 yields:

$$B = \sqrt{32\pi c \epsilon_B^{1/2} \gamma \xi^{3/4} m_p^{1/2} n_1^{1/2}} = (40 \text{ G}) \epsilon_B^{1/2} \xi^{3/4} \gamma_{100} n_1^{1/2}. \quad (104)$$

If the magnetic field in region 2 behind the forward shock is obtained purely by shock compression of the ISM field, the field would be very weak, with  $\epsilon_B \ll 1$ . Such low fields are incompatible with observations of GRBs. We therefore consider the possibility that there may be some kind of a turbulent instability which may bring the magnetic field to approximate equipartition. In the case of the reverse shock, magnetic fields of considerable strength might be present in the pre-shock shell material if the original exploding fireball was magnetic. The exact nature of magnetic field evolution during fireball expansion depends on several assumptions. Thompson [224] found that the magnetic field will remain in equipartition if it started off originally in equipartition. Mészáros, Laguna & Rees [240] on the other hand estimated that if the magnetic field was initially in equipartition then it would be below equipartition by a factor of  $10^{-5}$  by the time the shell expands to  $R_\Delta$ . It is uncertain which, if either, is right. As in the forward shock, an instability could boost the field back to equipartition. Thus, while both shocks may have  $\epsilon_B \ll 1$  with pure flux freezing, both could achieve  $\epsilon_B \rightarrow 1$  in the presence of instabilities. In principle,  $\epsilon_B$  could be different for the two shocks, but we limit ourselves to the same  $\epsilon_B$  in both shocks.

In both regions 2 and 3 the electrons have a power law distribution with a minimal Lorentz factor  $\gamma_{e,min}$  given by Eq. 53 with the corresponding Lorentz factors for the forward and the reverse shock.

### 8.7.3. Synchrotron Cooling in External Shocks

The typical energy of synchrotron photons as well as the synchrotron cooling time depend on the Lorentz factor  $\gamma_e$  of the relativistic electrons under consideration and on the strength of the magnetic field. Using Eq. 53 for  $\gamma_{e,min}$  we find the characteristic synchrotron energy for the forward shock:

$$(h\nu_{syn})_{obs}|_{\gamma_{e,min}} = 160 \text{ keV } \epsilon_B^{1/2} \epsilon_e^2 (\gamma_2/100)^4 n_1^{1/2}, \quad (105)$$

and

$$t_{syn}|_{\gamma_{e,min}} = 0.085 \text{ sec } \epsilon_B^{-1} \epsilon_e^{-1} (\gamma_2/100)^{-4} n_1^{-1}. \quad (106)$$

The characteristic frequency and the corresponding cooling time for the “typical” electron are larger by a factor of  $[(p-2)/(p-1)]^2$  and shorter by a factor of  $[(p-2)/(p-1)]^2$ , correspondingly.

These photons seems to be right in the observed soft gamma-ray range. However, one should recall that the frequency calculated in Eq. 105 depends on the forth power of  $\gamma_2$ . An increase of the canonical  $\gamma_2$  by a factor of 3 (that is  $\gamma_2 = 300$  instead of  $\gamma_2 = 100$ ) will yield a “typical” synchrotron emission at the 16MeV instead of 160keV. The Lorentz factor of a “typical electron” in the reverse shock is lower by a factor  $\xi^{3/2}$ . Therefore the observed energy is lower by a factor  $\xi^3$  while the cooling time scale is longer by a factor  $\xi^{-3/4}$ .

Alternatively we can check the conditions in order that there are electrons with a Lorentz factor  $\hat{\gamma}_e$  that be emitting soft gamma-rays with energies  $\sim 100\text{keV}$ . Using Eq. 56 we calculate  $\hat{\gamma}_e$ :

$$\hat{\gamma}_e = \left( \frac{m_e c h \nu_{obs}}{\hbar q_e \gamma_2 B} \right)^{1/2} = 5 \times 10^4 \epsilon_B^{-1/4} \times \left( \frac{h \nu_{obs}}{100 \text{ keV}} \right)^{1/2} \gamma_{100}^{-1} \xi^{3/4} n_1^{-1/4}. \quad (107)$$

Electrons with  $\gamma_e = \hat{\gamma}_e$  are available in the shocked material if  $\gamma_{e,min} < \hat{\gamma}_e$ . This corresponds to the condition

$$\epsilon_e|_r < 80 \epsilon_b^{-1/4} \left( \frac{h \nu_{obs}}{100 \text{ keV}} \right)^{1/2} \gamma_{100}^{-1} n_1^{-1/4} \quad (108)$$

in the reverse shock, and the condition

$$\epsilon_e|_f < 0.8 \epsilon_B^{-1/4} \left( \frac{h \nu_{obs}}{100 \text{ keV}} \right)^{1/2} \gamma_{100}^{-2} \xi^{-3/2} n_1^{-1/4} \quad (109)$$

in the forward shock. Since by definition  $\epsilon_e \leq 1$ , we see that the reverse shock always has electrons with the right Lorentz factors to produce soft gamma-ray synchrotron photons. However, the situation is marginal in the case of the forward shock. If  $\gamma > 100$  and if the heating of the electrons is efficient, i.e. if  $\epsilon_e|_f \sim 1$ , then most of the electrons may be too energetic. Of course, as an electron cools, it radiates at progressively softer energies. Therefore, even if  $\gamma_{min}$  is initially too large for the synchrotron radiation to be in soft gamma-rays, the same electrons would at a later time have  $\gamma_e \sim \hat{\gamma}_e$  and become visible. However, the energy remaining in the electrons at the later time will also be lower (by a factor  $\hat{\gamma}/\gamma_{min}$ ), which means that the burst will be inefficient. For simplicity, we ignore this radiation.

Substituting the value of  $\hat{\gamma}_e$  from equation 107 into the cooling rate Eq. 58 we obtain the cooling time scale as a function of the observed photon energy to be

$$t_{syn}(h\nu) = 1.4 \times 10^{-2} \text{ sec } \epsilon_B^{-3/4} \left( \frac{h \nu_{obs}}{100 \text{ keV}} \right)^{-1/2} \gamma_{100}^{-2} n_1^{-3/4}. \quad (110)$$

Eq. 110 is valid for both the forward and reverse shock, and is moreover independent of whether the reverse shock is relativistic or Newtonian.

The cooling time calculated above sets a lower limit to the variability time scale of a GRB since the burst cannot possibly contain spikes that are shorter than its cooling time. However, it is unlikely that this cooling time actually determines the observed time scales.

### 8.8. The Internal - External Scenario

Internal shocks can convert only a fraction of the total energy to radiation [32, 33, 69]. After the flow has produced a GRB via internal shocks it will interact via an external shock with the surrounding medium [20]. This will produce the afterglow - a signal that will follow the GRB. The idea of an afterglow in other wavelengths was suggested earlier [17, 18, 21] but it was suggested as a follow up of the, then standard, external shock scenario. In this case the afterglow would have been a direct continuation of the GRB activity and its properties would have scaled directly to the properties of the GRB.

According to internal-external models (internal shocks for the GRB and external shocks for the afterglow) different mechanisms produce the GRB and the afterglow. Therefore the afterglow should not be scaled directly to the properties of the GRB. This was in fact seen in the recent afterglow observations [25, 26]. In all models of external shocks the observed time satisfy  $t \propto R/\gamma_e^2$  and the typical frequency satisfies  $\nu \propto \gamma_e^4$ . Since most of the emission takes place at practically the same radius and all that we see is the variation of the Lorentz factor we expect quite generally [25]:  $\nu \propto t^{2\pm\iota}$ . The small parameter  $\iota$  reflects the variation of the radius and it depends on the specific assumptions made in the model. We would expect that  $t_x/t_\gamma \sim 5$  and  $t_{opt}/t_\gamma \sim 300$ . The observations of GRB970508 show that  $(t_{opt}/t_\gamma)_{observed} \approx 10^4$ . This is in a clear disagreement with the single external shock model for both the GRB and the afterglow.

Under quite general conditions the initial typical synchrotron energy for either the forward or the reverse external shock may fall in the soft GRB band. In this case the initial stage of the afterglow might overlap the  $\gamma$ -ray emission from the internal shock [253]. The result will be superposition of a rapidly varying signal on top of a long smooth and softening pulse. This possibility should be explored in greater detail.

## 9. AFTERGLOW

It is generally believed that the observed afterglow results from slowing down of a relativistic shell on the external ISM. The afterglow is produced, in this case, by an external shock. A second alternative is of “continuous emission”. The “inner engine” that powers the GRB continues to emit energy for much longer duration with a lower amplitude [36] and may produce the earlier part (first day or two in GRB970228 and GRB970508) of the afterglow. It is most likely that both processes take place to some extent [26]. We discuss in this section theoretical models for the production of the afterglow focusing on the external shock model.

### 9.1. Hydrodynamics of a Slowing Down Relativistic Shell

Within the external shock model there are several possible physical assumptions that one can make. The “standard” model assumes adiabatic hydrodynamics (energy losses are negligible and do not influence the hydrodynamics), slow cooling (the electrons radiate a small fraction of the energy that is generated by the shock) and synchrotron emission [17, 18, 21, 22, 23, 247, 47]. However there are other possibilities. First, the electrons’ energy might be radiated rapidly. In this case the radiation process is fast and the observed flux is determined by the rate of energy generation by the shock. If the electrons carry a significant fraction of the total internal energy fast cooling will influence the hydrodynamics which will not be adiabatic any more. In this case we have a radiative solution [25, 24] which differs in its basic scaling laws from the adiabatic one. The different possibilities are summarized in Table 9.1

#### 9.1.1. A Simple Collisional Model

We consider first a simple model for the slowing down of the shell. In this model the slowing down is described by a series of infinitesimal inelastic collisions between the shell and infinitesimal external masses. We assume a homogeneous shell described by its rest frame energy  $M$  (rest mass and thermal energy) and its Lorentz factor  $\gamma$ . Initially,  $E_0 = M_0 c^2 \gamma_0$ . The shell collides with the surrounding matter. We denote the mass of the ISM that has already collided with the shell by  $m(R)$ . As the shell propagates it sweeps up more ISM mass. Additional ISM mass elements,  $dm$ , which are at rest collides inelastically with the shell.

Energy and momentum conservation yield:

$$\frac{d\gamma}{\gamma^2 - 1} = -\frac{dm}{M}, \quad (111)$$

and

$$dE = (\gamma - 1)dm, \quad (112)$$

where  $dE$  is the thermal energy produced in this collision. We define  $\epsilon$  as the fraction of the shock generated thermal energy (relative to the observer frame) that is radiated. The incremental total mass satisfies:

$$dM = (1 - \epsilon)dE + dm = [(1 - \epsilon)\gamma + \epsilon]dm. \quad (113)$$

These equations yields analytic relations between the Lorentz factor and the total mass of the shell:

$$\frac{(\gamma - 1)(\gamma + 1)^{1-2\epsilon}}{(\gamma_0 - 1)(\gamma_0 + 1)^{1-2\epsilon}} = (M/M_0)^{-2}, \quad (114)$$

and between  $m(R)$  (and therefore  $R$ ) and  $\gamma$ .

$$\frac{m(R)}{M_0} = -(\gamma_0 - 1)^{1/2}(\gamma_0 + 1)^{1/2-\epsilon} \times \int_{\gamma_0}^{\gamma} (\gamma' - 1)^{-3/2}(\gamma' + 1)^{-3/2+\epsilon} d\gamma'. \quad (115)$$

These relations completely describe the hydrodynamical evolution of the shell.

	Adiabatic Hydrodynamics	Radiative Hydrodynamics
Slow Cooling	Arbitrary $\epsilon_e$	Impossible
Fast Cooling	$\epsilon_e < 1$	$\epsilon_e \approx 1$

Table 6: *Afterglow Models*

Two basic features can be seen directly from Eq. 116. First, we can estimate the ISM mass  $m$  that should be swept to get significant deceleration. Solving Eq. 116 with an upper limit  $\gamma_0/2$  and using  $\gamma_0 \gg 1$  we obtain the well known result: a mass  $m \cong M_0/(2\gamma_0)$  is required to reach  $\gamma = \gamma_0/2$ . Apparently this result is independent of the cooling parameter  $\epsilon$ .

A second simple result can be obtained in the limit that  $\gamma_0 \gg \gamma \gg 1$ :

$$m(R) = \frac{M_0}{(2-\epsilon)\gamma_0} \left( \frac{\gamma}{\gamma_0} \right)^{-2+\epsilon}, \quad (116)$$

so that  $\gamma \propto R^{-3/(2-\epsilon)}$ . For  $\epsilon = 0$  this yields the well known adiabatic result:

$$\frac{4\pi}{3} R^3 n m_p c^2 \gamma^2 = E_0, \quad (117)$$

and  $\gamma \propto R^{-3/2}$  [238, 18, 22, 23, 247]. For  $\epsilon = 1$  this yields the completely radiative result:

$$\frac{4\pi}{3} R^3 n m_p c^2 \gamma \gamma_0 = E_0, \quad (118)$$

and  $\gamma \propto R^{-3}$  [238, 24, 25].

For comparison with observations we have to calculate the observed time that corresponds to different radii and Lorentz factors. The well known formula

$$t_{obs} = \frac{R}{2\gamma^2 c} \quad (119)$$

is valid only for emission along the line of sight from a shell that propagates with a constant velocity. Sari [253] pointed out that as the shell decelerates this formula should be used only in a differential sense:

$$dt_{obs} = \frac{dR}{2\gamma^2 c}. \quad (120)$$

Eq. 120 should be combined with the relation 117 or 118 and integrated to get the actual relation between observed time and emission radius. For an adiabatic expansion, for example, this yields:  $t_{obs} = R/16\gamma^2 c$  [253]. Eq. 120 is valid only along the line of sight. The situation is complicated further if we recall that the emission reaches the observer from an angle of order  $\gamma^{-1}$  around the line of sight. Averaging on all angles yields another numerical factor [254, 255, 256] and altogether we get

$$t_{obs} \approx \frac{R}{c_\gamma \gamma_2 c}, \quad (121)$$

where the value of the numerical factor,  $c_\gamma$ , depends on the details of the solution and it varies between  $\sim 3$  and

$\sim 7$ . Using Eqs. 121 and 117 or 118 we obtain the following relations between  $R$ ,  $\gamma$  and  $t$ :

$$R(t) \cong \begin{cases} (3Et/\pi m_p nc)^{1/4}, & \text{ad,} \\ (4ct/L)^{1/7} L, & \text{rad,} \end{cases} \quad (122)$$

$$\gamma(t) \cong \begin{cases} (3E/256\pi nm_p c^5 t^3)^{1/8}, & \text{ad,} \\ (4ct/L)^{-3/7}, & \text{rad,} \end{cases} \quad (123)$$

where  $L \equiv (3E/4\pi nm_p c^2 \gamma)^{1/3}$  is the radius where the external mass equals the mass of the shell.

One can proceed and use the relation between  $R$  and  $\gamma$  and  $t_{obs}$  (Eqs. 122 and 123) to estimate the physical conditions at the shocked material using Eqs. 44. Then one can estimate the emitted radiation from this shock using Eqs. 56 and 57. However, before doing so we explore the Blandford-McKee self similar solution [238], which describes more precisely the adiabatic expansion. This solution is inhomogeneous with a well determined radial profile. The matter at the front of the shell moves faster than the average speed. This influences the estimates of the radiation emitted from the shell.

### 9.1.2. The Blandford-McKee Self-Similar Solution

Blandford & McKee [238] discovered a self-similar solution that describes the adiabatic slowing down of an extremely relativistic shell propagating into the ISM. Using several simplifications and some algebraic manipulations we rewrite the Blandford-McKee solution as [253]:

$$\begin{aligned} n(r, t) &= 4n\gamma(t) [1 + 16\gamma(t)^2(1 - r/R)]^{-5/4}, \\ \gamma(r, t) &= \gamma(t) [1 + 16\gamma(t)^2(1 - r/R)]^{-1/2}, \\ e(r, t) &= 4nm_p c^2 \gamma(t)^2 [1 + 16\gamma(t)^2(1 - r/R)]^{-17/12} \end{aligned} \quad (124)$$

where  $n(r, t)$ ,  $e(r, t)$  and  $\gamma(r, t)$  are, respectively, the density, energy density and Lorentz factor of the material behind the shock (not to be confused with the ISM density  $n$ ) and  $\gamma(t) = \gamma(R(t))$  is the Lorentz factor of material just behind the shock.  $n(r, t)$  and  $e(r, t)$  are measured in the fluid's rest frame while  $\gamma(r, t)$  is relative to an observer at rest. The total energy in this adiabatic flow equals  $E = E_0$ , the initial energy. The scaling laws of  $R(t)$  and  $\gamma(t)$  that follow from these profiles and from the condition that the total energy in the flow equals  $E$  is:

$$\begin{aligned} R(t) &= \left( \frac{17Et}{\pi m_p nc} \right)^{1/4} = 3.2 \times 10^{16} \text{ cm } E_{52}^{1/4} n_1^{-1/4} t_s^{1/4}, \\ \gamma(t) &= \frac{1}{4} \left( \frac{17E}{\pi nm_p c^5 t^3} \right)^{1/8} = 260 E_{52}^{1/8} n_1^{-1/8} t_s^{-3/8}. \end{aligned} \quad (125)$$

The scalings 125 are consistent with the scalings 122 and 123 which were derived using conservation of energy and momentum. They provide the exact numerical factor that

cannot be calculated by the simple analysis of section 9.1.1. These equations can serve as a starting point for a detailed radiation emission calculation and a comparison with observations.

The Blandford-McKee solution is adiabatic and as such it does not allow for any energy losses. With some simplifying assumptions it is possible to derive a self-similar radiative solution in which an arbitrary fraction of the energy generated by the shock is radiated away [257].

### 9.2. Phases in a Relativistic Decelerating Shell

There are several phases in the deceleration of a relativistic shell: fast cooling (with either radiative or adiabatic hydrodynamics) is followed by slow cooling (with adiabatic hydrodynamics). Then if the shell is non spherical its evolution changes and a phase of sideways expansion and much faster slow down begins when the Lorentz factor reaches  $\theta^{-1}$  [258]. Finally the shell becomes Newtonian when enough mass is collected and  $\gamma \approx 1$ . In the following we estimate the time scale for the different transitions. We define  $\gamma_{e,min} \equiv c_\gamma \epsilon_e (m_p/m_e) \gamma$  and  $t_{obs} = (1+z)R/4c_t c^2$  such that the factors  $c_\gamma$  and  $c_t$  reflect some of the uncertainties in the model. The canonical values of these factors are:  $c_\gamma \approx 0.5$  and  $c_t \approx 1$ .

The deceleration begins in a fast cooling phase. If  $\epsilon_e$  is close to unity than this cooling phase will also be radiative. The first transition is from fast to slow cooling. There are several different ways to estimate this transition. One can compare the cooling time scale to the hydrodynamic time scale; alternatively one can calculate the fast cooling rate (given by the rate of energy generation by the shell) and compare it to the slow cooling rate (given by the emissivity of the relativistic electrons). We have chosen here to calculate this time as the time when the “typical electron” cools - that is when  $\nu_c = \nu_m$ :

$$t_{fs} = \begin{cases} 210 \text{ days } \epsilon_B^2 \epsilon_e^2 E_{52} n_1, & \text{ad,} \\ 4.6 \text{ days } \epsilon_B^{7/5} \epsilon_e^{7/5} E_{52}^{4/5} \gamma_{100}^{-4/5} n_1^{3/5}, & \text{rad.} \end{cases} \quad (126)$$

All methods of estimating  $t_{fs}$  give the same dependence on the parameters. However, the numerical factor is quite sensitive to the definition of this transition.

If the solution is initially radiative the transition from fast to slow cooling and from a radiative hydrodynamics to adiabatic hydrodynamics takes place at:

$$t_{rad-ad} = 1.3 \text{ days } E_{52}^{4/5} n_1^{3/5} \epsilon_e^{7/5} \epsilon_B^{7/5} ((1+z)/2)^{12/5} (127)$$

$$(c_\gamma/0.5)^{14/5} c_t^{-12/5} (\gamma_0/100)^{-4/5}.$$

During a radiative evolution the energy in the shock decreases with time. The energy that appears in Eqs. 122 in the radiative scalings is the initial energy. When a radiative shock switches to adiabatic evolution, it is necessary to use the reduced energy to calculate the subsequent adiabatic evolution. The energy  $E_{f,52}$  which one should use in the adiabatic regime is related to the initial  $E_{i,52}$  of the fireball by

$$E_{f,52} = 0.022 \epsilon_B^{-3/5} \epsilon_e^{-3/5} E_{i,52}^{4/5} \gamma_{100}^{-4/5} n_1^{-2/5}. \quad (128)$$

If the shell is not spherical and it has an opening angle:  $\theta$ , then the evolution will change when  $\gamma \sim \theta^{-1}$  [258]. Earlier on the jet expands too rapidly to expand sideways and

it evolves as if it is a part of a spherical shell. After this stage the jet expands sideways and it accumulates much more mass and slows down much faster. This transition will take place, quite generally, during the adiabatic phase at:

$$t_\theta \approx 0.5 \text{ days } E_{52}^{1/3} n_1^{-1/3} ((1+z)/2) (\theta/0.1)^{8/3} c_t^{-1} \quad (129)$$

The shell eventually becomes non relativistic. This happens at:  $R \approx l = (4E_0/4\pi n_1 m_p c^2)^{1/3}$  for an adiabatic solution. This corresponds to a transition at:

$$t_{NR,ad} \approx l/c \approx 300 \text{ days } E_{52}^{1/3} n_1^{-1/3}. \quad (130)$$

A radiative shell loses energy faster and it becomes non relativistic at  $R = L = l/\gamma_0^{1/3} = (4E_0/4\pi n_{ism} m_p c^2 \gamma_0)^{1/3}$ . This will take place at:

$$t_{NR,rad} \approx 65 \text{ days } E_{52}^{1/3} n_1^{-1/3} (\gamma_0/100)^{-1/3}. \quad (131)$$

However, the earlier estimate of the transition from fast to slow cooling suggests that the shell cannot remain radiative for such a long time.

### 9.3. Synchrotron Emission from a Relativistic Decelerating Shell

We proceed now to estimate the expected instantaneous spectrum and light curve from a relativistic decelerating shell. The task is fairly simple at this stage as all the ground rules have been set in the previous sections. We limit the discussion here to a spherical shock propagating into a homogeneous external matter. We consider two extreme limits for the hydrodynamic evolution: fully radiative and fully adiabatic. If  $\epsilon_e$  is somewhat less than unity during the fast cooling phase ( $t < t_{fs}$ ) then only a fraction of the shock energy is lost to radiation. The scalings will be intermediate between the two limits of fully radiative and fully adiabatic discussed here.

For simplicity we assume that all the observed radiation reaches the observer from the front of the shell and along the line of sight. Actually to obtain the observed spectrum we should integrate over the shell’s profile and over different angles relative to the line of sight. A full calculation [259] of the integrated spectrum over a Blandford-McKee profile shows that that different radial points from which the radiation reaches the observers simultaneously conspire to have practically the same synchrotron frequency and therefore they emit the same spectrum. Hence the radial integration over a Blandford-McKee profile does not change the observed spectrum (note that this result differs from the calculation for a homogeneous shell [255]). On the other hand the contribution from angles away from the line of sight is important and it shapes the observed spectrum, the light curve and the shape of the Afterglow (see Fig 26).

The instantaneous synchrotron spectra from a relativistic shock were described in section 8.2.4. They do not depend on the hydrodynamic evolution but rather on the instantaneous conditions at the shock front, which determines the break energies  $\nu_c$  and  $\nu_m$ . The only assumption

made is that the shock properties are fairly constant over a time scale comparable to the observation time  $t$ .

Using the adiabatic shell conditions (Eqs. 122-123), Eqs. 44 for the shock conditions, Eq. 56 for the synchrotron energy and Eq. 62 for the “cooling energy” we find:

$$\begin{aligned}\nu_c &= 2.7 \times 10^{12} \text{ Hz } \epsilon_B^{-3/2} E_{52}^{-1/2} n_1^{-1} t_d^{-1/2}, \\ \nu_m &= 5.7 \times 10^{14} \text{ Hz } \epsilon_B^{1/2} \epsilon_e^2 E_{52}^{1/2} t_d^{-3/2}, \\ F_{\nu, \text{max}} &= 1.1 \times 10^5 \mu\text{J} \epsilon_B^{1/2} E_{52} n_1^{1/2} D_{28}^{-2},\end{aligned}\quad (132)$$

where  $t_d$  is the time in days,  $D_{28} = D/10^{28}$  cm and we have ignored cosmological redshift effects. Fig. 22 depicts the instantaneous spectrum in this case.

For a fully radiative evolution we find:

$$\begin{aligned}\nu_c &= 1.3 \times 10^{13} \text{ Hz } \epsilon_B^{-3/2} E_{52}^{-4/7} \gamma_{100}^{4/7} n_1^{-13/14} t_d^{-2/7}, \\ \nu_m &= 1.2 \times 10^{14} \text{ Hz } \epsilon_B^{1/2} \epsilon_e^2 E_{52}^{4/7} \gamma_{100}^{-4/7} n_1^{-1/14} t_d^{-12/7}, \\ F_{\nu, \text{max}} &= 4.5 \times 10^3 \mu\text{J} \epsilon_B^{1/2} E_{52}^{8/7} \gamma_{100}^{-8/7} n_1^{5/14} D_{28}^{-2} t_d^{-3/7}\end{aligned}\quad (133)$$

where we have scaled the initial Lorentz factor of the ejecta by a factor of 100:  $\gamma_{100} \equiv \gamma_0/100$ . These instantaneous spectra are also shown in Fig. 22.

### 9.3.1. Light Curves

The light curves at a given frequency depend on the temporal evolution of the break frequencies  $\nu_m$  and  $\nu_c$  and the peak power  $N_e P_{\text{syn}}(\gamma_{e, \text{min}})$  (see Eq. 66). These depend, in turn, on how  $\gamma$  and  $N_e$  scale as a function of  $t$ .

The spectra presented in Fig. 22 show the positions of  $\nu_c$  and  $\nu_m$  for typical parameters. In both the adiabatic and radiative cases  $\nu_c$  decreases more slowly with time than  $\nu_m$ . Therefore, at sufficiently early times we have  $\nu_c < \nu_m$ , i.e. fast cooling. At late times we have  $\nu_c > \nu_m$ , i.e., slow cooling. The transition between the two occurs when  $\nu_c = \nu_m$  at  $t_{fs}$  (see Eq. 126). At  $t = t_{fs}$ , the spectrum changes from fast cooling (Fig. 22a) to slow cooling (Fig. 22b). In addition, if  $\epsilon_e \approx 1$ , the hydrodynamical evolution changes from radiative to adiabatic. However, if  $\epsilon_e \ll 1$ , the evolution remains adiabatic throughout.

Once we know how the break frequencies,  $\nu_c$ ,  $\nu_m$ , and the peak flux  $F_{\nu, \text{max}}$  vary with time, we can calculate the light curve. Consider a fixed frequency (e.g.  $\nu = 10^{15} \nu_{15}$  Hz). From the first two equations in (132) and (133) we see that there are two critical times,  $t_c$  and  $t_m$ , when the break frequencies,  $\nu_c$  and  $\nu_m$ , cross the observed frequency  $\nu$ :

$$t_c = \begin{cases} 7.3 \times 10^{-6} \text{ days } \epsilon_B^{-3} E_{52}^{-1} n_1^{-2} \nu_{15}^{-2}, & \text{ad}, \\ 2.7 \times 10^{-7} \text{ days } \epsilon_B^{-21/4} E_{52}^{-2} \gamma_{100}^{13/4} n_1^{-13/4} \nu_{15}^{-7/2}, & \text{rad}, \end{cases}\quad (134)$$

$$t_m = \begin{cases} 0.69 \text{ days } \epsilon_B^{1/3} \epsilon_e^{4/3} E_{52}^{1/3} \nu_{15}^{-2/3}, & \text{ad}, \\ 0.29 \text{ days } \epsilon_B^{7/24} \epsilon_e^{7/6} E_{52}^{1/3} \gamma_{100}^{-1/3} \nu_{15}^{-7/12} n_1^{-1/24}, & \text{ra.} \end{cases}\quad (135)$$

There are only two possible orderings of the three critical times,  $t_c$ ,  $t_m$ ,  $t_{fs}$ , namely  $t_{fs} > t_m > t_c$  and  $t_{fs} < t_m < t_c$ . We define the critical frequency,  $\nu_0 = \nu_c(t_{fs}) = \nu_m(t_{fs})$ :

$$\nu_0 = \begin{cases} 1.8 \times 10^{11} \epsilon_B^{-5/2} \epsilon_e^{-1} E_{52}^{-1} n_1^{-3/2} \text{ Hz,} & \text{ad}, \\ 8.5 \times 10^{12} \epsilon_B^{-19/10} \epsilon_e^{-2/5} E_{52}^{-4/5} \gamma_{100}^{4/5} n_1^{-11/10} \text{ Hz,} & \text{rad.} \end{cases}\quad (136)$$

When  $\nu > \nu_0$ , we have  $t_{fs} > t_m > t_c$  and we refer to the corresponding light curve as the *high frequency light curve*. Similarly, when  $\nu < \nu_0$ , we have  $t_{fs} < t_m < t_c$ , and we obtain the *low frequency light curve*.

Fig. 27a depicts a typical high frequency light curve. At early times the electrons cool fast and  $\nu < \nu_m$  and  $\nu < \nu_c$ . Ignoring self absorption, the situation corresponds to segment B in Fig. 22, and the flux varies as  $F_\nu \sim F_{\nu, \text{max}}(\nu/\nu_c)^{1/3}$ . If the evolution is adiabatic,  $F_{\nu, \text{max}}$  is constant, and  $F_\nu \sim t^{1/6}$ . In the radiative case,  $F_{\nu, \text{max}} \sim t^{-3/7}$  and  $F_\nu \sim t^{-1/3}$ . The scalings in the other segments, which correspond to C, D, H in Fig. 22, can be derived in a similar fashion and are shown in Fig. 27a.

Fig. 27b shows the low frequency light curve, corresponding to  $\nu < \nu_0$ . In this case, there are four phases in the light curve, corresponding to segments B, F, G and H. The time dependences of the flux are indicated on the plot for both the adiabatic and the radiative cases.

For a relativistic electron distribution with a power distribution  $\gamma^{-p}$  the uppermost spectral part behaves like  $\nu^{-p/2}$ . The corresponding temporal index (for adiabatic hydrodynamics) is  $-3p/4$ . In terms of the spectral index  $\alpha$ , this yields the relation  $F_\nu \propto t^{(1-3\alpha)/2}$ . Alternatively for slow cooling there is also another frequency range (between  $\nu_m$  and  $\nu_c$ ) for which the spectrum is given by  $\nu^{-(p-1)/2}$  and the temporal decay is  $-3(p-1)/4$ . Now we have  $F_\nu \propto t^{-3\alpha/2}$ . Note that in both cases there is a specific relation between the spectral index and the temporal index which could be tested by observations.

### 9.3.2. Parameter Fitting for GRBs from Afterglow Observation and GRB970508

Shortly after the observation of GRB970228 Mészáros *et al.* [22] showed that the decline in the intensity in X-ray and several visual bands (from B to K) fit the afterglow model well (see fig. 28). The previous discussion indicates that this agreement shows that the high energy tail (or late time behavior) is produced by a synchrotron emission from a power law distribution.

There are much more data on the afterglow of GRB970508. The light curves in the different optical bands generally peak around two days. There is a rather steep rise before the peak which is followed by a long power law decay (see figs. 6,7). In the optical band the observed power law decay for GRB970508 is  $-1.141 \pm 0.014$  [151]. This implies for an adiabatic slow cooling model (which Mészáros *et al.* [22] use) a spectral index  $\alpha = -0.761 \pm 0.009$ . However, the observed spectral index is  $\alpha = -1.12 \pm 0.04$  [260]. A fast cooling model, for which the spectral index is  $p/2$  and the temporal behavior is  $3p/4 - 1/2$ , fits the data better as the temporal power law implies that  $p = 2.188 \pm 0.019$  while the spectral index implies, consistently,  $p = 2.24 \pm 0.08$  [246, 261] (see Fig. 29). Unfortunately, at present this fit does not tell us much about the nature of the hydrodynamical processes and the slowing down.

Using both the optical and the radio data one can try to fit the whole spectrum and to obtain the unknown parameters that determine the fireball evolution [248, 249]. Wijers

and Galama [248] have attempted to do so using the spectrum of GRB970508. They have obtained a reasonable set of parameters. However, more detailed analysis [249] reveals that the solution is very sensitive to assumptions made on how to fit the observational data to the theoretical curve. Moreover, the initial phase of the light curve of GRB970508 does not fit any of the theoretical curves. This suggests that at least initially an additional process might be taking place. Because of the inability to obtain a good fit for this initial phase there is a large uncertainty in the parameters obtained in this way.

No deviation in the observed decaying light curve from a single power law was observed for GRB970508, until it faded below the level of the surrounding nebula. This suggests that there was no significant beaming in this case. If the outflow is in the form of a jet the temporal behavior will change drastically when the opening angle of the jet equals  $1/\gamma$  [258].

#### 9.4. *New Puzzles from Afterglow observations*

Afterglow observations fit well the fireball picture that was developed for explaining the GRB phenomena. The available data is not good enough to distinguish between different specific models. But in the future we expect to be able to distinguish between those models and even to be able to determine the parameters of the burst  $E$  and  $\gamma_0$  (if the data is taken early enough), the surrounding ISM density and the intrinsic parameters of the relativistic shock  $\epsilon_e$ ,  $\epsilon_B$  and  $p$ . Still the current data is sufficient to raise new puzzles and present us with new questions.

- **Why afterglow accompany some GRBs and not others?**

X-ray, Optical and radio afterglows have been observed in some bursts but not in others. According to the current model afterglow is produced when the ejecta that produced the GRB is shocked by the surrounding matter. Possible explanations to this puzzle invoke environmental effects. A detectable afterglow might be generated efficiently in some range of ISM densities and inefficiently in another. High ISM densities would slow down of the ejecta more rapidly. This could make some afterglows detectable and others undetectable. ISM absorption is another alternative. While most interstellar environments are optically thin to gamma-rays high density ISM regions can absorb and attenuate efficiently x-rays and optical radiation.

- **Jets and the Energy of GRB971214**

How can we explain the  $10^{53}$ ergs required for isotropic emission in GRB971214? As we discuss in the next section this amount is marginal for most models that are based on the formation of a compact source. This problem can be resolved if we invoke beaming, with  $\theta \sim 0.1$ . However, such beaming would result in a break at the light curve when the local Lorentz factor would reach a value of  $1/\theta$ . Such a break was not seen in other afterglows for which there are good data. Note that recently Perna & Loeb [263] inferred from the lack of radio transients

that GRB beams cannot be very narrow. If typical GRBs are beamed, the beam width  $\theta$  should be larger than  $6^\circ$ .

- **GRB980425 and SN1998bw**

SN1998bw (and the associated GRB980425) is a factor of a hundred nearer than a typical GRB (which are expected to be at  $z \sim 1$ ). The corresponding (isotropic) gamma-ray energy,  $\sim 5 \times 10^{47}$ ergs, is four order of magnitude lower than a regular burst. This can be in agreement with the peak flux distribution only if the bursts with such a low luminosity compose a very small fraction of GRBs. This leads naturally to the question is there an observational coincidence between GRBs and SNs? To which there are conflicting answers [264, 265, 266].

## 10. MODELS OF THE INNER ENGINE

We turn now to the most difficult part: the nature of the beast that produces the GRB-modeling of the Inner Engine. We examine a few general considerations in section 10.1 and then we turn to the Binary Neutron star merger model in 10.2.

### 10.1. *The “Inner Engine”*

The fireball model is based on an “inner engine” that supplies the energy and accelerates the baryons. This “engine” is well hidden from direct observations and it is impossible to determine what is it from current observations. Unfortunately, the discovery of afterglow does not shed additional direct light on this issue. However it adds some indirect evidence from the association of the location of the bursts in star forming regions.

Once the cosmological origin of GRBs was established we had two direct clues on the nature of the “inner engine”: the rate and the energy output. GRBs occur at a rate of about one per  $10^6$  years per galaxy [56] and the total energy is  $\sim 10^{52}$ ergs. These estimates assume isotropic emission. Beaming with an angle  $\theta$  changes these estimates by a factor  $4\pi/\theta^2$  in the rate and  $\theta^2/4\pi$  in the total energy involved. These estimates are also based on the assumption that the burst rate does not vary with cosmic time. The observations that GRB hosts are star forming galaxies [16, 129, 130, 131, 128] indicates that the rate of GRBs may follow the star formation rate [193, 194, 195]. In this case the bursts are further and they take place at a lower rate and have significantly higher energy output.

The fireball model poses an additional constraint: the inner engine should be capable of accelerating  $\sim 10^{-5} M_\odot$  to relativistic energies. One can imagine various scenarios in which  $10^{52}$ ergs are generated within a short time. The requirement that this energy should be converted to a relativistic flow is much more difficult as it requires a “clean” system with a very low but non zero baryonic load. This requirement suggests a preference for models based on electromagnetic energy transfer or electromagnetic energy generation as these could more naturally satisfy this condition (see [267, 224, 69, 227]). Paczyński [46] has recently suggested a unique hydrodynamical model in which  $10^{54}$ ergs are dumped into an atmosphere with a decreasing density profile. This is a cosmological variant of Colgate’s [262] galactic model. This would lead to an acceleration

of fewer and fewer baryons and eventually to a relativistic velocities. Overall one could say that the “baryonic load” problem is presently the most bothersome open question in the “fireball model”.

The recent realization that energy conversion is most likely via internal shocks rather than via external shocks provides additional information about the inner engine: The relativistic flow must be irregular (to produce the internal shocks), it must be variable on a short time scale (as this time scale is seen in the variability of the bursts), and it must be active for up to a few hundred seconds and possibly much longer [36] - as this determines the observed duration of the burst. These requirements rule out all explosive models. The engine must be compact ( $\sim 10^7$  cm) to produce the observed variability and it must operate for a million light crossing times to produce a few hundred-second signals.

There are more than a hundred GRB models [268]. At a certain stage, before BATSE, there were probably more models than observed bursts. Most of these models are, however, galactic and those have been ruled out if we accept the cosmological origin of GRBs. This leaves a rather modest list of viable GRB models: binary neutron star mergers - NS<sup>2</sup>Ms - [35] (see also [269, 270, 53, 271, 272]), failed supernova [273], white dwarf collapse [267] and hypernova [46]. All these are based on the formation of a compact object of one type or another and the release of its binding energy. With a binding energy of  $\sim 5 \times 10^{53}$  ergs or higher, all these models have, in principle, enough energy to power a GRB. However they face similar difficulties in channeling enough energy to a relativistic flow. This would be particularly difficult if indeed  $10^{53}$  ergs are needed, as some recent burst have indicated. Paczyński’s hypernova is an exception as in this model all the energy is channeled initially to a non-relativistic flow and only later a small fraction of it is converted to relativistic baryons. All these models are consistent with the possibility that GRBs are associated with star forming regions as the life time of massive stars is quite short and even the typical life time of a neutron star binary ( $\sim 10^8$  yr) is sufficiently short to allow for this coincidence. -

Other models are based on an association of GRBs with massive black holes associated with Quasars or AGNs in galactic centers (e.g. [274]). These are ruled out as all GRBs with optical afterglow are not associated with such objects. Furthermore, such objects do not appear in other small GRB error boxes searched by Schaefer *et al.* [126]. From a theoretical point of view it is difficult to explain the observed energy and time scales with such objects.

### 10.2. NS<sup>2</sup>Ms: Binary Neutron Star Mergers

Binary neutron star mergers (NS<sup>2</sup>Ms) [35] or, with a small variant: neutron star-black hole mergers [271] are probably the best candidates for GRB sources. These mergers take place because of the decay of the binary orbits due to gravitational radiation emission. A NS<sup>2</sup>M results, most likely, in a rotating black hole [276]. The process releases  $\approx 5 \times 10^{53}$  ergs [277]. Most of this energy escapes as neutrinos and gravitational radiation, but a small fraction of this energy suffices to power a GRB. The discovery of the famous binary pulsar PSR 1913+16 [48] demonstrated that this decay is taking place [275].

The discovery of other binary pulsars, and in particular of PSR 1534+12 [278], has shown that PSR 1913+16 is not unique and that such systems are common. These observations suggest that NS<sup>2</sup>Ms take place at a rate of  $\approx 10^{-6}$  events per year per galaxy [50, 51, 52]. This rate is comparable to the simple estimate of the GRB event rate (assuming no beaming and no cosmic evolution of the rate) [56, 272, 183].

It has been suggested [279, 280] that most neutron star binaries are born with very close orbits and hence with very short lifetimes (see however, [281, 282]). If this idea is correct, then the merger rate will be much higher. This will destroy, of course, the nice agreement between the rates of GRBs and NS<sup>2</sup>Ms. Consistency can be restored if we invoke beaming, which might even be advantageous as far as the energy budget is concerned. Unfortunately, the short lifetime of those systems, which is the essence of this idea means that at any given moment of time there are only about a hundred such systems in the Galaxy (compared to about  $10^5$  wider neutron star binaries). This makes it very hard to confirm or rule out this speculation. We should be extremely lucky to detect such a system.

It is not clear yet how NS<sup>2</sup>Ms form. The question is how does the system survive the second supernova event? The binary system will be disrupted if this explosion ejects more than half of its total mass. There are two competing scenarios for the formation of NS<sup>2</sup>Ms. In one scenario the first neutron star that forms sinks into the envelope of its giant companion and its motion within this envelope lead to a strong wind that carries away most of the secondary’s mass. When the secondary reaches core collapse it has only a small envelope and the total mass ejected is rather small. In a second scenario the second supernova explosion is asymmetric. The asymmetric explosion gives a velocity of a few hundred km/sec to the newborn neutron star. In a fraction of the cases this velocity is in the right direction to keep the binary together. Such a binary system will have a comparable center of mass velocity [28, 283, 284, 285]. This second scenario has several advantages. First it explains both the existence of binary neutron stars and the existence of high velocity pulsars [283, 286]. Second, and more relevant to GRBs, with these kick velocities these binaries could escape from their parent galaxy, provided that this galaxy is small enough. Such escaping binaries will travel a distance of  $\sim 200$  kpc ( $v/200$  km/sec) ( $T/10^9$  yr) before they merge. The GRB will occur when the system is at a distance of the order of hundred kpc from the parent galaxy. Clearly there is no “no host” problem in this case [28].

While a NS<sup>2</sup>M has enough energy available to power a GRB it is not clear how the GRB is produced. A central question is, of course, how does a NS<sup>2</sup>M generate the relativistic wind required to power a GRB. Most of the binding energy (which is around  $5 \times 10^{53}$  ergs escapes as neutrinos [277]. Eichler *et al.* [35] suggested that about one thousandth of these neutrinos annihilate and produce pairs that in turn produce gamma-rays via  $\nu\bar{\nu} \rightarrow e^+e^- \rightarrow \gamma\gamma$ . This idea was criticized on several grounds by different authors. Jaroszynski [288] pointed out that a large fraction of the neutrinos will be swallowed by the black hole that forms. Davies *et al.* [276] and Ruffert & Janka [289, 290, 291] who simulated neutron star

mergers suggested that the central object won't be warm enough to produce a significant neutrino flux because the merger is nearly adiabatic [69]. The neutrinos are also emitted over a diffusion time of several seconds, too long to explain the rapid variations observed in GRB [79], but to short to explain the observed GRB durations. Wilson & Mathews [292, 293] included approximate general relativistic effects in a numerical simulation of a neutron star merger. They found that the neutron stars collapse to a single black hole before they collide with each other. This again will suppress the neutrino emission from the merger. However, the approximation that they have used has been criticized by various authors and it is not clear yet that the results are valid. Others suggested that the neutrino wind will carry too many baryons. However, it seems that the most severe problem with this model stems from the fact that the prompt neutrino burst could produce only a single smooth pulse. This explosive burst is incompatible with the internal shocks scenario.

An alternative source of energy within the NS<sup>2</sup>M is the accretion power of a disk that forms around the black hole [28, 69, 227]. Various numerical simulations of neutron star mergers [276, 289, 290, 291] find that a  $\sim 0.1 M_{\odot}$  forms around the central black hole. Accretion of this disk on the central black hole may take a few dozen seconds [69]. It may produce the wind needed to produce internal shocks that could produce, in turn a GRB.

How can one prove or disprove this, or any other, GRB model? Theoretical studies concerning specific details of the model can, of course, make it more or less appealing. But in view of the fact that the observed radiation emerges from a distant region which is very far from the inner "engine" I doubt if this will ever be sufficient. It seems that the only way to confirm any GRB model will be via detecting in time-coincidence another astronomical phenomenon, whose source could be identified with certainty. Unfortunately while the recent afterglow observations take us closer to this target they do not tell us what are the sources of GRBs. We still have to search for additional signals.

NS<sup>2</sup>Ms have two accompanying signals, a neutrino signal and a gravitational radiation signal. Both signals are extremely difficult to detect. The neutrino signal could be emitted by some of the other sources that are based on a core collapse. Furthermore, with present technology detection of neutrino signals from a cosmological distance is impossible. On the other hand the gravitational radiation signal has a unique characteristic form. This provides a clear prediction of coincidence that could be proved or falsified sometime in the not too distant future when suitable gravitational radiation detectors will become operational.

### 10.3. *Binary Neutron Stars vs. Black Hole - Neutron star Mergers*

We have grouped together binary neutron star mergers and black-hole neutron star mergers. At present several neutron star binaries are known while no black hole - neutron star binary was found. Still on theoretical grounds one should expect a similar rate for both events [50]. Some even suggest that there are more black hole - neutron star binaries than neutron star-neutron star binaries [282]. There is a lot of similarity between the two processes which

are both driven by gravitational radiation emission and both result in a single black hole. First, unless the mass of the black hole is of rather small the neutron star will not be tidally disrupted before it is captured by the black hole. Even if such a tidal disruption will take place then while in the binary neutron star merger we expect a collision, in the black hole - neutron star merger we expect at most a tidal disruption followed by infall of the debris on the black hole.

This could lead to a situation in which one of the two events will produce a GRB and the other will not. Presently it is too difficult to speculate which of the two is the right one. One should recall, however, that there is a marked difference between the gravitational signature of those events and thus hopefully when we discover a coincidence between a GRB and a gravitational radiation signal we would also be able to find which of the two mechanism is the right one.

## 11. OTHER RELATED PHENOMENA

It is quite likely that other particles (in addition to  $\gamma$ -rays) are emitted in these events. Let  $f_{x\gamma}$  be the ratio of energy emitted in other particles relative to  $\gamma$ -rays. These particles will appear as a burst accompanying the GRB. The total fluence of a "typical" GRB observed by BATSE,  $F_{\gamma}$  is  $10^{-7}$  ergs/cm<sup>2</sup>, and the fluence of a "strong" burst is about hundred times larger. Therefore we should expect accompanying bursts with typical fluences of:

$$F_x \mid_{prompt} = 10^{-3} \frac{\text{particles}}{\text{cm}^2} f_{x\gamma} \left( \frac{F_{\gamma}}{10^{-7} \text{ergs/cm}^2} \right) \left( \frac{E_x}{\text{GeV}} \right)^{-1}, \quad (137)$$

where  $E_x$  is the energy of these particles. This burst will be spread in time and delayed relative to the GRB if the particles do not move at the speed of light. Relativistic time delay will be significant (larger than 10 seconds) if the particles are not massless and their Lorentz factor is smaller than  $10^8$ ! similarly a deflection angle of  $10^{-8}$  will cause a significant time delay.

In addition to the prompt burst we should expect a continuous background of these particles. With one  $10^{51}$  ergs GRB per  $10^6$  years per galaxy we expect  $\sim 10^4$  events per galaxy in a Hubble time (provided of course that the event rate is constant in time). This corresponds to a background flux of

$$F_x \mid_{bg} = 3 \cdot 10^{-8} \frac{\text{particles}}{\text{cm}^2 \text{sec}} f_{x\gamma} \left( \frac{E_{\gamma}}{10^{51} \text{ergs}} \right) \left( \frac{R}{10^{-6} \text{y/galaxy}} \right) \left( \frac{E_x}{\text{GeV}} \right)^{-1}. \quad (138)$$

For any specific particle that could be produced one should calculate the ratio  $f_{x\gamma}$  and then compare the expected fluxes with fluxes from other sources and with the capabilities of current detectors. One should distinguish between two types of predictions: (i) Predictions of the generic fireball model which include low energy cosmic rays [220], UCHERs [294, 295, 296] and high energy neutrinos [297] and (ii) Predictions of specific models and in particular the NS<sup>2</sup>M model. These include low energy neutrinos [277] and gravitational waves [35, 301].

### 11.1. Cosmic Rays

Already in 1990, Shemi & Piran [220] pointed out that fireball model is closely related to Cosmic Rays. A “standard” fireball model involved the acceleration of  $\sim 10^{-7} M_{\odot}$  of baryons to a typical energy of 100GeV per baryon. Protons that leak out of the fireball will become low energy cosmic rays. However, a comparison of the GRB rate (one per  $10^6$  years per galaxy) with the observed low energy cosmic rays flux, suggests that even if  $f_{CR-\gamma} \approx 1$  this will amount only to 1% to 10% of the observed cosmic ray flux at these energies. Cosmic rays are believed to be produced by SNRs. Since supernovae are ten thousand times more frequent than GRBs, unless GRBs are much more efficient in producing Cosmic Rays in some specific energy range their contribution will be swamped by the SNR contribution.

### 11.2. UCHERs - Ultra High Energy Cosmic Rays

Waxman [294] and Vietri [295] have shown that the observed flux of UCHERs (above  $10^{19}$ eV) is consistent with the idea that these are produced by the fireball shocks provided that  $f_{UCHERs-\gamma} \approx 1$ . Milgrom & Usov [296] pointed out that the error boxes of the two highest energy UCHERs contain strong GRBs - suggesting an association between the two phenomena. The relativistic fireball shocks that appear in GRBs are among the few astronomical objects that satisfy the conditions for shock acceleration of UCHERs. Waxman [298] has shown that the spectrum of UCHERs is consistent with the one expected from Fermi acceleration within those shocks.

### 11.3. High Energy Neutrinos

Waxman & Bahcall [297] suggested that collisions between protons and photons within the relativistic fireball shocks produce pions. These pions produce high energy neutrinos with  $E_{\nu} \sim 10^{14}$ eV and  $f_{\text{high energy } \nu-\gamma} > 0.1$ . The flux of these neutrinos is comparable to the flux of atmospheric neutrinos but those will be correlated with the position of strong GRBs. This signal might be detected in future  $\text{km}^2$  size neutrino detectors.

### 11.4. Gravitational Waves

If GRBs are associated with NS<sup>2</sup>M then they will be associated with gravitational waves and low energy neutrinos. The spiraling in phase of a NS<sup>2</sup>M produces a clean chirping gravitational radiation signal. This signal is the prime target of LIGO [299] and VIRGO, the two [300] large interferometers that are build now in the USA and in Europe. The observational scheme of these detectors is heavily dependent on digging deeply into the noise. Kochanek & Piran [301] suggested that a coincidence between a chirping gravitational radiation signal from a neutron star merger and a GRB could enhance greatly the statistical significance of the detection of the gravitational radiation signal. At the same time this will also verify the NS<sup>2</sup>M GRB model.

### 11.5. Low Energy Neutrinos

Most of the energy generated in any core collapse event and in particular in NS<sup>2</sup>M is released as low energy ( $\sim$

$5 - 10\text{MeV}$ ) neutrinos [277]. The total energy is quite large  $\sim$  a few  $\times 10^{53}$ ergs, leading to  $f_{\text{low energy } \nu-\gamma} \approx 10$ . However, this neutrino signal will be quite similar to a supernova neutrino signal, and at present only galactic SN neutrinos can be detected. Supernovae are ten thousand times more frequent than GRBs and therefore low energy neutrinos associated with GRB constitute an insignificant contribution to the background at this energy range.

### 11.6. Black Holes

An NS<sup>2</sup>M results, inevitably, in a black hole [276]. Thus a direct implication of the NS<sup>2</sup>M model is that GRBs signal to us (indirectly) that a black hole has just (with the appropriate time of flight in mind) formed.

## 12. COSMOLOGICAL IMPLICATIONS

Cosmological GRBs seem to be a relatively homogeneous population of sources with a narrow luminosity function (the peak luminosity of GRBs varies by less than a factor of 10 [183, 186]) that is located at relatively high redshifts [56, 302, 303, 304, 183]. The universe and our Galaxy are transparent to MeV  $\gamma$ -rays (see e.g. [305]). Hence GRBs constitute a unique homogeneous population of sources which does not suffer from any angular distortion due to absorption by the Galaxy or by any other object. Could GRBs be the holy grail of Cosmology and provide us with the standard candles needed to determine the cosmological parameters  $H_0$ ,  $\Omega$ , and  $\Lambda$ ? Lacking any spectral feature, there is no indication of the redshift of individual bursts. The available number vs. peak luminosity distribution is not suitable to distinguish between different cosmological models even when the sources are perfect standard candles with no source evolution [183].

The situation might be different if optical afterglow observations would yield an independent redshift measurement of a large number of bursts. If the GRB luminosity function is narrow enough this might allow us, in the future, to determine the cosmological closure parameter  $\Omega$  using a peak-flux vs. red-shift diagram (or the equivalent more common magnitude - red-shift diagram). For example a hundred bursts with a measured  $z$  are needed to estimate  $\Omega$  with an accuracy of  $\sigma_{\Omega} = 0.2$ , if  $\sigma_L/L = 1$  [201].

Currently, the rate of detection of bursts with counterparts is a few per year and of those detected until now only two have a measured red-shift. This rate is far too low for any cosmological measurement. However, there is an enormous potential for improvements. For example, systematic measurements of the red-shift of all bursts observed by BATSE ( $\approx 300$  per year) would yield an independent estimate of  $\Omega$ , with  $\sigma_{\Omega} = 0.1$ , even if the luminosity function is wide, ( $\sigma_L/L = 0.9$ ), within one year.

Direct redshift measurements would also enable us to determine the cosmological evolution of the rate of GRBs [201]. Most current cosmological GRB models suggest that the GRB rate follows (with a rather short time delay) the rate of star formation [306]. Consequently measurements of the rate of GRBs as a function of the red-shift will provide an independent tool to study star formation and galactic evolution.

It is also expected that the bursts' sources follow the matter distribution. Then GRBs can map the large scale structure of the Universe on scales that cannot be spanned directly otherwise. Lamb & Quashnock [307] have pointed out that a population of several thousand cosmological bursts should show angular deviations from isotropy on a scale of a few degrees. This would immediately lead to new interesting cosmological limits. So far there is no detected anisotropy in the 1112 bursts of the BATSE 3B catalog [308]. But the potential of this population is clear and quite promising. A more ambitious project would be to measure the multipole moments of the GRB distribution and from this to estimate cosmological parameters [58]. However, it seems that too many bursts are required to overcome the signal to noise ratio in such measurements.

GRBs can also serve to explore cosmology as a background population which could be lensed by foreground objects [53]. While standard gravitational lensed object appears as several images of the same objects, the low angular resolution of GRB detectors is insufficient to distinguish between the positions of different images of a lensed GRB. However, the time delay along the different lines of sight of a gravitationally lensed burst will cause such a burst to appear as repeated bursts with the same time profile but different intensities from practically the same position on the sky. Mao [309] estimated that the probability for lensing of a GRB by a regular foreground galaxy is 0.04%-0.4%. Hence the lack of a confirmed lensed event so far [310] is not problematic yet. In the future, the statistics of lensed bursts could probe the nature of the lensing objects and the dark matter of the Universe [54]. The fact that no lensed bursts have been detected so far is sufficient to rule out a critical density ( $\Omega = 1$ ) of  $10^{6.5} M_{\odot}$  to  $10^{8.1} M_{\odot}$  black holes [55]. Truly, this was not the leading candidate for cosmological dark matter. Still this result is a demonstration of the power of this technique and the potential of GRB lensing. The statistics of lensing depends on the distance to the lensed objects which is quite uncertain at present. The detection of a significant number of counterparts whose red-shift could be measured would improve significantly this technique as well.

### 13. SUMMARY AND CONCLUSIONS

Some thirty years after the discovery of GRBs a generic GRB model is beginning to emerge. The observations of isotropy, peak flux distribution and time dilation indicated that GRBs are cosmological. The measurement of a redshift provided a final confirmation for this idea. All cosmological models are based on the fireball mode. The discovery of the afterglow confirmed this general scheme.

The Fireball-Internal-External Shocks model seems to have the necessary ingredients to explain the observations. Relativistic motion, which is the key component of all Fireball Model provided the solution for the compactness problem. The existence of such motion was confirmed by the radio afterglow observations in GRB970508. Energy conversion via internal shocks can produce the observed highly variable light curves while the external shock model agrees, at least qualitatively, with afterglow observations. There are some indications that the two kind of shocks might combine and operate within the GRB itself producing two different components of the signal. This fireball model has

some fascinating immediate implications on accompanying UCHER and high energy neutrino signals. An observations of these phenomena in coincidence with a GRB could provide a final confirmation of this model.

In spite of this progress we are still far from a complete solution. There are many open questions that has to be resolved. Within the internal-external shocks model there is a nagging efficiency problem in conversion of the initial kinetic energy to the observed radiation. If the overall efficiency is too low the initial energy required might be larger than  $10^{53}$  ergs and it is difficult to imagine a source that could provide so much energy. Beaming might provide a solution to this energy crisis. However, so far there is no indication for the corresponding break in the afterglow light curve, which is essential in any relativistic beaming model when  $\gamma \sim \theta^{-1}$ . These last two facts might be consistent if GRB970508 took place within a very low density ISM - an issue that should be explored further. Afterglow observations agree qualitatively, but not quantitatively with the model. Better observations and more detailed theoretical modeling are needed. Another nagging open question is what determines the appearance of afterglow. Why there was no X-ray afterglow in the very strong 970111? Why was optical afterglow observed in GRB970228 and in GRB970508 but it was not seen in others (in particular in GRB970828 [46])? Finally we turn to the GRB itself and wonder why is the observed radiation always in the soft  $\gamma$ -ray band? Is there an observational bias? Are there other bursts that are not observed by current instruments? If there are none and we do observe all or most of the bursts why is the emitted radiation always in the soft gamma-ray range? Why it is insensitive to a likely variability in the Lorentz factors of the relativistic flow and to variability of other parameters in the model.

While there are many open questions concerning the fireball and the radiation emitting regions the first and foremost open question concerning GRBs is what are the inner engines that power GRBs? In spite of all the recent progress we still don't know what produces GRBs. My personal impression is that binary neutron mergers are the best candidates. But other models that are based on the formation of a compact object and release a significant amount of its binding energy on a short time scale are also viable. A nagging question in all these models is what produces the the "observed" ultra-relativistic flow? How are  $\sim 10^{-5} M_{\odot}$  of baryons accelerated to an ultra-relativistic velocity with  $\gamma \sim 100$  or larger? Why is the baryonic load so low? Why isn't it lower? There is no simple model for that. An ingenious theoretical idea is clearly needed here.

However, I believe that theoretical reasoning won't be enough and only observations can provide a final resolution of the questions what is are the sources of GRBs? The binary neutron star merger model has one specific observational prediction: A coincidence between a (near by and therefore strong) GRB and a characteristic gravitational radiation signal. Luckily these events have a unique gravitational radiation signature. The detection of these gravitational radiation events is the prime target of three gravitational radiation detector that are being built now. Hopefully they will become operational within the next decade and their observations might confirm or rule out this model. Such predictions, of an independently ob-

served phenomena are clearly needed for all other competing models.

GRBs seem to be the most relativistic phenomenon discovered so far. They involve a macroscopic relativistic motion not found elsewhere before. As cosmological objects they display numerous relativistic cosmological phenomena. According to the NS<sup>2</sup>M model they are associated with the best sources for gravitational radiation emission

and more than that they signal, though in directly, the formation of a new black hole.

I thank E. Cohen, J. Granot, J. I. Katz, S. Kobayashi, R. Narayan, and R. Sari for many helpful discussions and D. Band and G. Blumenthal for helpful remarks. This work was supported by the US-Israel BSF grant 95-328 and by NASA grant NAG5-3516.

## REFERENCES

- [1] Klebesadel, R.W., Strong, I.B., & Olson, R.A. 1973, *Ap. J. Lett.*, **182**, L85.
- [2] Mazets, E.P., Golenetskii, S.V., & Illnskii, V.N., 1974, *JETP Lett.*, **19**, 77.
- [3] Cline, T., 1973, *Ap. J. Lett.*, **185**, L1.
- [4] Hillier, R., *Gamma-Ray Astronomy*, 1984, Clarendon Press, Oxford, England.
- [5] Ramana Murthy, P.V., & Wolfendale A.W., *Gamma-Ray Astronomy*, 1986, Cambridge University Press, Cambridge, England.
- [6] Mészáros, P., *High Energy Radiation from Magnetized Neutron Stars*, 1992, The University of Chicago Press.
- [7] Cline, T.L., 1992, in: *The Astronomy & Astrophysics Encyclopedia*, Ed. Maran, S.P., Van Nostrand Reinhold & Cambridge University Press, p. 284.
- [8] Luminet, J.P., 1992, in: *The Cambridge Atlas of Astronomy*, Eds. Adouze, J., & Israel, G., Cambridge University Press.
- [9] Meegan, C.A., *et al.*, 1992, *Nature*, **355**, 143.
- [10] Costa, E., *et al.*, 1997, *Nature*, **387**, 783.
- [11] van Paradijs, J., *et al.*, 1997, *Nature*, **386**, 686.
- [12] Bond, H.E., 1997, IAU circ. 6665.
- [13] Frail, D.A., *et al.*, 1997, *Nature*, **389**, 261.
- [14] Metzger, M.R., *et al.*, 1997, *Nature*, **387**, 878.
- [15] Kulkarni, S., *et al.*, 1998, *Nature*, **393**, 35.
- [16] Djorgovski, S. G., *et al.*, 1998, CGN notice 139.
- [17] Paczyński, B., & Rhoads, J., 1993, *Ap. J. Lett.*, **418**, L5.
- [18] Katz, J.I., 1994, *Ap. J.*, **422**, 248.
- [19] Katz, J.I., 1994, *Ap. J.*, **432**, L107.
- [20] Sari, R., & Piran, T., 1997, *Ap. J.*, **485**, 270. astro-ph/9701002.
- [21] Mészáros, P., & Rees, M.J., 1997, *Ap. J.*, **476**, 232.
- [22] Wijers, A.M.J., Rees, M.J., and Mészáros, P., 1997, *MNRAS*, **288**, L51.
- [23] Waxman, E., 1997, *Ap. J. Lett.* **485**, L5.
- [24] Vietri, M., 1997, *Ap. J. Lett.* **478**, L9.
- [25] Katz, J.I., & Piran, T., 1997, *Ap. J.*, **490**, 772.
- [26] Katz, J.I., & Piran, T., 1997, in: in C. Meegan, R. Preece & T. Koshut, Eds., *Gamma-Ray Bursts 4th Huntsville Symposium* AIP Conf. Proc. 428 (New York: AIP)
- [27] Mészáros, P., & Rees, M.J., 1992, *MNRAS*, **258**, 41P.
- [28] Narayan, R., Paczyński, B., & Piran, T., 1992, *Ap. J. Lett.*, **395**, L83.
- [29] Rees, M. J., & Mészáros, P., 1994, *Ap. J. Lett.*, **430**, L93.
- [30] Paczyński, B., & Xu, G., 1994, *Ap. J.*, **427**, 709.
- [31] Piran, T., 1997, in: *Some Unsolved Problems in Astrophysics*, Eds. Bahcall, J.N., & Ostriker, J.P., Princeton University Press.
- [32] MochkovitchSK, R., Maitia, V., & Marques, R., 1995, in: *Towards the Source of Gamma-Ray Bursts*, *Proceedings of 29th E-ELAB Symposium*, Eds. Bennett, K., & Winkler, C., 531.
- [33] Kobayashi, S., Piran, T., & Sari, R., 1997, *Ap. J.*, **490**, 92.
- [34] Mochkovitch, R. & Daigne, F., 1997, in: in C. Meegan, R. Preece & T. Koshut, Eds., *Gamma-Ray Bursts 4th Huntsville Symposium* AIP Conf. Proc. 428 (New York: AIP)
- [35] Eichler, D., Livio, M., Piran, T., and Schramm, D. N., 1989, *Nature*, **340**, 126.
- [36] Katz, J.I., Piran, T., & Sari, R., 1998, *Phys. Rev. Lett.*, **80**, 1580.
- [37] Fishman, G.J., & Meegan, C.A. 1995, *ARA&A*, **33**, 415.
- [38] Fishman, J.G., 1995, *PASP*, **107**, 1145.
- [39] Briggs, M.S., 1995, *Ap&SS*, **231**, 3.
- [40] Kouveliotou, C., 1995, to appear in: *Proceedings of the International School of Astrophysics, D. Chalonge*.
- [41] Hartmann, D., 1995, *A&A Rev.*, **6**, 225.
- [42] Paciesas, W. S., & Fishman G. J., Eds., 1991, *AIP Conf. Proc.*, **265**, *Gamma-Ray Bursts*, (New York: AIP).
- [43] Fishman, G.J., Brainerd, J.J., & Hurley, K., Eds., 1994, *AIP Conference Proceedings*, **307**, *Gamma-Ray Bursts, Second Workshop, Huntsville, Alabama*, (New York: AIP).
- [44] Kouveliotou, C., Briggs, M.S., & Fishman, G.J., Eds., 1995, *AIP Conf. Proc.* **384**, *Gamma-Ray Bursts, 3rd Huntsville Symposium*, (New York: AIP).
- [45] Meegan, C., Preece, R., & Koshut, T., Eds., *Gamma-Ray Bursts, 4th Huntsville Symposium*, (New York: AIP).
- [46] Paczyński, B., 1998, *Ap. J. Lett.*, **494**, L45, (see also astro-ph/9706232).
- [47] Mészáros, P., Rees, M.J., & Wijers, A.M.J., 1997, *Astro-ph*/9709273.
- [48] Hulse, R.A., & Taylor, J.H., 1975, *Ap. J.*, **368**, 504.
- [49] Clark, J.P.A., & Eardley, D., 1977, *Ap. J.*, **215**, 311.
- [50] Narayan, R., Piran, T., & Shemi, A., 1991, *Ap. J. Lett.*, **379**, L1.
- [51] Phinney, E.S., 1991, *Ap. J.*, **380**, L17.
- [52] van den Heuvel, E.P.J., & Lorimer, D.R., 1996, *MNRAS*, **283**, L37.
- [53] Paczyński, B., 1986, *Ap. J. Lett.*, **308**, L43.
- [54] Blaes, O.M., & Webster, R.L., 1992, *Ap. J.*, **391**, L66.
- [55] Nemiroff, R.J., *et al.*, 1993, *Ap. J.*, **414**, 36.
- [56] Piran, T., 1992, *Ap. J. Lett.*, **389**, L45.
- [57] Lamb, D.Q., & Quashnock, J.M., 1993, *Ap. J. Lett.*, **415**, L1.
- [58] Piran, T., & Singh, A., 1997, *Ap. J.*, **483**, 552.
- [59] Hurley, K., in: in C. Meegan, R. Preece & T. Koshut, Eds., *Gamma-Ray Bursts 4th Huntsville Symposium* AIP Conf. Proc. 428 (New York: AIP)
- [60] Fishman, G.J., *et al.*, 1993, *A&A Supp.*, **97**, 17.
- [61] Klebesadel, R., Laros, J., & Fenimore, E.E., 1984, *BAAS*, **16**, 1016.
- [62] Koshut, T.M., *et al.*, 1995, *Ap. J.*, **452**, 145.
- [63] Laros, J., *et al.*, 1995, *Proc. 19th ICRC, San Diego, California*, OG 1.1-2, 5.
- [64] Murakami, T., *et al.*, 1991, *Nature*, **350**, 592.
- [65] Yoshida, A., *et al.*, 1989, *PASJ*, **41**, 509.
- [66] Bhat, P.N., *et al.*, 1992, *Nature*, **359**, 217.
- [67] Hurley, K., 1994, *Ap. J. Supp.*, **90**, 857.
- [68] Meegan, C., *et al.*, 1996, *IAU Circ.* 6518.
- [69] Katz, J.I., 1997, *Ap. J.*, **490**, 633.
- [70] Hurley, K., 1992, in: *Gamma ray Bursts*, Paciesas, W., & Fishman, G.J., Eds., (AIP: New York) p. 3.
- [71] Mazet, E.P., *et al.*, 1981, *Ap. Space Sci.*, **80**, 3.
- [72] Kouveliotou, C., *et al.*, 1993, *Ap. J.*, **413**, L101.
- [73] Lamb, D.Q., Graziani, C., & Smith, I.A., 1993, *Ap. J.*, **413**, L11.
- [74] Mao, S., Narayan, R., & Piran, T., 1994, *Ap. J.*, **420**, 171.
- [75] Klebesadel, R.W., 1992, in: *Gamma-Ray Bursts*, Ho, C., Epstein, R.I., & Fenimore, E.E., Eds. (Cambridge University Press), p. 161.
- [76] Dezaley, J.-P., *et al.*, 1992, in: in Fishman, G. J., & Brainerd, J. J., Eds., *Gamma-Ray Bursts 2nd Huntsville Symposium* AIP Conf. Proc. 307 (New York: AIP).
- [77] Cohen, E., Kollat, T., & Piran, T., 1994, *Astro-ph*/9406012.
- [78] Piran, T., 1996, in: *IAU Symposium 165 on Compact Stars in Binaries*, van den Heuvel, E.P.J., & van den Paradijs, J., Eds., The Hague, Netherlands, 15-19 Aug. 1995, Kluwer Publishing, 489.
- [79] Katz, J.I., & Cane, L.M., 1996, *Ap. J.*, **471**, 527.
- [80] Park, H.S., *et al.*, 1997, *Ap. J. Lett.*, in press, *Astro-ph*/9708130.
- [81] Hurley, K., *et al.*, 1994, *Nature*, **372**, 652.
- [82] Dingus, B., *et al.*, 1997, in: in C. Meegan, R. Preece & T. Koshut, Eds., *Gamma-Ray Bursts 4th Huntsville Symposium* AIP Conf. Proc. 428 (New York: AIP)
- [83] Kippen, R.M., *et al.*, 1996, in: in Kouveliotou, C. Briggs M.S. & G.J. Fishman Eds. *Gamma-Ray Bursts 3rd Huntsville Symposium*, AIP Conf. Proc. 384, (New York: AIP).
- [84] Band, D.L., *et al.*, 1993, *Ap. J.*, **413**, 281.
- [85] Schaefer, B., E., *et al.*, 1992, in: in Fishman, G. J., & Brainerd, J. J., Eds., *Gamma-Ray Bursts 2nd Huntsville Symposium* AIP Conf. Proc. 307 (New York: AIP).
- [86] Greiner, J., *et al.*, 1994, *A&A*, **302**, 1216.
- [87] Schaefer, B., E., *et al.*, 1998, *Ap. J.*, **492**, 696.
- [88] Mallozi, R.S., *et al.*, 1995, *Ap. J.*, **454**, 597.
- [89] Cohen, E., Narayan, R., & Piran, T., 1998, *Ap. J.*, **500**, 888, *astro-ph*/9710064.
- [90] Piran, T., & Narayan, R., 1995, in: *Gamma-Ray Bursts, 3rd Huntsville Symposium*, Kouveliotou, C., Briggs, M.S., & Fishman, G.J., Eds., AIP Conf. Proc. 384, (New York: AIP).
- [91] Petrosian, V., & Llyods, N., 1997, in: in C. Meegan, R. Preece & T. Koshut, Eds., *Gamma-Ray Bursts 4th Huntsville Symposium* AIP Conf. Proc. 428 (New York: AIP)
- [92] Lingenfelter, R., & Higdon, J., 1997, in: in C. Meegan, R. Preece & T. Koshut, Eds., *Gamma-Ray Bursts 4th Huntsville Symposium*

AIP Conf. Proc. 428 (New York: AIP)

[93] Harris, M., in: in C. Meegan, R. Preece & T. Koshut, Eds., *Gamma-Ray Bursts 4th Huntsville Symposium* AIP Conf. Proc. 428 (New York: AIP)

[94] Imamura, J.N., & Epstein, R.I., 1987, Ap. J., **313**, 711.

[95] Cohen, E., et al., 1997, Ap. J., **480**, 330.

[96] Preece, R.D., et al., 1997, in: in C. Meegan, R. Preece & T. Koshut, Eds., *Gamma-Ray Bursts 4th Huntsville Symposium* AIP Conf. Proc. 428 (New York: AIP)

[97] Golenetskii, S.V., et al., 1983, Nature **306**, 451.

[98] Mitrofanov, I.G. et al., 1984, Soviet Astron., **28**, 547.

[99] Norris, J.P., et al., 1986, Ap. J., **301**, 213.

[100] Band, D., et al., 1991, in: in W. S. Paciesas, & G. J. Fishman Eds., *Gamma-Ray Bursts* AIP Conf. Proc. 265, (New York: AIP)

[101] Ford L.A., et al., 1995, Ap. J., **439**, 307.

[102] Fenimore, E.E., et al., 1995, Ap. J. Lett., **448**, L101.

[103] Sari, R., Narayan, R., & Piran, T., 1996, Ap. J., **473**, 204.

[104] Murakami, T., et al., 1988, Nature, **335**, 234.

[105] Fenimore, E.E., et al., 1988, Ap. J. Lett., **335**, L71.

[106] Mazets, E., et al., 1980, Sov. Astron. Lett., **6**, 372.

[107] Palmer, D.M., et al., 1994, Ap. J. Lett., **433**, L77.

[108] Band, D.L., et al., 1996, Ap. J., **458**, 746.

[109] Band, D.L., et al., 1995, Ap. J., **447**, 289.

[110] Mészáros, P., & Rees, M.J., 1993, Ap. J., Lett, in press, astro-ph/9804119.

[111] Pendleton, G.M., et al., 1995, in: in Kouveliotou, C. Briggs M.S. & G.J. Fishman Eds. *Gamma-Ray Bursts 3rd Huntsville Symposium*, AIP Conf. Proc. 384, (New York: AIP).

[112] Graziani, C., 1995, in: in Kouveliotou, C. Briggs M.S. & G.J. Fishman Eds. *Gamma-Ray Bursts 3rd Huntsville Symposium*, AIP Conf. Proc. 384, (New York: AIP).

[113] Briggs, M., 1997, in: in C. Meegan, R. Preece & T. Koshut, Eds., *Gamma-Ray Bursts 4th Huntsville Symposium* AIP Conf. Proc. 428 (New York: AIP)

[114] Hurley, K., et al., 1993, A&A Supp., **97**, 39.

[115] Cline, T.L., 1975, Ann. N.Y. Acad. Sci., **262**, 159.

[116] Van Den Bergh, S., 1983, A&SS, **97**, 385.

[117] Schaefer, B.R., 1992, in: in Fishman, G. J., & Brainerd, J. J., Eds., *Gamma-Ray Bursts 2nd Huntsville Symposium* AIP Conf. Proc. 307 (New York: AIP).

[118] Vrba, F.J., in: in Kouveliotou, C. Briggs M.S. & G.J. Fishman Eds. *Gamma-Ray Bursts 3rd Huntsville Symposium*, AIP Conf. Proc. 384, (New York: AIP).

[119] Schaefer, B.R., et al., 1987, Ap. J., **313**, 226.

[120] Schaefer, B.R., et al., 1989, Ap. J., **340**, 455.

[121] Schaefer, B.R., 1990, Ap. J., **364**, 590.

[122] Vrba, F.J., Hartmann, D.H., & Jennings, M.C., 1995, Ap. J., **446**, 115.

[123] Luginbuhl, C.B., et al., 1995, A&SS, **231**, 289.

[124] Larson, S.B., McLean, I.S., & Becklin, E.E., Ap. J. Lett., **460**, L95.

[125] Larson, S.B., & McLean, I.S., 1997, Ap. J. Lett., **491**, 93L.

[126] Schaefer, B.R., et al., 1997, Ap. J., **489**, 636.

[127] Band, D., & Hartmann, D.H., 1998, Ap. J., **493**, 555.

[128] Hogg, D. W., & Fruchter, A. S., 1998, astro-ph/9807262.

[129] Djorgovski, S. G., 1998, astro-ph/9808188.

[130] Bloom, J., S., et al., 1998, astro-ph/9807315.

[131] Fruchter, A., et al., 1998, astro-ph/9807295.

[132] Piro, L., Sacrsi, L., & Butler, R., 1995, Proc. SPIE, **2517**, 169, 686.

[133] Sahu, K., et al., 1997, Nature **387**, 476.

[134] Lamb, D., 1997, in: in C. Meegan, R. Preece & T. Koshut, Eds., *Gamma-Ray Bursts 4th Huntsville Symposium* AIP Conf. Proc. 428 (New York: AIP)

[135] Frontera, F., et al., 1997, preprint, astro-ph/9711279.

[136] Frontera, F., et al., 1997, IAU Circ. 6637.

[137] Murakami, T., et al., 1997, in: in C. Meegan, R. Preece & T. Koshut, Eds., *Gamma-Ray Bursts 4th Huntsville Symposium* AIP Conf. Proc. 428 (New York: AIP)

[138] Galama, T.J., et al., 1997, Nature, **387**, 497.

[139] Fruchter, A., et al., 1997, IAU Circ. 6747.

[140] Frail, D.A., & Kulkarni, S., 1997, private communication.

[141] Kouveliotou, C., et al., 1997, IAU Circ. No. 6660.

[142] Piro, L., 1997, IAU Circ. No. 6656.

[143] Djorgovski, S.G., et al., IAU Circ. No 6655.

[144] Djorgovski, S.G., et al., IAU Circ. No 6658.

[145] Djorgovski, S.G., et al., IAU Circ. No 6660.

[146] Mignoli, M., et al., IAU Circ. No 6661.

[147] Chevalier, C., & Illovaiky, S.A., 1997, IAU Circ. No 6663.

[148] Taylor, G., et al., 1997, Nature, **389**, 263.

[149] Pian, E. et al., 1998, Ap. J. Lett., **492**, 103.

[150] Natarajan, P. et al., 1997, New Astronomy, **2**, 471.

[151] Galama, T.J., et al., 1998, Ap. J. Lett., **497**, L13.

[152] Castro-Tirado, A.J., et al., 1998, Science, **387**, 1011.

[153] Pedersen, H., et al., 1998, Ap. J., **496**, 311.

[154] Sokolov, V.V., et al., 1997, in: in C. Meegan, R. Preece & T. Koshut, Eds., *Gamma-Ray Bursts 4th Huntsville Symposium* AIP Conf. Proc. 428 (New York: AIP)

[155] Bloom, J.S., 1998, GCN Note #30.

[156] Castro-Tirado, A.J., et al., 1998 IAU Circ. 6848.

[157] Sokolov, V.V., et al., 1998 A&A **334**, 117.

[158] Goodman, J., 1997, New Astronomy, **2**, 449.

[159] Remillard, R.A., et al., 1997, IAU Circ. 6726.

[160] Smith, D., et al., 1997, IAU Circ. 6728.

[161] Groot, P.J., et al., 1998, Ap. J. Lett., **493**, L27, astro-ph/9711171.

[162] Heise, J., et al., 1997, IAU Circ. 6787.

[163] Halpern, J., et al., 1997, IAU Circ. 6788.

[164] Meegan, C., et al., 1998, BATSE catalogue, <http://www.batse.msfc.nasa.gov/data/grb/catalog/>.

[165] Galama, T. J., et al., 1998, submitted to Nature, astro-ph/9806175.

[166] Kippen, R. M., et al. 1998, GCN Circ. no. 143.

[167] Quashnock, J., & Lamb, D., 1993, MNRAS, **265**, L59.

[168] Narayan, R., & Piran, T., 1993, MNRAS, **265**, L65.

[169] Hartmann, D. H., et al., 1994, in: *AIP Conference Proceedings, Gamma-Ray Bursts, Second Workshop, Huntsville, Alabama, 1993*, **307**, Fishman, G.J., Brainerd, J.J., & Hurley, K., Eds. (New York: AIP).

[170] Meegan, C.A., et al., 1995, Ap. J., **434**, 552.

[171] Tegmark, M., et al., 1996, Ap. J., **466**, 757.

[172] Hartmann, D.H., & Blumenthal, G.R., 1989, Ap. J., **342**, 521.

[173] Kollat, T., & Piran, T., 1996, Ap. J. Lett., **467**, 41L.

[174] Kompaneetz, D., & Stern, B., 1997 in: in C. Meegan, R. Preece & T. Koshut, Eds., *Gamma-Ray Bursts 4th Huntsville Symposium* AIP Conf. Proc. 428 (New York: AIP)

[175] Hurley, K., et al., 1997, Ap. J. Lett., **479**, 113.

[176] Schartel, N., Andernach, H., & Greiner, J., 1997, A&A, **323**, 659.

[177] Schmidt, M., Higdon, J.C., & Jueter, G., 1988, Ap. J. Lett., **329**, L85.

[178] Pendleton, G.N., et al., 1995, in preparation (quoted in [39]).

[179] Katz, J.I., 1992, A&SS, **197**, 163.

[180] Hartmann, D.H., et al., 1995, A&SS, **231**, 361.

[181] Loredo, T.J., & Wassermann, I.M., 1995, Ap. J. Supp., **96**, 59.

[182] Loredo, T.J., & Wassermann, I.M., 1995, Ap. J. Supp., **96**, 261.

[183] Cohen, E., & Piran, T., 1995, Ap. J., **444**, L25.

[184] Weinberg, S., 1972, *General Relativity & Cosmology*, Wiley.

[185] Rutledge, R.E., Hui, L., Lewin, W.H.G., 1995, MNRAS, **276**, 753.

[186] Horack, J.M., & Emslie, A.G., 1994, Ap. J., **428**, 620.

[187] Mészáros, P. & Mészáros, A., 1995, Ap. J., **449**, 9.

[188] Mészáros, A. & Mészáros, P., 1996, Ap. J., **466**, 29.

[189] Horváth, I., Mészáros, P. & Mészáros, A., 1996, Ap. J., **470**, 56.

[190] Reichart, D.E. & Mészáros, P., 1997, Ap. J., **483**, 597.

[191] Cohen, E., & Piran, T., 1996, in: *Gamma-Ray Bursts, Huntsville, Alabama, 1995*, Kouveliotou, C., Briggs, M.S., & Fishman, G.J., Eds. (New York: AIP).

[192] Kirshner, R.P., et al., 1983, Ap. J., **88**, 1285.

[193] Totani, T., 1997, Ap. J. Lett., **486**, 71.

[194] Sahu, K., et al., 1997, Ap. J. Lett., **489**, L127.

[195] Wijers, R.A.M.J., et al., 1998, MNRAS, **294**, 13.

[196] Lilly, S.J., et al., 1996, Ap. J. Lett., **460**, L1.

[197] Madau, P., et al., 1996, MNRAS, **283**, 1388.

[198] Connolly, A.J., et al., Ap. J. Lett., **486**, L11.

[199] Krumholz, M., Thorsett, S. E., & Harrison, F., A., 1998, astro-ph/9807117.

[200] Fenimore, E.E., et al., 1993, Nature, **366**, 40.

[201] Cohen, E., & Piran, T., 1997, Ap. J. Lett., **488**, L7.

[202] Nemiroff, R.J., et al., 1994, Ap. J., **423**, 432.

[203] Norris, J.P., et al., 1995, Ap. J., **439**, 542.

[204] Fenimore, E.E. & Bloom, J.S., 1995, **453**, 25.

[205] Ruderman, M., 1975, Ann. N.Y. Acad. Sci., **262**, 164.

[206] Schmidt, W.K.H., 1978, Nature, **271**, 525.

[207] Guilbert, P.W., Fabian, A.C., & Rees, M.J., 1983, MNRAS, **205**, 593.

[208] Carigan, B.J., & Katz, J.I., 1992, Ap. J., **399**, 100.

[209] Piran, T., & Shemi, A., 1993, Ap. J. Lett., **403**, L67.

[210] Fenimore, E.E., Epstein, R.I., & Ho, C.H., 1993, A&A Supp., **97**, 59.

[211] Woods, E., & Loeb, A., 1995, Ap. J., **383**, 292.

[212] Baring, M., G., & Harding, A., K., 1997, Ap. J. **491**, 663.

[213] Loeb, A., 1993, Phys. Rev., **D48**, 3419.

[214] Woltjer, L., 1966, Ap. J. Lett., **146**, 597.

[215] Rees, M. J., 1967, MNRAS, **135**, 345.

[216] Mirabel, I.F., & Rodriguez, L.F., 1995, Nature, **371**, 46.

[217] Goodman, J., 1986, Ap. J., **308**, L47.

[218] Krolik, J.H., & Pier, E.A., 1991, Ap. J., **373**, 277.

[219] Mészáros, P., & Rees, M.J., 1993, Ap. J., **405**, 278.

[220] Shemi, A., & Piran, T., 1990, Ap. J., **365**, L55.

[221] Paczyński, B., 1990, Ap. J., **363**, 218.

[222] Piran, T., 1994, in: AIP Conference Proceedings **307**, *Gamma-Ray Bursts, Second Workshop, Huntsville, Alabama, 1993*, Fishman, G.J., Brainerd, J.J., & Hurley, K., Eds., (New York: AIP), p. 495.

[223] Narayan, R., & Piran, T., 1995, in preparation.

[224] Thompson, C., 1994, MNRAS, **270**, 480.

[225] Usov, V.V., 1994, MNRAS, **267**, 1035.

[226] Usov, V.V., & Smolsky, M.V., 1996, Ap. J., **461**, 858.

[227] Mesz, P. & Rees, M.J., 1997, Ap. J. Lett., **482**, L89.

[228] Kobayashi, S., Piran, T., & Sari, R., 1998, astro-ph/9803217.

[229] Piran, T., Shemi, A., & Narayan, R., 1993, MNRAS, **263**, 861.

[230] Fenimore, E.E., Madras, C., & Nayakshin, S., 1996, Ap. J., **473**, 998.

[231] Fenimore, E.E., *et al.*, 1998, astro-ph/9802200.

[232] Sari, R., & Piran, T., 1997, MNRAS, **287**, 110.

[233] Sari, R., & Piran, T., 1995, Ap. J. Lett., **455**, 143.

[234] Shemi, A., 1994, MNRAS, **269**, 1112.

[235] Shaviv, N., & Dar, A., 1995, MNRAS, **277**, 287.

[236] Mészáros, P., 1995, in: *The 17th Texas Symposium on Relativistic Astrophysics and Cosmology*.

[237] Kobayashi, S., Sari, R., & Piran, T., 1997, Ap. J., **490**, 92.

[238] Blandford, R.D., & McKee, C.F. 1976, Phys. of Fluids, **19**, 1130.

[239] Blandford, R.D., & McKee, C.F. 1976, MNRAS, **180**, 343.

[240] Mészáros, P., Laguna, P., & Rees, M.J., 1993, Ap. J., **415**, 181.

[241] Schaefer, B.R., *et al.*, 1997, Ap. J., **492**, 696.

[242] Usov, V.V., & Smolsky, M.V., 1998, Phys. Rev., **E57**, 2267.

[243] Kirk, J.G., 1994, in: *it Plasma Astrophysics*, Benz, A.O., & Courvoisier, T.J.L., Eds., Springer-Verlag (New York).

[244] Hillas, A.M., 1984, ARA&A, **22**, 42.

[245] Rybicki, G.B., & Lightman, A.P., 1979, *Radiative Processes in Astrophysics*.

[246] Sari, R., Piran, T., & Narayan, R., 1998, Ap. J. Lett., **497**, L41.

[247] Waxman, E., 1997, Ap. J. Lett., **489**, L33.

[248] Wijers, R.A.M.J., & Galama, T.J. 1998, astro-ph/9805341.

[249] Granot, J., Piran, T., & Sari, R., 1998, astro-ph/9808007.

[250] Pilla, R., & Loeb, A., 1998, Ap. J. Lett., **494**, 167, astro-ph/9710219.

[251] Waxman, E., & Piran, T. 1994, Ap. J., **433**, L85.

[252] Sari, R., & Piran, T., 1997, in: in C. Meegan, R. Preece & T. Koshut, Eds., *Gamma-Ray Bursts 4th Huntsville Symposium* AIP Conf. Proc. 428 (New York: AIP)

[253] Sari, R., 1997, Ap. J. Lett., **489**, 37.

[254] Sari, R., 1998, Ap. J. Lett., **494**, L49.

[255] Waxman, E., 1997, Ap. J. Lett., **491**, L19.

[256] Panaitescu, A., & Mészáros, P., 1998, Ap. J., **492**, 683, astro-ph/9709284.

[257] Cohen, E., Piran, T., & Sari, R., 1998, astro-ph/9803258.

[258] Rhoads, J.E., 1997, Ap. J. Lett., **487**, L1.

[259] Granot, J., Piran, T., & Sari, R., 1998, astro-ph/9806192.

[260] Galama, T.J., *et al.*, 1998, Ap. J. Lett., in press. astro-ph/9804191.

[261] Galama, T.J., *et al.*, 1998, Ap. J. Lett., in press, astro-ph/9804190.

[262] Colgaae, S.A., 1974, Ap. J., **187**, 333.

[263] Perna, R., & Loeb, A., 1998, astro-ph/9810085.

[264] Wang, L., & Wheeler, J. C., 1998, Ap. J. Lett. **584**, 87, Astro-ph/9806212.

[265], Kippen, R. M., *et al.* 1998, astro-ph/9806364.

[266] Bloom, J. S., *et al.* 1998, astro-ph/9807050.

[267] Usov, V.V., 1992, Nature, **357**, 472.

[268] Nemiroff, R.J., 1993, Comm. Ap., **17**, 189.

[269] Belinkov, S.I., Novikov, I.D., & Tsvetkov, D.Yu., 1984, SvAL, **10**, 177.

[270] Goodman, J., Dar, A., & Nussinov, S., 1987, Ap. J. Lett., **314**, L7.

[271] Paczyński, B., 1991, Acta Astronomica, **41**, 257.

[272] Piran, T., Narayan, R., & Shemi, A., 1992, in: AIP Conference Proceedings **265**, *Gamma-Ray Bursts, Huntsville, Alabama, 1991*, Paciesas, W.S., & Fishman, G.J., Eds. (New York: AIP), p. 149.

[273] Woosley, S.E., 1993, Ap. J., **405**, 273.

[274] Carter, B., 1992, Ap. J. Lett., **391**, L67.

[275] Taylor, J.H., & Weisberg, J.M., 1982, Ap. J., **253**, 908.

[276] Davies, M.B., Benz, W., Piran, T., & Thielemann, F.K., 1994, Ap. J., **431**, 742.

[277] Clark, J.P.A., & Eardley, D., 1977, Ap. J., **215**, 311.

[278] Wolszczan, A., 1991, Nature, **350**, 688.

[279] Tutukov, A.V., & Yungelson, L.R., 1994, MNRAS, **268**, 871.

[280] Lipunov, V.M., Postanov, K.A., & Prokhorov, M.E., MNRAS, **288**, 245.

[281] Yungelson, L.R., & Portegies Zwart, S.F., 1998, astro-ph/9801127.

[282] Bethe, H.A., & Brown, G.E., 1998, astro-ph/9802084.

[283] Lyne, A.G. & Lorimer, D.R., 1994, Nature, **369**, 127.

[284] White, N.E., & van Paradijs, J., 1996, Ap. J. Lett., **473**, L25.

[285] Fryer, C., & Kalogera, V., 1997, Ap. J. in press.

[286] Cordes, J.M., & Chernoff, D.F., 1997, astro-ph/9707308.

[287] Jaroszynski, M., 1993, Acta Astronomica, **43**, 183.

[288] Jaroszynski, M., 1996, A&A, **305**, 839.

[289] Ruffert, M., & Janka, H.-T., 1996, A&A, **307**, L33.

[290] Ruffert, M., Janka, H.-T., & Schaefer, G., A&A, **311**, 532.

[291] Ruffert, M., Janka, H.-T., Takahashi, K., & Schaefer, G., A&A, **319**, 122.

[292] Wilson, J.R., Mathews, G.J., & Marronetti, P., 1996, Phys. Rev., **D54**, 1317.

[293] Mathews, G.J., *et al.*, 1997, in: in C. Meegan, R. Preece & T. Koshut, Eds., *Gamma-Ray Bursts 4th Huntsville Symposium* AIP Conf. Proc. 428 (New York: AIP)

[294] Waxman, E., 1995, Ap. J. Lett., **452**, 1.

[295] Vietri, M., 1995, Ap. J., **453**, 883.

[296] Milgrom, M., & Usov, V. 1995, Ap. J. Lett., **449**, L37.

[297] Waxman, E., & Bahcall, J. N., 1997, Phys. Rev. Lett., **78**, 2292.

[298] Waxman, E., 1995 Phys. Rev. Lett., **75**, 386.

[299] Abramovichi, A., *et al.*, 1992, Science, **256**, 325.

[300] Bardachia, C., *et al.*, 1990, Nucl. Inst. A., **289**, 518.

[301] Kochaneck, C., & Piran, T., 1993, Ap. J. Lett., **417**, L17.

[302] Mao, S., & Paczyński, B. 1992, Ap. J. Lett., **388**, L45.

[303] Dermer, C., D., 1992, Phys. Rev. Lett., **68**, 1799.

[304] Wickramasinghe, W.A.D.T., *et al.*, 1993, Ap. J. Lett., **411**, L55.

[305] Zdziarski, A.A., & Svensson, R., 1989, Ap. J., **344**, 551.

[306] Livio, M., *et al.*, 1997, in: in C. Meegan, R. Preece & T. Koshut, Eds., *Gamma-Ray Bursts 4th Huntsville Symposium* AIP Conf. Proc. 428 (New York: AIP)

[307] Lamb, D.Q., & Quashnock, J.M., 1993, Ap. J. Lett., **415**, L1.

[308] Tegmark, M., Hartmann, D.H., Briggs, M.S., & Meegan, C.A., 1995, Ap. J., **486**, 214.

[309] Mao, S., 1992, Ap. J. Lett., **389**, L41.

[310] Nemiroff, R.J., *et al.*, 1994, Ap. J., **432**, 478.

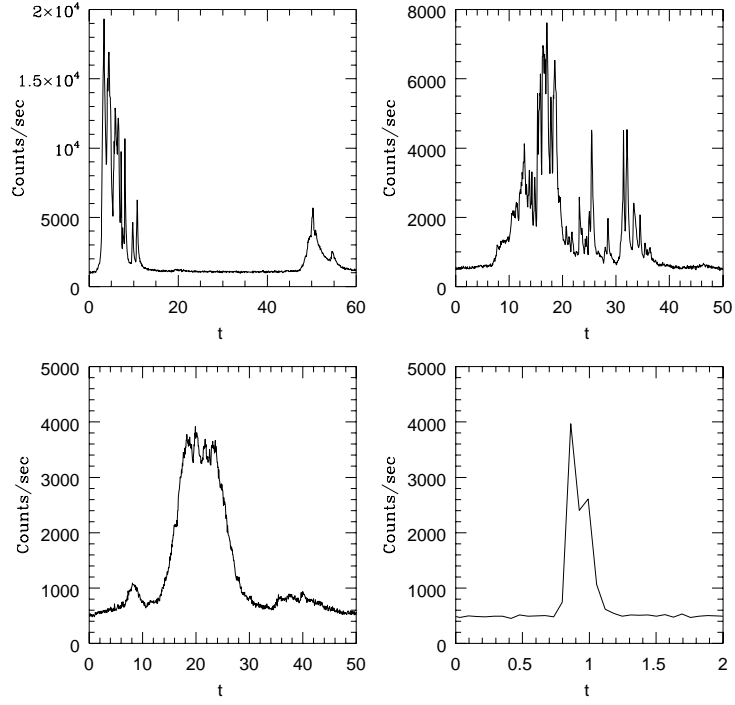


Fig. 1.— Total number of counts vs. time for several bursts from the BATSE Catalogue. Note the large diversity of temporal structure observed.

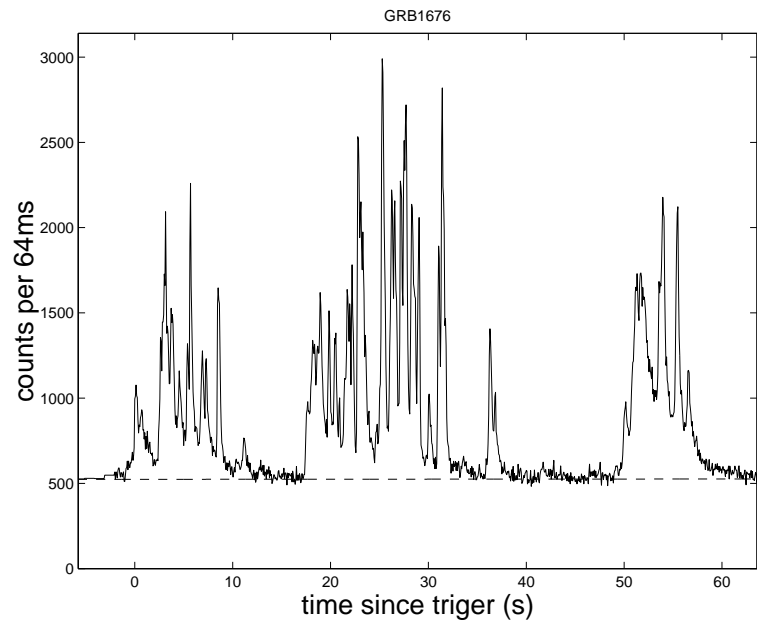


Fig. 2.— Counts vs. time for BATSE burst 1676. The bursts lasted  $T \sim 60$  sec and it had peaks of width  $\delta T \sim 1$  sec, leading to  $\mathcal{N} \approx 60$ .

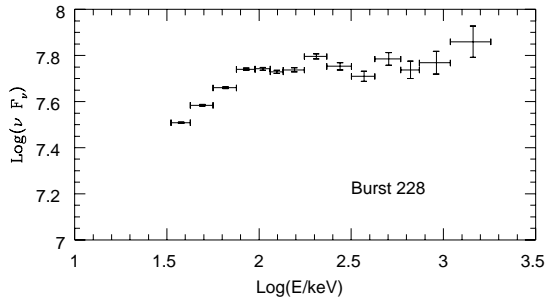


Fig. 3.— *Observed spectrum of BATSE's burst 228.*

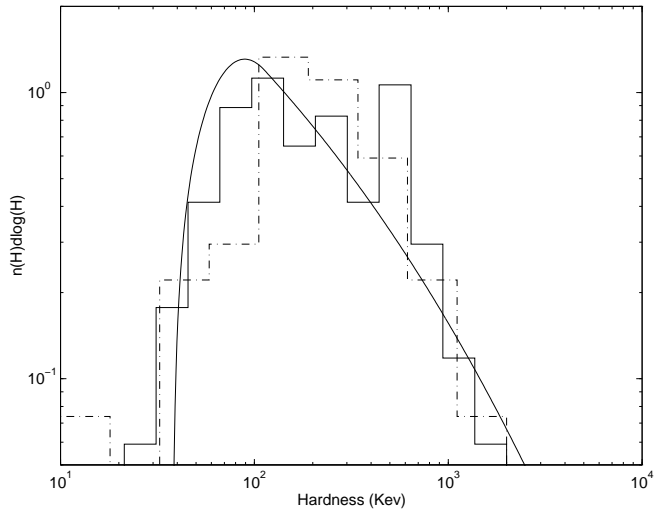


Fig. 4.—  $N(H)$  - the number of bursts with hardness ,  $H$ , in the Band et al. [84] sample (dashed-dotted line) and in the Cohen et al. sample (solid line) [89] together with a theoretical fit of a distribution above  $H = 120\text{KeV}$  with  $\gamma \sim -0.5$  (a slowly decreasing numbers of GRBs per decade of hardness)

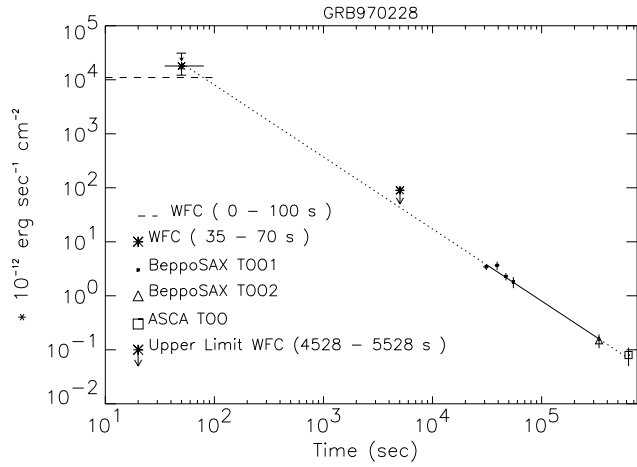


Fig. 5.— Decay of the X-ray afterglow from GRB970228, from [10]. Shown is source flux at the 2-10KeV range. The data is fitted with a power law  $t^{-1.32}$ .

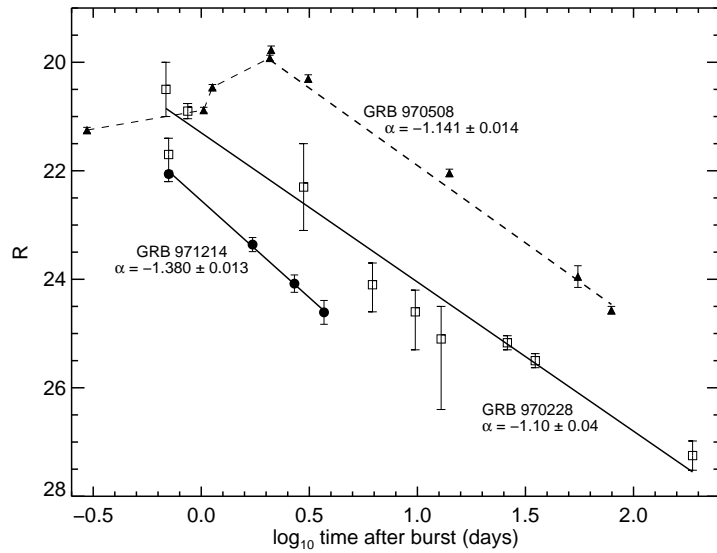


Fig. 6.— Decay of the optical afterglow in GRB070228, GRB9700508 and GRB971214. A clear power law decay can be seen in all cases.

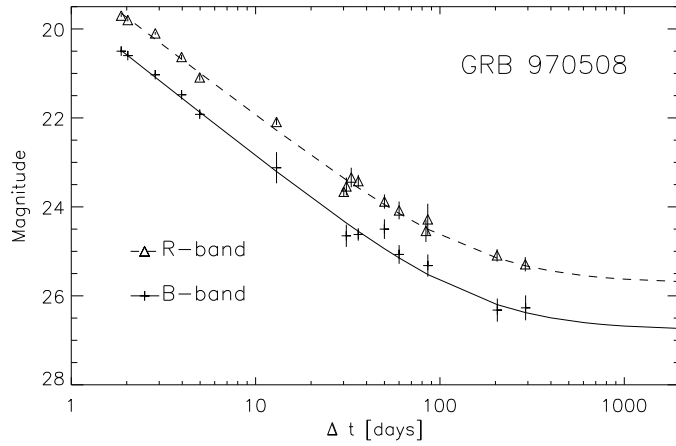


Fig. 7.— Decay of the optical afterglow in , GRB9700508. A clear transition from a power law decay to a constant can be seen (from [130].

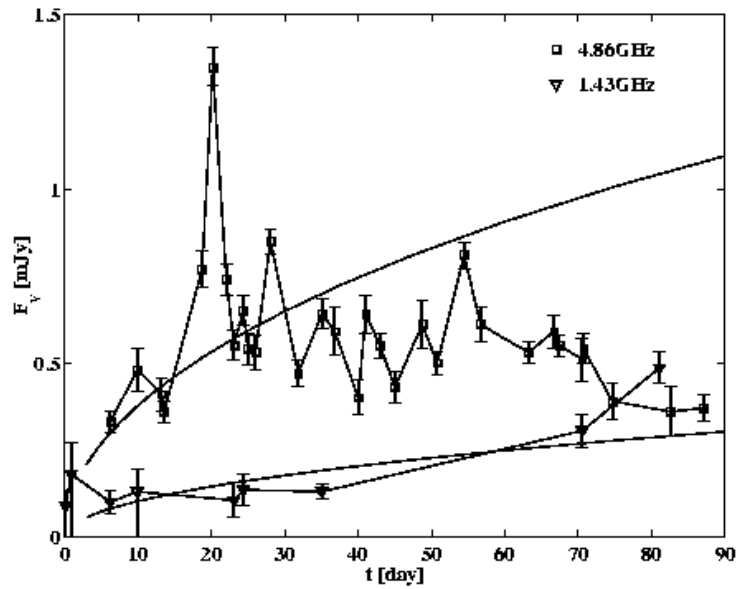


Fig. 8.— Light curve of the radio afterglow from GRB970508, from [13]

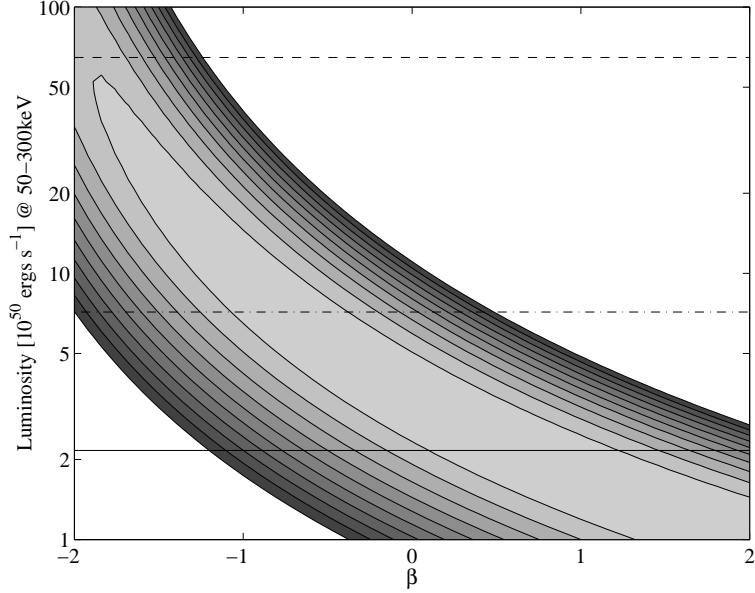


Fig. 9.— The likelihood function (levels 33%, 10%, 3.3%, 1% etc..) in the  $(\beta, L)$  plane for standard candles  $\alpha = 1.5$ ,  $\Omega = 1$ , and evolution given by  $\rho(z) = (1+z)^{-\beta}$ . Superimposed on this map is the luminosity of GRB970508, (solid curve), GRB971214 (dashed curve) and GRB980703 (dashed-dotted curve). We have used  $h_{75} = 1$ .

From [201].

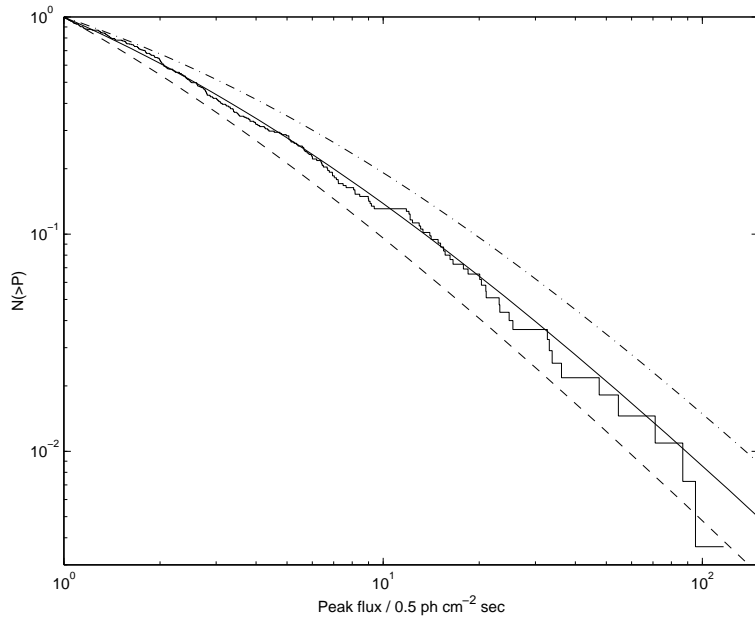


Fig. 10.— The observed long burst peak flux distribution and three theoretical cosmological distributions with  $\Omega = 1$ ,  $\Lambda = 0$ ,  $\alpha = -1.5$ , standard candles and no source evolution:  $L = 3.4 \cdot 10^{50} \text{ ergs/sec}$  (solid line: best fit),  $L = 7.2 \cdot 10^{50} \text{ ergs/sec}$  (dashed line: lower 1% bound),  $L = 1.4 \cdot 10^{50} \text{ ergs/sec}$  (dashed-dotted line: upper 1% bound)

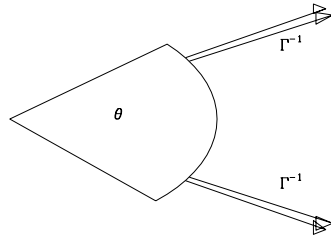


Fig. 11.— Radiation from a relativistic beam with a width  $\theta$ . Each observer will detect radiation only from a very narrow beam with a width  $\Gamma^{-1}$ . The overall angular size of the observed phenomenon can vary, however, with  $\Gamma^{-2} < \theta^2 < 4\pi$ .

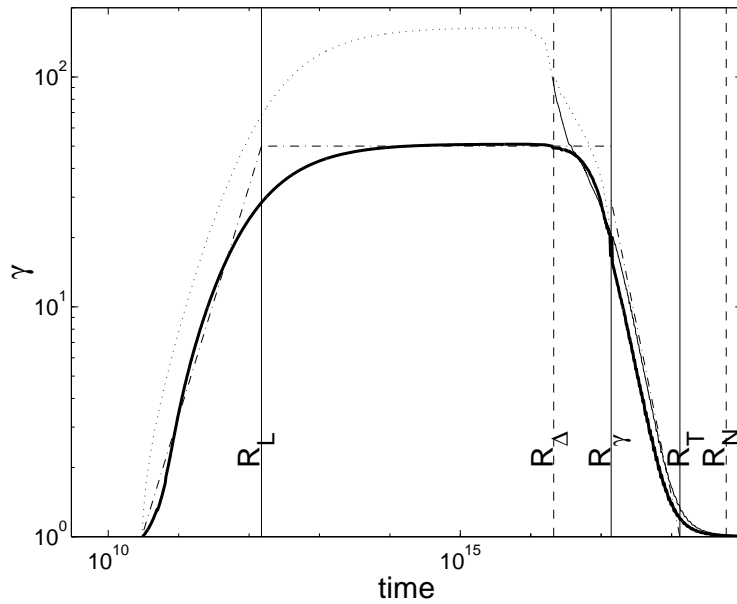


Fig. 12.— Fireball evolution from its initial formation at rest to the final Newtonian Sedov solution. The energy extraction is due to the interaction with the ISM via a relativistic forward shock and a Newtonian reverse shock. We have used for this calculations  $\xi = 43$ ,  $E_0 = 10^{52}$  [erg],  $\gamma_0 = 50$ ,  $R_0 = 3 \times 10^{10}$  [cm]. Shown are the average value of the Lorentz factor (thick solid line), the value at the forward shock (thin solid line), the maximal value (dotted line) and an analytic estimate (dashed dotted line). From [228].

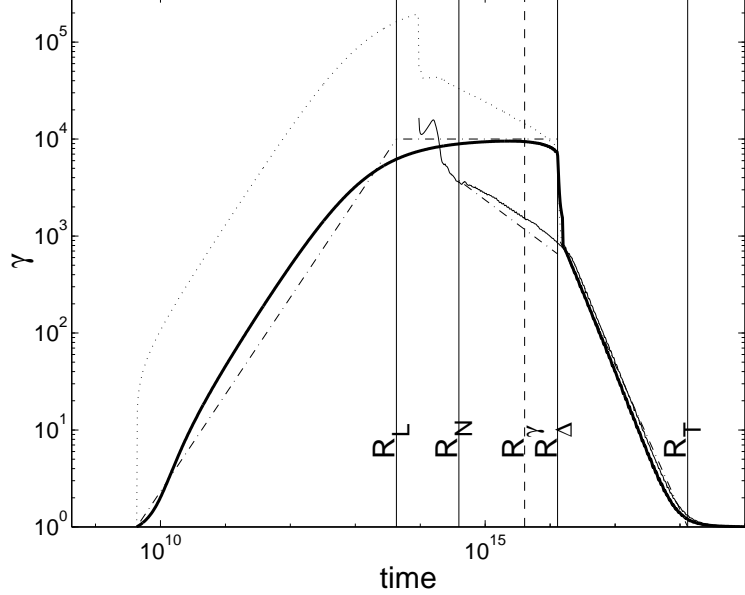


Fig. 13.— Fireball evolution from its initial formation at rest to the final Newtonian Sedov solution. The energy extraction is due to the interaction with the ISM via relativistic forward and reverse shocks. The parameters for this computation are:  $\xi = 0.1$ ,  $E_0 = 10^{52}[\text{erg}]$ ,  $\gamma_0 = 10^4$ ,  $R_0 = 4.3 \times 10^9[\text{cm}]$ . Shown are the average value of the Lorentz factor (thick solid line), the value at the forward shock (thin solid line), the maximal value (dotted line) and an analytic estimate (dashed dotted line). From [228].

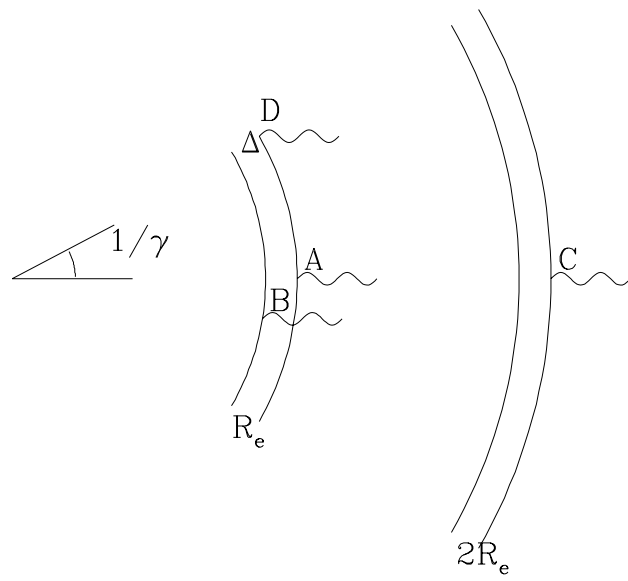


Fig. 14.— Different time scales in terms of the arrival time of four photons:  $t_A, t_B, t_C$ , and  $t_D$ .  $T_{\text{radial}} = t_C - t_A$ ;  $T_{\text{angular}} = t_D - t_A$ ,  $\Delta/c = t_B - t_A$ .

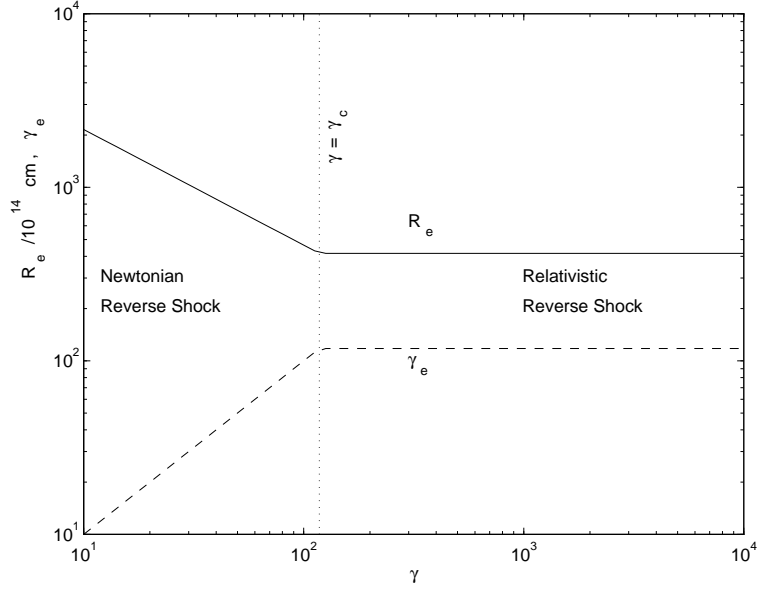


Fig. 15.— The deceleration radius  $R_e$  and the Lorentz factor of the shocked shell  $\gamma_e$  as functions of the initial Lorentz factor  $\gamma$ , for a shell of fixed width  $\Delta = 3 \times 10^{12}$  cm. For low values of  $\gamma$ , the shocked material moves with Lorentz factor  $\gamma_e \sim \gamma$ . However as  $\gamma$  increases the reverse shock becomes relativistic reducing significantly the Lorentz factor  $\gamma_e < \gamma$ . This phenomena prevents the “external shock model” from being Type-II.



Fig. 16.— A very narrow jet of angular size considerably smaller than  $\gamma_e^{-1}$ , for which the angular spreading problem does not exist. The duration of the burst is determined by the deceleration distance  $\Delta R_e$ , while the angular time is assumed small. The variability could now be explained by either variability in the source which leads to a pulsed jet (a) or by a uniform jet interacting with an irregular ISM (b)

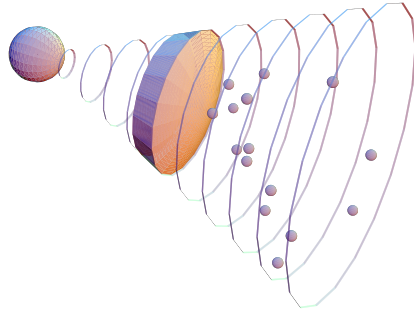


Fig. 17.— A shell with angular size  $\gamma^{-1}$  (the angular size is highly exaggerated). The spherical symmetry is broken by the presence of bubbles in the ISM. The relative angular size of the shell and the bubbles is drawn to scale assuming that a burst with  $N = 15$  is to be produced. Consequently  $N = 15$  bubbles are drawn (more bubbles will add up to a smooth profile). The fraction of the shell that will impact these bubbles is small leading to high inefficiency. As  $N$  increases the efficiency problem becomes more severe  $\sim N^{-1}$ , from [20]

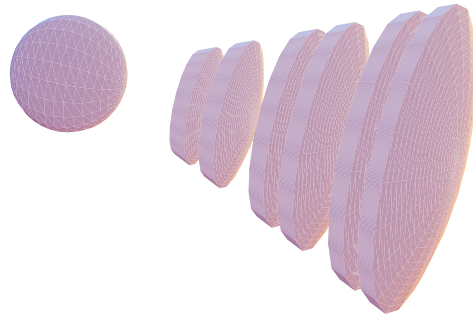


Fig. 18.— *The internal shock scenario. The source produces multiple shells as shown in this figures. The shells will have different Lorentz factors. Faster shells will catch up with slower ones and will collide, converting some of their kinetic energy to internal energy. This model is Type-II and naturally produces variable bursts. from [20]*

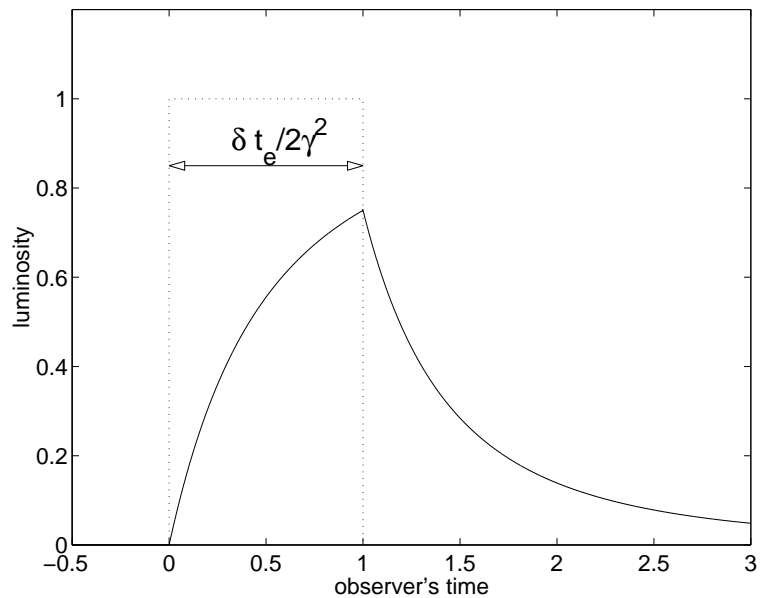


Fig. 19.— A peak produced by a collision between two shells. The luminosity plotted versus the arrival time. The solid line corresponds to  $R = c\delta t_e$  and the dotted line corresponds to  $R = 0$ , from [33]

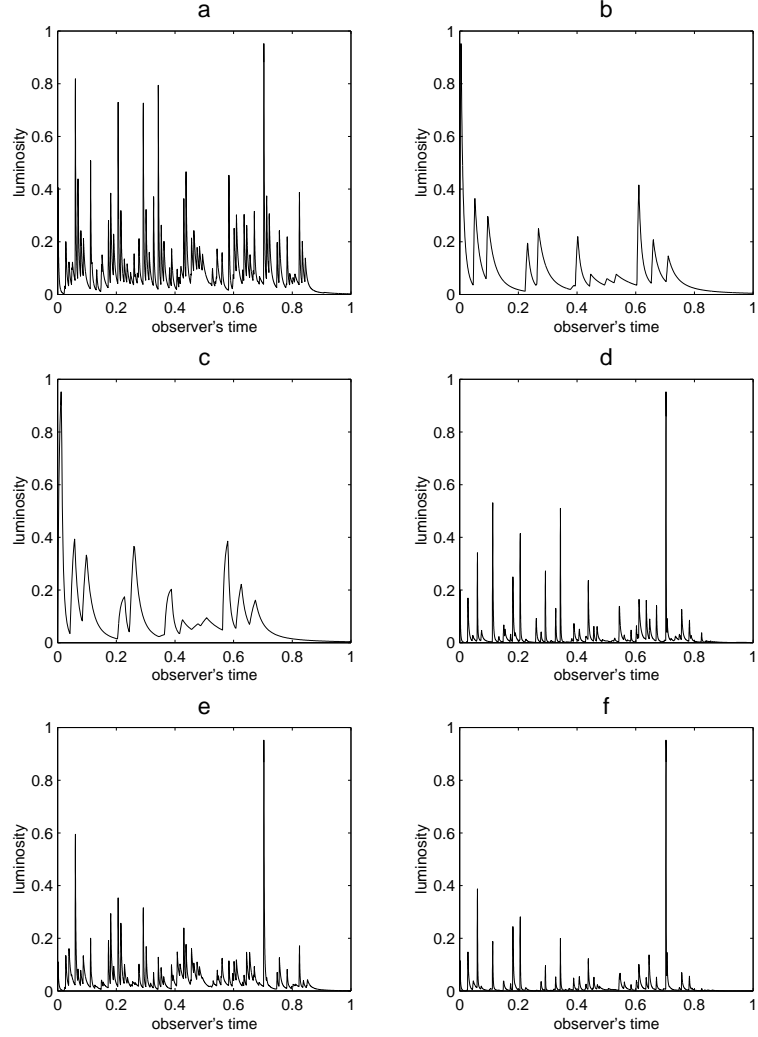


Fig. 20.— *Luminosity vs. observer time, for different synthetic models* a:  $\gamma_{min} = 100$ ,  $\gamma_{max} = 1000$ ,  $N = 100$ ,  $\eta = -1$  and  $L/l = 5$  b:  $\gamma_{min} = 100$ ,  $\gamma_{max} = 1000$ ,  $N = 100$ ,  $\eta = 1$  and  $L/l = 5$  c:  $\gamma_{min} = 100$ ,  $\gamma_{max} = 1000$ ,  $N = 20$ ,  $\eta = -1$  and  $L/l = 5$  d:  $\gamma_{min} = 100$ ,  $\gamma_{max} = 1000$ ,  $N = 20$ ,  $\eta = -1$  and  $L/l = 1$  e:  $\gamma_{min} = 100$ ,  $\gamma_{max} = 1000$ ,  $N = 100$ , random energy with  $E_{max} = 1000$  and  $L/l = 5$  f:  $\gamma_{min} = 100$ ,  $\gamma_{max} = 1000$ ,  $N = 100$ , random density with  $\rho_{max} = 1000$  and  $L/l = 5$ . From [33].

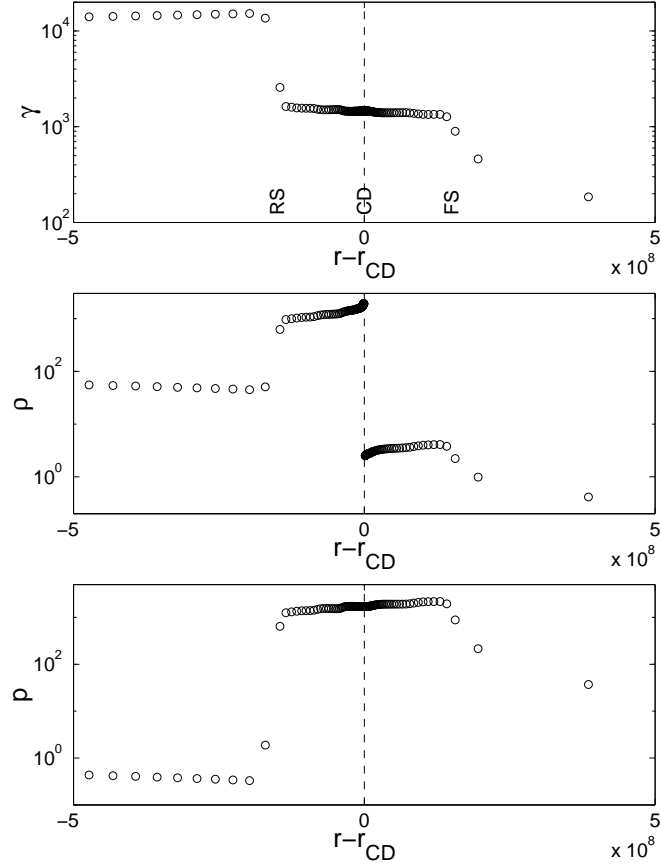


Fig. 21.— The Lorentz factor  $\gamma$ , the density  $\rho$  and the pressure  $p$  in the shocks. There are four regions: the ISM (region 1), the shocked ISM (region 2), the shocked shell (region 3) and the unshocked shell (region 4), which are separated by the forward shock (FS), the contact discontinuity (CD) and the reverse shock (RS). The initial parameters are the same as in 13. From [228].

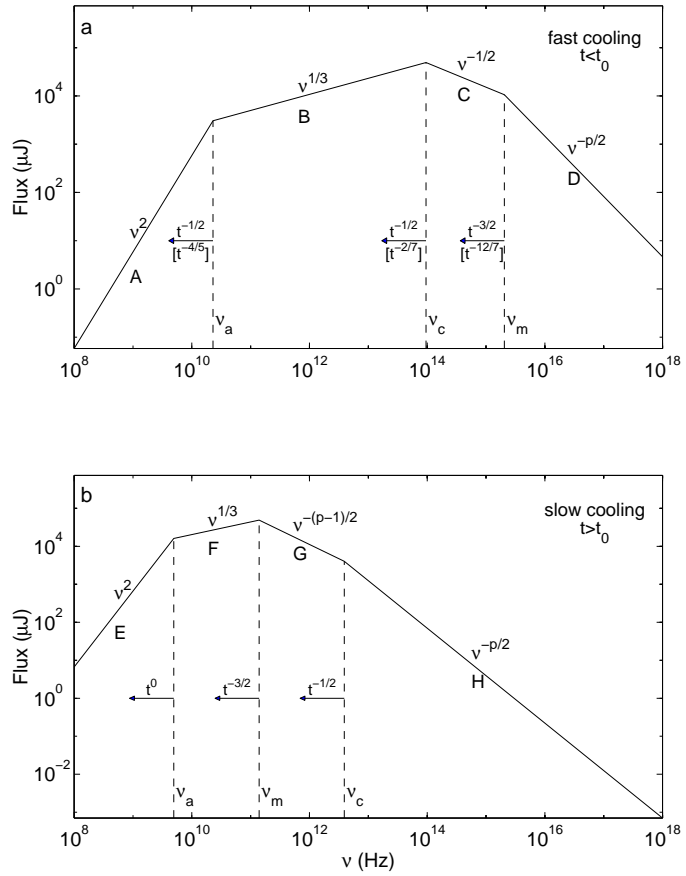


Fig. 22.— Synchrotron spectrum of a relativistic shock with a power-law electron distribution. (a) Fast cooling, which is expected at early times ( $t < t_0$ ). The spectrum consists of four segments, identified as A, B, C, D. Self-absorption is important below  $\nu_a$ . The frequencies,  $\nu_m$ ,  $\nu_c$ ,  $\nu_a$ , decrease with time as indicated; the scalings above the arrows correspond to an adiabatic evolution, and the scalings below, in square brackets, to a fully radiative evolution. (b) Slow cooling, which is expected at late times ( $t > t_0$ ). The evolution is always adiabatic. The four segments are identified as E, F, G, H. From [246].

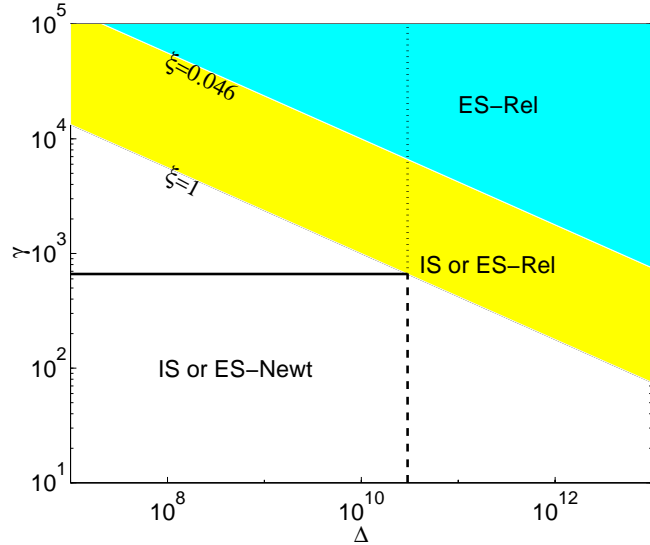


Fig. 23.— Different scenarios in the  $\Delta$  (in cm) -  $\gamma$  plane for  $\zeta \equiv \delta/\Delta = 0.01$ . Relativistic ES occur for large  $\Delta$  and large  $\gamma$  - upper right -above the  $\xi = 1$  line (dark gray and light gray regions). Newtonian ES occur below  $\xi = 1$  - lower left - white region. IS occur, if there are sufficient variation in  $\gamma$  below the  $\xi = \zeta^{2/3}$  line (light gray and white regions). The equal duration  $T = 1$  s curve is shown for Newtonian ES (solid line) a relativistic ES (dotted line) and IS (dashed line). Note that a relativistic ES and an internal shock with the same parameters have the same overall duration  $T$  but different temporal substructure depending on  $\delta$ . From [232].

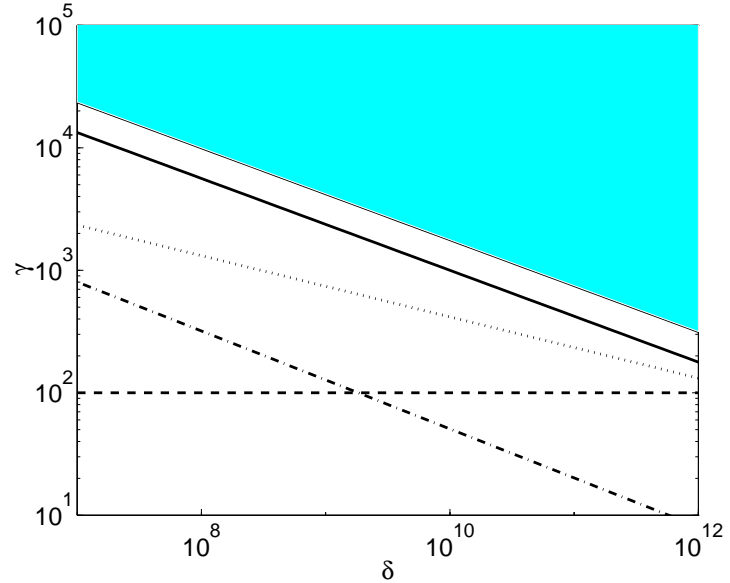


Fig. 24.— Allowed regions for internal shocks in the  $\delta$  (in cm),  $\gamma$  plane. Note that the horizontal  $\delta$  axis also corresponds to the typical peak duration,  $\delta t$  multiplied by  $c$ . Internal shocks are impossible in the upper right (light gray) region. The lower boundary of this region depends on  $\zeta \equiv \delta/\Delta$  and are marked by two solid curves, the lower one for  $\zeta = 1$  and the upper one for  $\zeta = 0.01$ . Also shown are  $\tau_{\gamma\gamma} = 1$  for an observed spectrum with no upper bound (dotted line),  $\tau_{\gamma\gamma} = 1$  for an observed spectrum with an upper bound of 100 MeV (dashed line) and  $\tau_e = 1$  (dashed-dotted). The optically thin internal shock region is above the  $\tau = 1$  curves and below the  $\xi = \zeta^{2/3}$  (solid) lines. From [232].

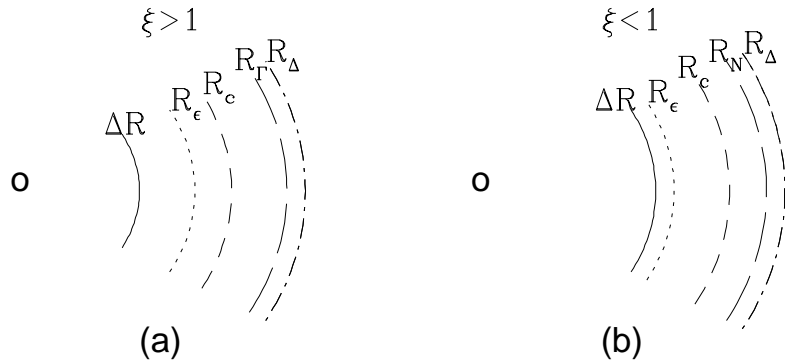


Fig. 25.— (a) Schematic description of the different radii for the case  $\xi > 1$ . The different distances are marked on a logarithmic scale. Beginning from the inside we have  $\Delta R$ , the initial size of the shell,  $R_\epsilon$ , the radius in which a fireball becomes matter-dominated (see the following discussion),  $R_c$ , the radius where inner shells overtake each other and collide,  $R_\Delta$ , where the reverse shock reaches the inner boundary of the shell, and  $R_\Gamma$ , where the kinetic energy of the shell is converted into thermal energy. (b) Same as (a) for  $\xi < 1$ .  $R_\Gamma$  does not appear here since it is not relevant.  $R_N$  marks the place where the reverse shock becomes relativistic. From [31]

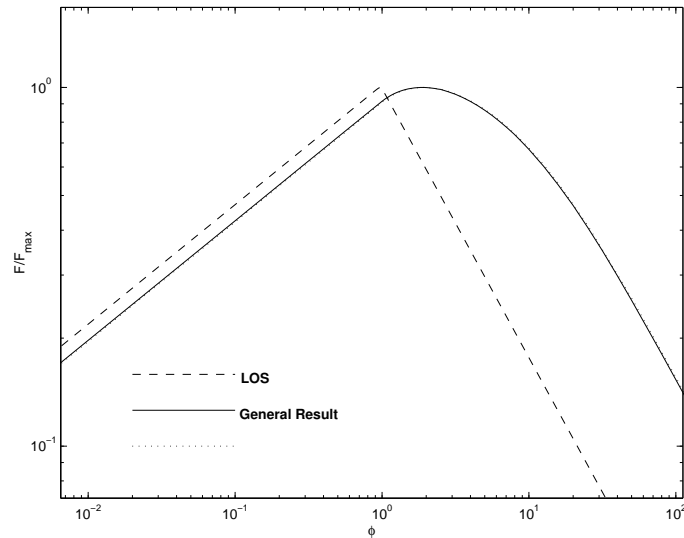


Fig. 26.— Calculated spectra or light curve from a Blandford-McKee solution.  $F_\nu(t)$  is plotted as a function of  $\phi \equiv \text{Const.} \times \nu t^{3/2}$ . Thus if we consider a constant time this figure yields the spectrum while if we consider a fixed frequency it yields the light curve. The solid curve depicts emission from the full fireball. The dashed line depicts the spectrum resulting from emission along the line of sight. From [259].

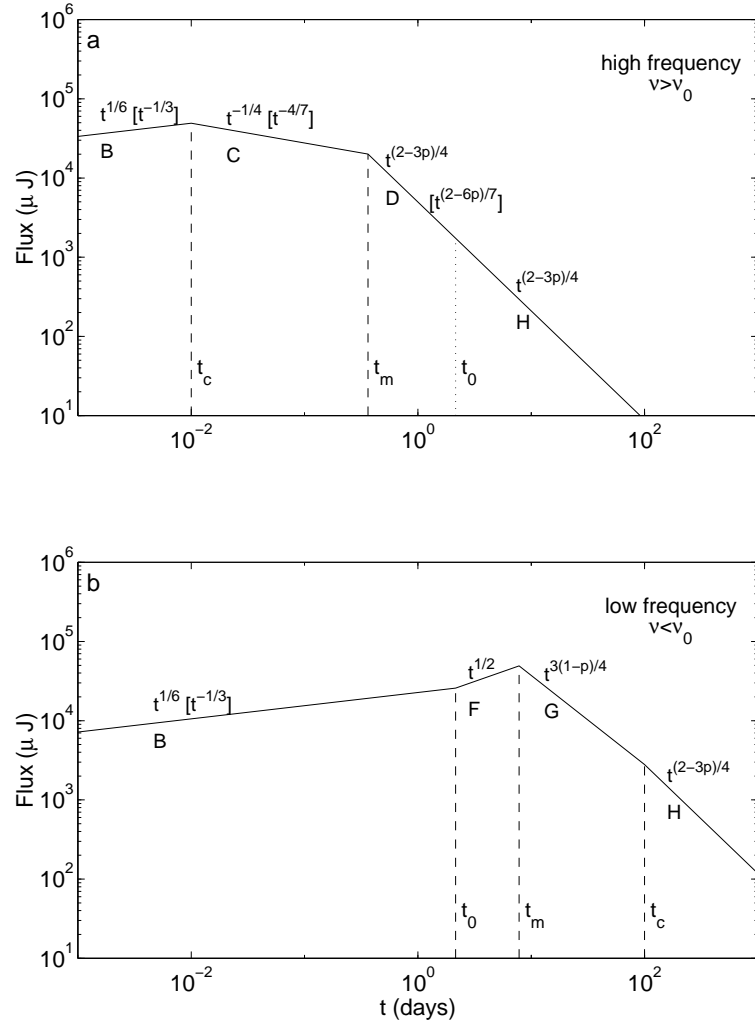


Fig. 27.—Light curve due to synchrotron radiation from a spherical relativistic shock, ignoring the effect of self-absorption. (a) The highfrequency case ( $\nu > \nu_0$ ). The light curve has four segments, separated by the critical times,  $t_c$ ,  $t_m$ ,  $t_0$ . The labels, B, C, D, H, indicate the correspondence with spectral segments in Fig. 22. The observed flux varies with time as indicated; the scalings within square brackets are for radiative evolution (which is restricted to  $t < t_0$ ) and the other scalings are for adiabatic evolution. (b) The low frequency case ( $\nu < \nu_0$ ). From [246].

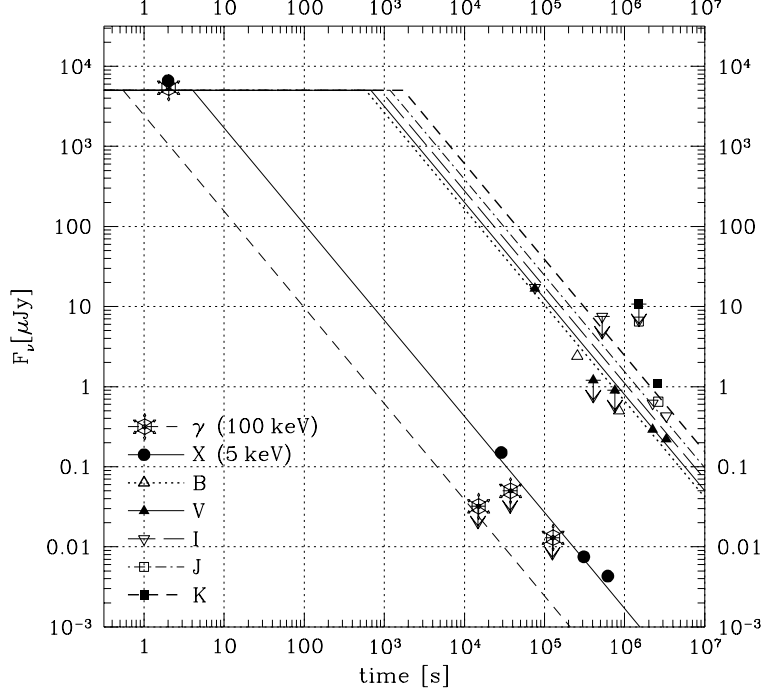


Fig. 28.— Decline in the afterglow of GRB970228 in different wavelength and theoretical model, from [22]

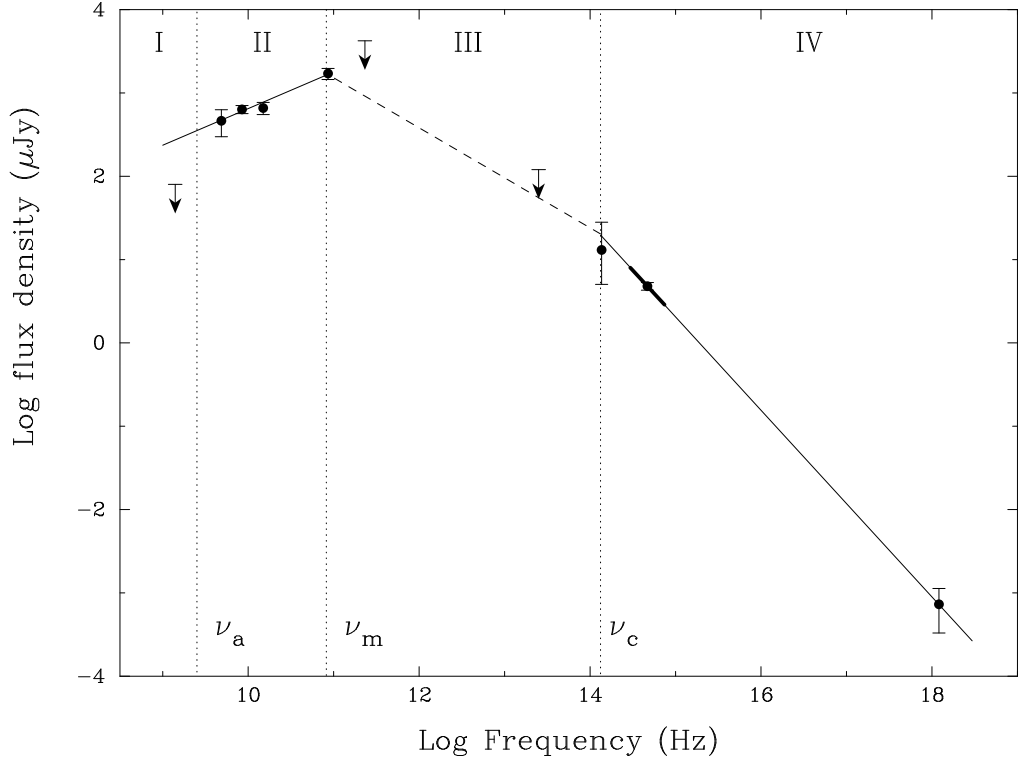


Fig. 29.— The X-ray to radio spectrum of GRB 970508 on May 21.0 UT (12.1 days after the event). The fit to the low-frequency part,  $\alpha_{4.86-86\text{GHz}} = 0.44 \pm 0.07$ , is shown as well as the extrapolation from X-ray to optical (solid lines). The local optical slope (2.1–5.0 days after the event) is indicated by the thick solid line. Also indicated is the extrapolation  $F_\nu \propto \nu^{-0.6}$  (lines). Indicated are the rough estimates of the break frequencies  $\nu_a$ ,  $\nu_m$  and  $\nu_c$  for May 21.0 UT from [260]